ADAPTIVE DISCRETE-ORDINATES QUADRATURES BASED ON DISCONTINUOUS FINITE ELEMENTS OVER SPHERICAL QUADRILATERALS

A Dissertation

by

CHEUK YIU LAU

Submitted to the Office of Graduate and Professional Studies of
Texas A&M University
in partial fulfillment of the requirements for the degree of

DOCTOR OF PHILOSOPHY

Chair of Committee,	Marvin Adams
Committee Members,	Teresa Bailey
	Joshua Jarrell
	Raytcho Lazarov
	Ryan McClarren
	Jim Morel
	Jean Ragusa
Head of Department,	Yassin Hassan

August 2016

Major Subject: Nuclear Engineering

ABSTRACT

We present a new family of discrete-ordinates (S_n) angular quadratures based on discontinuous finite elements (DFEM) in angle. The angular domain is divided into spherical quadrilaterals (SQs) on the unit sphere surface. Linear and quadratic discontinuous finite element (LDFE and QDFE) basis functions in the direction cosines are defined over each SQ, producing LDFE-SQ and QDFE-SQ angular quadratures, respectively. The new angular quadratures demonstrate more uniform direction and weight distributions than previous DFEM-based angular quadratures, local refinement capability, strictly positive weights, generation to large numbers of directions, and 4th-order accurate high-degree spherical harmonics (SH) integration. Results suggest that particle-conservation errors due to inexact high-degree SH integration rapidly diminish with quadrature refinement, and tend to be orders of magnitude smaller than other discretization errors affecting the solution. Results also demonstrate that the performance of the new angular quadratures without local refinement is on par with or better than that of traditional angular quadratures for various radiation transport problems. The performance of the new angular quadratures can be further improved by using local refinement, especially within an adaptive S_n algorithm.

The effectiveness of DFEM-based angular quadratures in adaptive S_n algorithms is limited by the accuracy of the mapping algorithms required for passing the angular flux solution between spatial regions with different angular quadrature refinement. An "optimal" mapping algorithm should preserve both the shape and the angular moments of interest from the incoming solution. We present a new mapping algorithm which is nearly "optimal" for mapping sufficiently smooth solutions away

from octant boundaries. If the mapped solution contains over- and under-shoots, we apply a fix-up algorithm that uses multi-objective optimization to ensure that the mapped solution remains within prescribed bounds, and exactly preserves the 0th angular moment of the incoming solution. We have demonstrated the use of the new mapping and fix-up algorithms for mapping increasing-degree SH functions, and nearly discontinuous angular flux solutions.

The new angular quadratures along with the new mapping and fix-up algorithms provide the necessary tools for using DFEM-based angular quadratures in adaptive S_n algorithms. Future work should include testing various adaptive S_n algorithms, and their efficient parallel implementation.

ACKNOWLEDGEMENTS

First and foremost, I would like to thank my graduate advisor, Dr. Marvin Adams, for his guidance in this research. I would also like to thank my committee members: Dr. Teresa Bailey, Dr. Joshua Jarrell, Dr. Raytcho Lazarov, Dr. Ryan McClarren, Dr. Jim Morel, and Dr. Jean Ragusa for participating in my defense, and offering positive feedback on this dissertation. Lastly, I would like to thank Daryl Hawkins and Michael Adams for helping me with issues related to the radiation transport code (PDT) required for this research.

I would like to acknowledge the National Exellence Fellowship sponsored by Texas A&M University for funding this research, and Lawrence Livermore National Laboratory for providing me the opportunity to perform multiple summer practicums in the area of computational physics.

TABLE OF CONTENTS

Page

LIST OF FIGURES

FIGURE Page

LIST OF TABLES

TABLE Page

1. INTRODUCTION

In this dissertation, we present a new family of discrete-ordinates (S_n) angular quadratures based on discontinuous finite elements (DFEM) in angle for solving the linear Boltzmann transport equation (LBE).[1] The new angular quadratures have many desirable properties. By design, they are well-suited for adaptive S_n algorithms: they are locally refinable, have strictly positive weights, and lend themselves to accurate mapping across multiple refinement levels. They also offer advantages over traditional angular quadratures for standard (non-adaptive) S_n calculations, producing in many problems more accurate solutions with fewer unknowns. The new angular quadratures can be generated with large numbers of directions; for example, we have generated sets with ≈800,000 directions over all octants. The new angular quadratures without local refinement can integrate smooth functions with 4th-order truncation error. While many of the preceeding advantages also apply to previous DFEM-based angular quadratures, [2, 3] the new angular quadratures offer advantages over their predecessors, which are mainly attributed to more uniform direction and weight distributions.

Previous studies [2, 3] have shown that the effectiveness of adaptive S_n algorithms is limited by the accuracy of mapping algorithms required to pass the angular flux solution between spatial regions with different angular quadrature refinement. An "optimal" mapping algorithm should preserve both the shape and the angular moments of interest from the incoming solution. We present a new mapping algorithm that is nearly "optimal" for mapping smooth solutions away from octant boundaries (small pointwise errors are introduced into the mapped solution even when the incoming solution lives in the underlying DFEM basis space, due to the preservation of

the higher angular moments). However, over- and under-shoots (including negativities) may occur when mapping near solution discontinuities or octant boundaries. To address these instances, we have devised a fix-up algorithm that uses multi-objective optimization to ensure the mapped solution remains within prescribed bounds, and exactly preserves the 0th angular moment of the incoming solution. However, the fix-up algorithm introduces minor error into the preservation of the higher angular moments.

In the subsections that follow, we describe the LBE and briefly describe the contents of the remainder of this dissertation.

1.1 Linear Boltzmann Transport Equation

The LBE is used to model neutral-particle transport in many physical systems, such as the neutron population in nuclear reactors.[1] The LBE is a particle conservation equation in a seven-dimensional phase space: three in position, two in direction, one in energy, and one in time. The LBE for neutron transport is provided in Eqn. 1.1, where the left-hand side contains the change rate density plus the loss terms (i.e., net leakage and total interactions), and the right-hand side contains the gain terms (i.e., in-scatter and external plus fission source):

$$\frac{1}{v\left(E\right)}\frac{\partial\Psi\left(\vec{r},\vec{\Omega},E,t\right)}{\partial t}+\vec{\Omega}\cdot\vec{\nabla}\Psi\left(\vec{r},\vec{\Omega},E,t\right)+\sigma_{t}\left(\vec{r},E,t\right)\Psi\left(\vec{r},\vec{\Omega},E,t\right) \quad = \\ \int_{4\pi}d\Omega'\int_{0}^{\infty}dE'\sigma_{s}\left(\vec{r},\vec{\Omega}'\cdot\vec{\Omega},E'\rightarrow E,t\right)\Psi\left(\vec{r},\vec{\Omega}',E',t\right)+q\left(\vec{r},\vec{\Omega},E,t\right)\ , \qquad (1.1)$$

where

$$\vec{r}=\text{spatial coordinate vector}\left(\text{cm}\right)\ ,$$

$$\vec{\Omega}=\text{particle unit directional vector}\ ,$$

$$E = \text{particle energy}\,(\text{MeV})\ ,$$

$$t = \text{time}\,(\text{s})\ ,$$

$$v\,(E) = \text{particle speed}\left(\frac{\text{cm}}{\text{s}}\right)\ ,$$

$$\Psi\left(\vec{r},\vec{\Omega},E,t\right) = \text{particle angular flux}\left(\frac{\text{particles}}{\text{MeV}\cdot\text{ster}\cdot\text{cm}^2\cdot\text{s}}\right)\ ,$$

$$\sigma_t\left(\vec{r},E,t\right) = \text{total cross-section}\left(\frac{1}{\text{cm}}\right)\ ,$$

$$\sigma_s\left(\vec{r},\vec{\Omega}'\cdot\vec{\Omega},E'\rightarrow E,t\right) = \text{scattering cross-section}\left(\frac{1}{\text{cm}\cdot\text{MeV}\cdot\text{ster}}\right)\ ,$$

and

$$q\left(\vec{r},\vec{\Omega},E,t\right) = \text{particle source rate density}\left(\frac{\text{particles}}{\text{MeV}\cdot\text{ster}\cdot\text{cm}^3\cdot\text{s}}\right)\ .$$

Eqn. 1.1 is an integro-differential equation with a single unknown function Ψ, also known as the angular flux. Unique solutions for Ψ exist given appropriate boundary and initial conditions. We define the boundary condition as

$$\Psi\left(\vec{r}_s,\vec{\Omega},E,t\right) = F\left(\vec{r}_s,\vec{\Omega},E,t\right),\vec{n}\left(\vec{r}_s\right)\cdot\vec{\Omega} < 0\ , \tag{1.2}$$

where F is a known function, and $\vec{n}\left(\vec{r}_s\right)$ is the outward normal at point $\vec{r}_s$ on the surface of the problem domain. Eqn. 1.2 assumes the surface of the problem domain is non-reentrant. We define the initial condition as

$$\Psi\left(\vec{r},\vec{\Omega},E,t_0\right) = F_0\left(\vec{r},\vec{\Omega},E\right)\ , \tag{1.3}$$

where F_0 is a known function representing Ψ at the start of the problem.

The LBE shown in Eqn. 1.1 was derived under several assumptions.[1] First, we assume particles do not interact with each other, but only with the background material. This assumption is valid since the number of particles in the system is typically many orders of magnitude less than the number of particles (nuclei and electrons) in the background material. Second, we assume particles are not affected by outside forces (e.g., gravitational, magnetic or electric fields). This assumption allows particles to travel in straight paths. Third, we assume the quantum-mechanical wavelengths of particles are negligible compared to the distances between collisions. This assumption allows the velocity and position of a particle to be treated as deterministic, single-valued quantities. Fourth, we assume nuclei in the background material move isotropically. This assumption allows particles to see the same background material distribution from any incident direction, causing the total cross section to be independent of particle direction. Therefore, scattering cross sections only depend on the change in particle direction rather than the incident and exiting directions. Fifth, we assume all particle interactions occur instantaneously.

1.2 Dissertation Layout

Analytic solutions to the LBE are available only for simple problems. In practice, each independent variable is discretized in order to form a large set of algebraic equations that can be iteratively solved. In this research, we focus on angular discretization using advanced angular quadratures in the discrete-ordinates (S_n) method. Section 2 discusses the S_n method and highlights desirable angular quadrature properties. A brief discussion of time, energy, and spatial discretization is also provided for completeness. Section 3 discusses traditional angular quadratures used in the S_n method, and highlights several of their shortcomings that the DFEM-based angular quadratures overcome. We then discuss previous DFEM-based angular quadratures,

[2, 3] which led to the current research. Lastly, we discuss recently developed angular quadratures, and highlight their differences compared to the DFEM-based angular quadratures. Section 4 presents the construction of the new DFEM-based angular quadratures, and discusses their advantages over the previous DFEM-based angular quadratures. Section 5 presents the new mapping and fix-up algorithms required for passing the angular flux solution between spatial regions with different angular quadrature refinement. Section 6 presents the computational results using the new DFEM-based angular quadratures, and the new mapping and fix-up algorithms. Section 7 summarizes the results, draws conclusions, and offers suggestions for future work.

2. DISCRETIZATION OF THE LINEAR BOLTZMANN TRANSPORT EQUATION

This reseach focuses on the angular discretization of the linear Boltzmann transport equation (LBE) using advanced angular quadratures in the discrete-ordinates (S_n) method. In this section, we discuss the S_n method, and highlight desirable angular quadrature properties. We also briefly discuss time, energy, and spatial discretization for completeness.

2.1 Time Discretization

Time discretization partitions the temporal domain into a series of non-overlapping time steps $\Delta t_n = t_{n+1} - t_n, n = 1 : N$. A general approach is to integrate the LBE (Eqn. 1.1) over each time step and divide by Δt_n:

$$\frac{\Psi_{n+1}\left(\vec{r},\vec{\Omega},E\right)-\Psi_n\left(\vec{r},\vec{\Omega},E\right)}{v\left(E\right)\Delta t_n}+\vec{\Omega}\cdot\vec{\nabla}\overline{\Psi}\left(\vec{r},\vec{\Omega},E\right)+\overline{\sigma}_t\left(\vec{r},E\right)\overline{\Psi}\left(\vec{r},\vec{\Omega},E\right) = \int_{4\pi}d\Omega'\int_0^\infty dE'\overline{\sigma}_s\left(\vec{r},\vec{\Omega}'\cdot\vec{\Omega},E'\rightarrow E\right)\overline{\Psi}\left(\vec{r},\vec{\Omega}',E'\right)+\overline{q}\left(\vec{r},\vec{\Omega},E\right), \quad (2.1)$$

where

$$\overline{\Psi}\left(\vec{r},\vec{\Omega},E\right)=\frac{1}{\Delta t_n}\int_{t_n}^{t_{n+1}}dt\Psi\left(\vec{r},\vec{\Omega},E,t\right), \quad (2.2)$$

$$\overline{q}\left(\vec{r},\vec{\Omega},E\right)=\frac{1}{\Delta t_n}\int_{t_n}^{t_{n+1}}dtq\left(\vec{r},\vec{\Omega},E,t\right), \quad (2.3)$$

$$\overline{\sigma}_t\left(\vec{r},E\right)=\frac{\int_{t_n}^{t_{n+1}}dt\Psi\left(\vec{r},\vec{\Omega},E,t\right)\sigma_t\left(\vec{r},E,t\right)}{\int_{t_n}^{t_{n+1}}dt\Psi\left(\vec{r},\vec{\Omega},E,t\right)}, \quad (2.4)$$

and

$$\overline{\sigma}_s\left(\vec{r},\vec{\Omega}'\cdot\vec{\Omega},E'\rightarrow E\right)=\frac{\int_{t_n}^{t_{n+1}}dt\Psi\left(\vec{r},\vec{\Omega},E,t\right)\sigma_s\left(\vec{r},\vec{\Omega}'\cdot\vec{\Omega},E'\rightarrow E,t\right)}{\int_{t_n}^{t_{n+1}}dt\Psi\left(\vec{r},\vec{\Omega},E,t\right)}. \tag{2.5}$$

Since Ψ_n is known from the previous time step, Eqn. 2.1 has two unknowns (Ψ_{n+1} and $\overline{\Psi}$) requiring a closure relationship, an example of which is:

$$\overline{\Psi}\left(\vec{r},\vec{\Omega},E\right)=\beta\Psi_{n+1}\left(\vec{r},\vec{\Omega},E\right)+\left(1-\beta\right)\Psi_n\left(\vec{r},\vec{\Omega},E\right)\ . \tag{2.6}$$

Different choices for β lead to different time discretization methods (e.g., $\beta=1/2$ for Crank-Nicholson or $\beta=1$ for backward Euler). We can eliminate Ψ_{n+1} from Eqn. 2.1 by applying Eqn. 2.6 to obtain

$$\begin{aligned}\vec{\Omega}\cdot\vec{\nabla}\overline{\Psi}\left(\vec{r},\vec{\Omega},E\right)+\overline{\sigma}_{t,\text{eff}}\left(\vec{r},E\right)\overline{\Psi}\left(\vec{r},\vec{\Omega},E\right)\ &=\\ \int_{4\pi}d\Omega'\int_0^\infty dE'\overline{\sigma}_s\left(\vec{r},\vec{\Omega}'\cdot\vec{\Omega},E'\rightarrow E\right)\overline{\Psi}\left(\vec{r},\vec{\Omega}',E'\right)+\overline{q}_{\text{eff}}\left(\vec{r},\vec{\Omega},E\right)\ ,\end{aligned} \tag{2.7}$$

where

$$\overline{\sigma}_{t,\text{eff}}\left(\vec{r},E\right)=\overline{\sigma}_t\left(\vec{r},E\right)+\frac{1}{v\left(E\right)\Delta t\beta}\ , \tag{2.8}$$

and

$$\overline{q}_{\text{eff}}\left(\vec{r},\vec{\Omega},E\right)=\overline{q}\left(\vec{r},\vec{\Omega},E\right)+\frac{\Psi_n\left(\vec{r},\vec{\Omega},E\right)}{v\left(E\right)\Delta t\beta}\ . \tag{2.9}$$

These equations, which are particular to the form of closure chosen above, illustrate a general truth: time discretization with any degree of implicitness results in a series of steady-state problems. Therefore, if we can solve steady-state problems, we can solve discretized time-dependent problems.

2.2 Energy Discretization

Energy discretization partitions the energy domain into a series of non-overlapping energy intervals $\Delta E_g = E_{g-1} - E_g, g = 1 : G$. A general approach is to integrate the time-differenced LBE (Eqn. 2.7 with over-bars and *eff* subscript removed) over each energy interval ΔE_g:

$$\vec{\Omega} \cdot \vec{\nabla} \Psi_g \left(\vec{r}, \vec{\Omega} \right) + \sigma_{t,g} \left(\vec{r} \right) \Psi_g \left(\vec{r}, \vec{\Omega} \right) \quad =$$

$$\int_{4\pi} d\Omega' \sum_{g'=1}^{G} \sigma_{s,g' \to g} \left(\vec{r}, \vec{\Omega}' \cdot \vec{\Omega} \right) \Psi_{g'} \left(\vec{r}, \vec{\Omega}' \right) + q_g \left(\vec{r}, \vec{\Omega} \right) \quad , \quad g = 1 : G \, , \tag{2.10}$$

where:

$$\Psi_g \left(\vec{r}, \vec{\Omega} \right) = \int_{E_g}^{E_{g-1}} dE \Psi \left(\vec{r}, \vec{\Omega}, E \right) \, , \tag{2.11}$$

$$q_g \left(\vec{r}, \vec{\Omega} \right) = \int_{E_g}^{E_{g-1}} dE q \left(\vec{r}, \vec{\Omega}, E \right) \, , \tag{2.12}$$

$$\sigma_{t,g} \left(\vec{r} \right) = \frac{\int_{E_g}^{E_{g-1}} dE \sigma_t \left(\vec{r}, E \right) F \left(E \right)}{\int_{E_g}^{E_{g-1}} dE F \left(E \right)} \, , \tag{2.13}$$

$$\sigma_{s,g' \to g} \left(\vec{r}, \vec{\Omega}' \cdot \vec{\Omega} \right) = \frac{\int_{E_{g'}}^{E_{g'-1}} dE' \int_{E_g}^{E_{g-1}} dE \sigma_s \left(\vec{r}, \vec{\Omega}' \cdot \vec{\Omega}, E' \to E \right) F \left(E' \right)}{\int_{E_{g'}}^{E_{g'-1}} dE' F \left(E' \right)} \, , \tag{2.14}$$

and $F\left(E\right)$ is an energy shape function, which is usually determined by solving a simplified model problem. We can separate the within-group scattering to obtain a one-group equation:

$$\vec{\Omega} \cdot \vec{\nabla} \Psi_g \left(\vec{r}, \vec{\Omega} \right) + \sigma_{t,g} \left(\vec{r} \right) \Psi_g \left(\vec{r}, \vec{\Omega} \right) \quad =$$

$$\int_{4\pi} d\Omega' \sigma_{s,g \to g} \left(\vec{r}, \vec{\Omega}' \cdot \vec{\Omega} \right) \Psi_g \left(\vec{r}, \vec{\Omega}' \right) + q_{g,\text{eff}} \left(\vec{r}, \vec{\Omega} \right) \quad , \quad g = 1 : G \, , \tag{2.15}$$

where

$$q_{g,\text{eff}}\left(\vec{r},\vec{\Omega}\right)=q_g\left(\vec{r},\vec{\Omega}\right)+\int_{4\pi}d\Omega'\sum_{g'=1,g'\neq g}^{G}\sigma_{s,g'\rightarrow g}\left(\vec{r},\vec{\Omega}'\cdot\vec{\Omega}\right)\Psi_{g'}\left(\vec{r},\vec{\Omega}'\right)\ . \tag{2.16}$$

Therefore, energy discretization results in a series of one-group equations coupled by the group-to-group scattering term.

2.3 Angular Discretization

Consider the time and energy-differenced LBE (Eqn. 2.15 with subscripts g and *eff* removed):

$$\vec{\Omega}\cdot\vec{\nabla}\Psi\left(\vec{r},\vec{\Omega}\right)+\sigma_t\left(\vec{r}\right)\Psi\left(\vec{r},\vec{\Omega}\right)=q_s\left(\vec{r},\vec{\Omega}\right)+q\left(\vec{r},\vec{\Omega}\right)\ , \tag{2.17}$$

where q_s is the scattering source:

$$q_s\left(\vec{r},\vec{\Omega}\right)=\int_{4\pi}d\Omega'\sigma_s\left(\vec{r},\vec{\Omega}'\cdot\vec{\Omega}\right)\Psi\left(\vec{r},\vec{\Omega}'\right)\ . \tag{2.18}$$

We begin by expanding the angular flux in q_s in terms of spherical harmonics (SH) functions:

$$\Psi\left(\vec{r},\vec{\Omega}'\right)=\sum_{l=0}^{\infty}\frac{2l+1}{4\pi}\sum_{\tilde{m}=-l}^{l}\phi_{l\tilde{m}}\left(\vec{r}\right)Y_{l\tilde{m}}\left(\vec{\Omega}'\right)\ , \tag{2.19}$$

where $Y_{l\tilde{m}}$ is the SH function of degree l and order $\tilde{m}$, and $\phi_{l\tilde{m}}$ is the angular flux moment of degree l and order $\tilde{m}$ defined as:

$$\phi_{l\tilde{m}}\left(\vec{r}\right)=\int_{4\pi}d\Omega\Psi\left(\vec{r},\vec{\Omega}\right)Y^*_{l\tilde{m}}\left(\vec{\Omega}\right)\ . \tag{2.20}$$

Next, we expand the scattering cross section in terms of Legendre polynomials:

$$\sigma_s\left(\vec{r},\vec{\Omega}'\cdot\vec{\Omega}\right)=\sum_{l'=0}^{L}\frac{2l'+1}{4\pi}\sigma_{sl'}\left(\vec{r}\right)P_{l'}\left(\mu_0\right)\ , \tag{2.21}$$

where L is the anisotropic scattering order, $\mu_0=\vec{\Omega}'\cdot\vec{\Omega}$ is the scattering angle cosine, $P_{l'}$ is the Legendre polynomial of degree l', and $\sigma_{sl'}$ is the scattering cross section Legendre expansion coefficient of degree l' defined as:

$$\sigma_{sl'}\left(\vec{r}\right)=\int_{-1}^{1}d\mu_0\sigma_s\left(\mu_0\right)P_{l'}\left(\mu_0\right)\ . \tag{2.22}$$

We insert Eqns. 2.19 and 2.21 into 2.18 to obtain

$$q_s\left(\vec{r},\vec{\Omega}\right)=\int_{4\pi}d\Omega'\sum_{l'=0}^{L}\frac{2l'+1}{4\pi}\sigma_{sl'}\left(\vec{r}\right)P_{l'}\left(\mu_0\right)\sum_{l=0}^{\infty}\frac{2l+1}{4\pi}\sum_{\tilde{m}=-l}^{l}\phi_{l\tilde{m}}\left(\vec{r}\right)Y_{l\tilde{m}}\left(\vec{\Omega}'\right)\ . \tag{2.23}$$

The SH addition theorem states

$$P_{l'}\left(\mu_0\right)=\frac{1}{2l'+1}\sum_{\tilde{m}'=-l'}^{l'}Y^*_{l'\tilde{m}'}\left(\vec{\Omega}'\right)Y_{l'\tilde{m}'}\left(\vec{\Omega}\right)\ . \tag{2.24}$$

The SH orthogonality property states

$$\int_{4\pi}d\Omega' Y^*_{l'\tilde{m}'}\left(\vec{\Omega}'\right)Y_{l\tilde{m}}\left(\vec{\Omega}'\right)=4\pi\delta_{ll'}\delta_{\tilde{m}\tilde{m}'}\ . \tag{2.25}$$

We apply Eqns. 2.24 and 2.25 to 2.23 to obtain the expanded scattering source:

$$q_s\left(\vec{r},\vec{\Omega}\right)=\sum_{l=0}^{L}\frac{2l+1}{4\pi}\sigma_{sl}\left(\vec{r}\right)\sum_{\tilde{m}=-l}^{l}\phi_{l\tilde{m}}\left(\vec{r}\right)Y_{l\tilde{m}}\left(\vec{\Omega}\right)\ . \tag{2.26}$$

We insert Eqn. 2.26 back into 2.17 to obtain

$$\vec{\Omega}\cdot\vec{\nabla}\Psi\left(\vec{r},\vec{\Omega}\right)+\sigma_t\left(\vec{r}\right)\Psi\left(\vec{r},\vec{\Omega}\right) \;=\; \sum_{l=0}^{L}\frac{2l+1}{4\pi}\sigma_{sl}\left(\vec{r}\right)\sum_{\tilde{m}=-l}^{l}\phi_{l\tilde{m}}\left(\vec{r}\right)Y_{l\tilde{m}}\left(\vec{\Omega}\right)+q\left(\vec{r},\vec{\Omega}\right)\;. \tag{2.27}$$

2.3.1 Discrete-Ordinates Method

The S_n method solves Eqn. 2.27 at a set of discrete directions $\vec{\Omega}_m$ with associated weights $w_m, m = 1 : M$, and approximates angular integrals using finite sums:

$$\vec{\Omega}_m\cdot\vec{\nabla}\Psi_m\left(\vec{r}\right)+\sigma_t\left(\vec{r}\right)\Psi_m\left(\vec{r}\right) \;=\; \sum_{l=0}^{L}\frac{2l+1}{4\pi}\sigma_{sl}\left(\vec{r}\right)\sum_{\tilde{m}=-l}^{l}\phi_{l\tilde{m}}\left(\vec{r}\right)Y_{l\tilde{m}}\left(\vec{\Omega}_m\right)+q_m\left(\vec{r}\right)\quad,\quad m=1:M\;, \tag{2.28}$$

where

$$\Psi_m=\Psi\left(\vec{\Omega}_m\right)\;, \tag{2.29}$$

$$q_m=q\left(\vec{\Omega}_m\right)\;, \tag{2.30}$$

and

$$\phi_{l\tilde{m}}\left(\vec{r}\right)\approx\sum_{m=1}^{M}w_m\Psi_m\left(\vec{r}\right)Y^*_{l\tilde{m}}\left(\vec{\Omega}_m\right)\;. \tag{2.31}$$

The set of discrete directions and weights forms an angular quadrature. Therefore, angular discretization using the S_n method results in a series of equations solved at discrete directions with angular flux moments formed using Eqn. 2.31.

2.3.2 Desirable Angular Quadrature Properties

The S_n form of the LBE above, combined with information about our solution quantities of interest and solution characteristics in problems of interest, imply sev-

eral important properties that angular quadratures should have for maximum utility in radiation transport problems. In the following subsections, we discuss these properties in more detail, and thereby enumerate the properties that we seek for the new angular quadratures presented in this research.

2.3.2.1 Accurate Global Spherical Harmonics Integration

Angular quadratures must integrate Eqn. 2.28 over the global angular domain to obtain a statement of particle balance:

$$\sum_{m=0}^{M} w_m \vec{\Omega}_m \cdot \vec{\nabla} \Psi_m \left(\vec{r}\right) + \sum_{m=0}^{M} w_m \sigma_t \left(\vec{r}\right) \Psi_m \left(\vec{r}\right) = \sum_{m=0}^{M} w_m \sum_{l=0}^{L} \frac{2l+1}{4\pi} \sigma_{sl} \left(\vec{r}\right) \sum_{\tilde{m}=-l}^{l} \phi_{l\tilde{m}} \left(\vec{r}\right) Y_{l\tilde{m}} \left(\vec{\Omega}_m\right) + \sum_{m=0}^{M} w_m q_m \left(\vec{r}\right). \tag{2.32}$$

The integral of the streaming term over all angles (i.e., the first term on the left-hand side of Eqn. 2.32) can be written in terms of the net current density, $\vec{J}(\vec{r})$:

$$\sum_{m=0}^{M} w_m \vec{\Omega}_m \cdot \vec{\nabla} \Psi_m \left(\vec{r}\right) = \vec{\nabla} \cdot \vec{J} \left(\vec{r}\right) \tag{2.33}$$

where $\vec{J}(\vec{r}) = \sum_{m=0}^{M} w_m (\vec{\Omega}_m \Psi_m \left(\vec{r}\right))$. The scalar flux is defined as

$$\phi_{00} \left(\vec{r}\right) = \sum_{m=0}^{M} w_m \Psi_m \left(\vec{r}\right). \tag{2.34}$$

Inserting Eqns. 2.33 and 2.34 into 2.32 produces

$$\vec{\nabla} \cdot \vec{J} \left(\vec{r}\right) + \sigma_t \left(\vec{r}\right) \phi_{00} \left(\vec{r}\right) = \sum_{m=0}^{M} w_m \sum_{l=0}^{L} \frac{2l+1}{4\pi} \sigma_{sl} \left(\vec{r}\right) \sum_{\tilde{m}=-l}^{l} \phi_{l\tilde{m}} \left(\vec{r}\right) Y_{l\tilde{m}} \left(\vec{\Omega}_m\right) + \sum_{m=0}^{M} w_m q_m \left(\vec{r}\right). \tag{2.35}$$

Analytically, the integral of SH functions above 0th degree over all angles should be zero (due to the SH orthogonality property); however, angular quadratures are not guaranteed to exactly integrate these functions to zero. Therefore, the first term on the right-side of Eqn. 2.35 becomes

$$\sum_{m=0}^{M} w_m \sum_{l=0}^{L} \frac{2l+1}{4\pi} \sigma_{sl}\left(\vec{r}\right) \sum_{\tilde{m}=-l}^{l} \phi_{l\tilde{m}}\left(\vec{r}\right) Y_{l\tilde{m}}\left(\vec{\Omega}_m\right) = \frac{1}{4\pi} \sigma_{s0}\left(\vec{r}\right) \phi_{00}\left(\vec{r}\right) + \epsilon, \tag{2.36}$$

where ϵ is the contamination term consisting of the angular quadrature integration errors for the SH functions above 0th degree. Inserting Eqn. 2.36 into 2.35, and recognizing $\sigma_a = \sigma_t - \sigma_{s0}$ results in

$$-\vec{\nabla} \cdot \vec{J}\left(\vec{r}\right) - \sigma_a\left(\vec{r}\right) \phi_{00}\left(\vec{r}\right) + \sum_{m=0}^{M} w_m q_m\left(\vec{r}\right) + \epsilon = 0. \tag{2.37}$$

Eqn. 2.37 is a statement of exact particle balance (i.e., net outleakage rate density + absorption rate density = volumetric source-rate density) if the contamination term ϵ is zero, which can only occur if the angular quadrature can exactly integrate SH functions of up to degree L over the global angular domain.

In certain practical problems of interest, the angular flux solution is smooth, and thus can be well-approximated by a SH expansion of degree K over the global angular domain. In this case, Eqn. 2.31 suggests that the angular quadratures must accurately integrate SH functions of up to degree $L + K$ over the global angular domain to accurately form the angular flux moments.

2.3.2.2 Accurate Local Angular Flux Integration

The largest component of the scattering source is the isotropic term (i.e., the ϕ_{00} term). Therefore, it is important for angular quadratures to accurately integrate the angular flux itself. In many practical problems of interest, this requires accurate

integration of functions that are not smooth, but rather are peaky, nearly discontinuous, and have significant magnitudes only in small local angular regions. This is illustrated in Fig. 2.1, which plots a high-energy angular flux solution as a function of azimuthal angle for a fixed location in an infinite lattice of circular fuel pins in water. Fig. 2.1 shows the angular flux solution is peaky, and nearly discontinuous even for a relatively simple radiation transport problem. In many practical problems of interest, the particular local angular regions containing the majority of the angular flux may not be the same for different spatial regions. Therefore, in order to accurately form the angular flux moments for practical radiation transport problems, angular quadratures must accurately integrate piecewise discontinuous functions whose discontinuities can occur anywhere in the angular domain. In addition, uniform quadrature directions and weights are desired because non-uniformity leads to differences in the integration of two functions that are simply rotations or translations of each other.

Inaccurate local integration of the angular flux solution may lead to ray effects. Consider the radiation transport problem illustrated in Fig. 2.2 containing a circular isotropic source surrounded by vacuum.[4] The quantities of interest are the 0th angular flux moments (i.e., scalar fluxes) at spatial points A and B. Fig. 2.3 plots the angular flux solution as a function of azimuthal angle at spatial points A and B, along with the directions for an evenly-distributed eight-point angular quadrature. The angular quadrature will produce a scalar flux of zero at spatial point A, since none of the quadrature directions happen to pass through a non-zero portion of its angular flux solution. However, the angular quadrature will produce a scalar flux of erroneously high value at spatial point B, since one of the quadrature directions happens to pass through its angular flux solution maximum. Fig. 2.4 plots the resulting scalar flux spatial distribution containing artificial peaks and valleys known

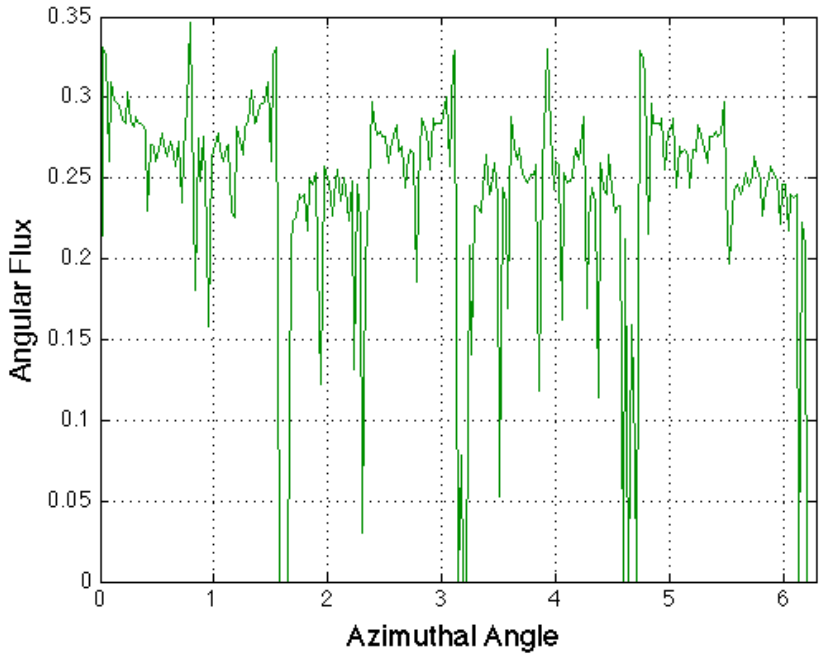

Figure 2.1: Angular flux solution at a fixed location in an infinite lattice of circular fuel pins in water.

as ray effects. In order to mitigate ray effects, angular quadratures must accurately integrate the angular flux solution over small local angular regions.

We also note certain quantities of interest may involve integrating the angular flux solution multiplied by different degree SH functions over specific local angular regions. For example, the rate at which particles leave a surface requires the angular quadratures to accurately integrate $\Psi \times \vec{n} \cdot \vec{\Omega}$ over local angular regions.

2.4 Spatial Discretization

Spatial discretization partitions the spatial domain into a set of non-overlapping spatial cells, $V_k, k = 1 : K$. The following procedure applies DFEM spatial discretization [5] to the time, energy, and angular differenced LBE provided in Eqn. 2.28. We begin by selecting the basis functions $b_{kj}(\vec{r}), j = 1 : J_k$ for each spatial cell k. The DFEM method approximates the angular flux solution as a linear combination of the

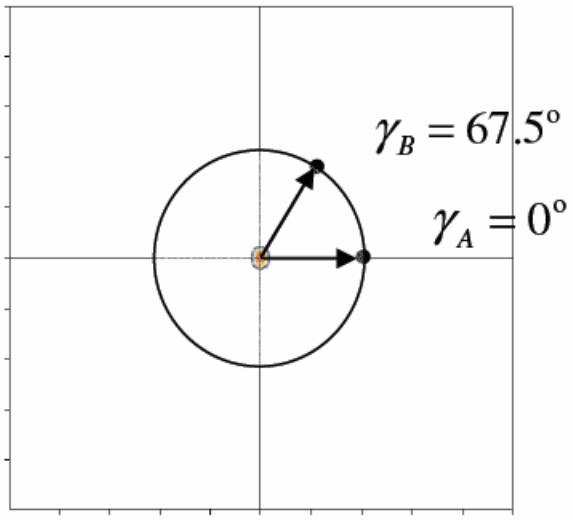

Figure 2.2: Circular isotropic source surrounded by vacuum. Quantities of interest are the scalar fluxes at spatial points A and B.

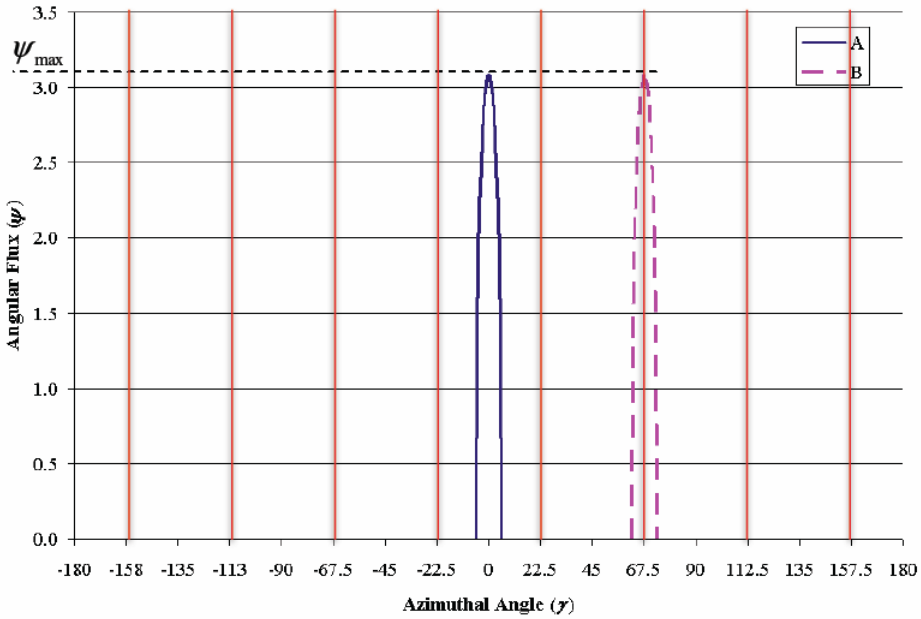

Figure 2.3: Angular flux solution at spatial points A and B. Red lines indicate the eight evenly-distributed angular quadrature directions.

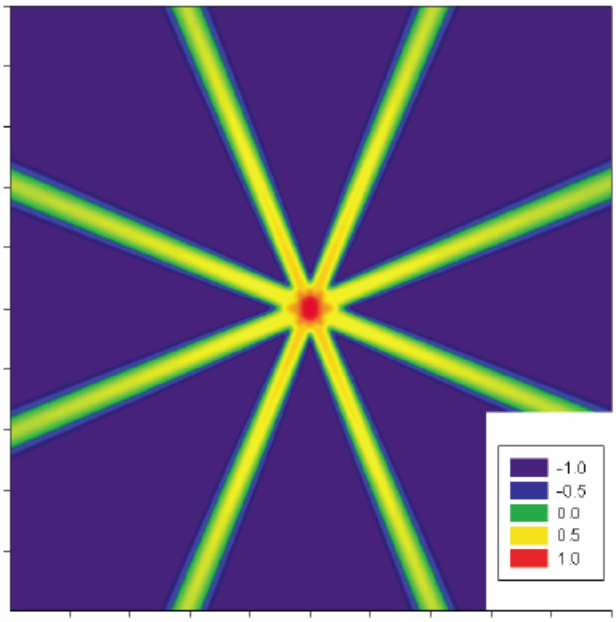

Figure 2.4: Scalar flux spatial distribution showing prominent ray effects.

selected basis functions:

$$\Psi_m\left(\vec{r}\right) \approx \psi_m\left(\vec{r}\right) \equiv \sum_{j=1}^{J_k} \psi_{kj} b_{kj}\left(\vec{r}\right) \quad , \quad \vec{r} \in V_k \tag{2.38}$$

We use the Galerkin method, which requires that weighted integrals of the transport equation be satisfied, with the chosen basis functions serving also as the weight functions. That is, the i-th weighted-integral equation is obtained by multiplying Eqn. 2.28 by $b_{ki}(\vec{r})$ and integrating over the volume of the problem. This reduces to an integral over the k-th cell, because $b_{ki}(\vec{r}) = 0$ outside of the k-th cell. We obtain:

$$\int_{V_k} d^3 r b_{ki}\left(\vec{r}\right) \left[\vec{\Omega}_m \cdot \vec{\nabla} \Psi_m\left(\vec{r}\right) + \sigma_t\left(\vec{r}\right) \Psi_m\left(\vec{r}\right)\right] =$$

$$\int_{V_k} d^3 r b_{ki}\left(\vec{r}\right) \left[\sum_{l=0}^{L} \frac{2l+1}{4\pi} \sigma_{sl}\left(\vec{r}\right) \sum_{\tilde{m}=-l}^{l} \phi_{l\tilde{m}}\left(\vec{r}\right) Y_{l\tilde{m}}\left(\vec{\Omega}_m\right) + q_m\left(\vec{r}\right)\right] \quad ,$$

$$m = 1 : M \ , \ i = 1 : J_k \ , \ k = 1 : K. \quad (2.39)$$

Next, we apply Green's theorem to the leakage term (i.e., first term on the left-hand side of Eqn. 2.39) to obtain

$$\int_{\partial V_k} d^2 r b_{ki}\left(\vec{r}_{kl}\right) \vec{n} \cdot \vec{\Omega} \Psi_m\left(\vec{r}_{kl}\right) + \int_{V_k} d^3 r \left[-\Psi_m\left(\vec{r}\right) \vec{\Omega} \cdot \vec{\nabla} b_{ki}\left(\vec{r}\right) + b_{ki}\left(\vec{r}\right) \sigma_t\left(\vec{r}\right) \Psi_m\left(\vec{r}\right) \right] =$$
$$\int_{V_k} d^3 r b_{ki}\left(\vec{r}\right) \left[\sum_{l=0}^{L} \frac{2l+1}{4\pi} \sigma_{sl}\left(\vec{r}\right) \sum_{\tilde{m}=-l}^{l} \phi_{l\tilde{m}}\left(\vec{r}\right) Y_{l\tilde{m}}\left(\vec{\Omega}_m\right) + q_m\left(\vec{r}\right) \right] \ ,$$
$$m = 1 : M \ , \ i = 1 : J_k \ , \ k = 1 : K, \quad (2.40)$$

where ∂V_k is the surface of cell k, and $\vec{r}_{kl}$ is a point on surface l of cell k. We insert the DFEM angular flux approximation (Eqn. 2.38) into Eqn. 2.40 to obtain

$$\int_{\partial V_k} d^2 r b_{ki}\left(\vec{r}_{kl}\right) \vec{n} \cdot \vec{\Omega} \Psi_m\left(\vec{r}_{kl}\right) +$$
$$\sum_{j=1}^{J_k} \psi_{kj} \int_{V_k} d^3 r \left[-b_{kj}\left(\vec{r}\right) \vec{\Omega} \cdot \vec{\nabla} b_{ki}\left(\vec{r}\right) + b_{ki}\left(\vec{r}\right) \sigma_t\left(\vec{r}\right) b_{kj}\left(\vec{r}\right) \right] =$$
$$\int_{V_k} d^3 r b_{ki}\left(\vec{r}\right) \left[\sum_{l=0}^{L} \frac{2l+1}{4\pi} \sigma_{sl}\left(\vec{r}\right) \sum_{\tilde{m}=-l}^{l} \phi_{l\tilde{m}}\left(\vec{r}\right) Y_{l\tilde{m}}\left(\vec{\Omega}_m\right) + q_m\left(\vec{r}\right) \right] \ ,$$
$$m = 1 : M \ , \ i = 1 : J_k \ , \ k = 1 : K. \quad (2.41)$$

Lastly, the surface terms are set to the upstream ψ values on each surface:

$$\Psi_m\left(\vec{r}_{kl}\right) = \left\{ \begin{array}{ll} \psi_m\left(\vec{r}_{kl}^{-}\right) & , \ \vec{n}_{kl} \cdot \vec{\Omega} > 0 \\ \psi_m\left(\vec{r}_{kl}^{+}\right) & , \ \vec{n}_{kl} \cdot \vec{\Omega} < 0 \end{array} \right\}, \quad (2.42)$$

where $\vec{r}_{kl}^{+}$ is immediately outside surface l of cell k, and $\vec{r}_{kl}^{-}$ is just inside. Therefore, spatial discretization results in a series of equations solved over each spatial cell.

2.5 Iterative Solution

A general approach for solving the fully-discretized LBE is to perform an outer iteration that involves the solution of each energy group's equation, with some group-to-group scattering terms evaluated using the previous iterate. Within each energy group, we perform an inner iteration, which solves the fully-discretized LBE using the latest inner iteration's scalar flux for the within-group scattering source, and the latest outer iteration's scalar flux for the external-group scattering source. The inner iteration is converged when the difference in scalar flux between inner iterations is within tolerance for each spatial cell. The outer iteration is converged when the difference in scalar flux between outer iterations is within tolerance for each spatial cell in each energy group. There are many variations on this basic inner/outer iterative procedure. See [6] for a more complete discussion.

2.6 Summary

In this section, we discussed the time, energy, angular, and spatial discretization of the LBE (Eqn. 1.1). Each discretization method is an approximation of the continuous function, which introduces some level of discretization error. As discussed in Section 2.3.2, the S_n method for angular discretization introduces particle-conservation error if the angular quadratures do not exactly integrate SH functions of up to the scattering order over the global angular domain. Ray effects (i.e., artificial peaks and valleys in the scalar flux spatial distribution) may occur if the angular quadratures do not accurately integrate the angular flux solution over local angular regions, which produces incorrect angular flux moments. The next section describes traditional angular quadratures used in the S_n method, and discusses some of their deficiencies, which the DFEM-based angular quadratures overcome. We then present previous DFEM-based angular quadratures, which led to the current

research. Lastly, we discuss recently developed angular quadratures, and highlight their differences compared to DFEM-based angular quadratures.

3. DISCRETE-ORDINATES ANGULAR QUADRATURES

In this section, we describe angular quadratures [1, 7, 8, 9] that have been widely used for many years in the discrete-ordinates (S_n) method, and discuss several of their shortcomings which led to the development of discontinuous finite element (DFEM) based angular quadratures. We then describe previous DFEM-based angular quadratures, [2, 3] which led to the current research. Lastly, we discuss several recently developed angular quadratures, [10, 11, 12, 13] and highlight their differences compared to DFEM-based angular quadratures.

3.1 Traditional Angular Quadratures

This research focuses on angular quadratures used in the Cartesian coordinates system shown in Fig. 3.1. The unit directional vector $\vec{\Omega}$ can be described by the polar and azimuthal angles (θ, γ) or the directional cosines:

$$\mu = \Omega_x = \cos\gamma \sin\theta \ , \tag{3.1}$$

$$\eta = \Omega_y = \sin\gamma \sin\theta \ , \tag{3.2}$$

and

$$\xi = \Omega_z = \cos\theta \ . \tag{3.3}$$

Since $\vec{\Omega}$ is a unit vector, the squares of its directional cosines sum to unity:

$$\mu^2 + \eta^2 + \xi^2 = 1 \ . \tag{3.4}$$

An angular quadrature is a set of discrete directions (μ_m, η_m, ξ_m) with associated weights $w_m, m = 1 : M$. Quadrature directions with the same ξ are defined to be

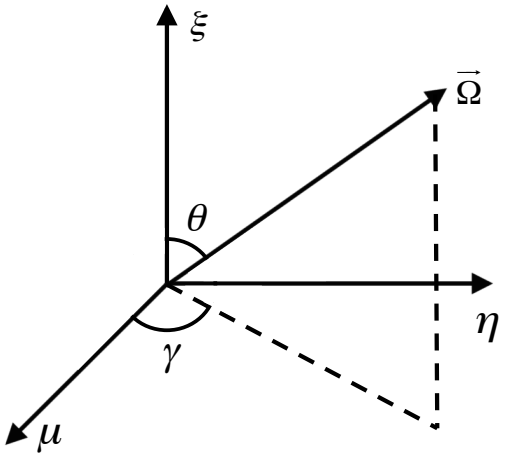

Figure 3.1: Cartesian coordinate system. Unit directional vector $\vec{\Omega}$ can be described by the polar and azimuthal angles (θ, γ) or the directional cosines (μ, η, ξ).

on the same polar level. Triangular angular quadratures have a triangular direction distribution i.e., the highest polar level (with ξ closest to unity) has one direction, the second highest has two, and so on. Rectangular angular quadratures have the same number of directions on each polar level. If the number of directions on each polar level is equal to the total number of polar levels, then the angular quadrature may be considered a square angular quadrature. We note that the new DFEM-based angular quadratures, in their current form, are not compatible with the algorithms most widely used for S_n transport calculations in cylindrical coordinates, because their directions are not aligned along polar levels. We leave the development of DFEM-based angular quadratures for S_n transport calculations in the cylindrical coordinates system as future work.

The directions and weights of traditional angular quadratures are typically generated to exactly integrate as high-degree spherical harmonics (SH) functions as possible over the global angular domain. An exception is the Quadruple Range (QR) angular quadrature family, which is generated to exactly integrate SH functions over

each octant.[7, 8] Therefore, traditional angular quadratures can exactly integrate the scattering source (Eqn. 2.36), and avoid introducing particle-conservation errors, even for problems with highly anisotropic scattering. However, traditional angular quadratures inaccurately form the angular flux moments (Eqn. 2.31) when the angular flux solution is not a smooth function over the entire angular domain, which occurs even for simple radiation transport problems. Traditional angular quadratures are also static (i.e., directions and weights are selected before run-time and kept constant throughout the solution process) and uniform (i.e., directions and weights cannot be added to local angular regions), which is computationally inefficient for radiation transport problems that may need additional angular resolution only for local angular regions.

3.1.1 Level Symmetric

Level Symmetric (LS) angular quadratures are triangular and rotationally invariant to 90° rotations about any axis.[1] Due to the strict symmetry constraints, there is only one degree of freedom in choosing the quadrature directions. An order-N (denoted S_N) LS angular quadrature contains $N(N+2)/8$ directions per octant. The weights are chosen to exactly integrate SH functions of as high-degree as possible over the global angular domain. However, negative weights are produced above the S_{22} LS angular quadrature. The S_{16} LS angular quadrature is shown in Fig. 3.2. LS angular quadratures produce non-uniform direction and weight distributions, which increase local integration error as discussed in Section 2.3.2.2. In addition, LS angular quadratures are designed to integrate smooth functions over the global angular domain, and thus poorly integrate functions over local angular regions.

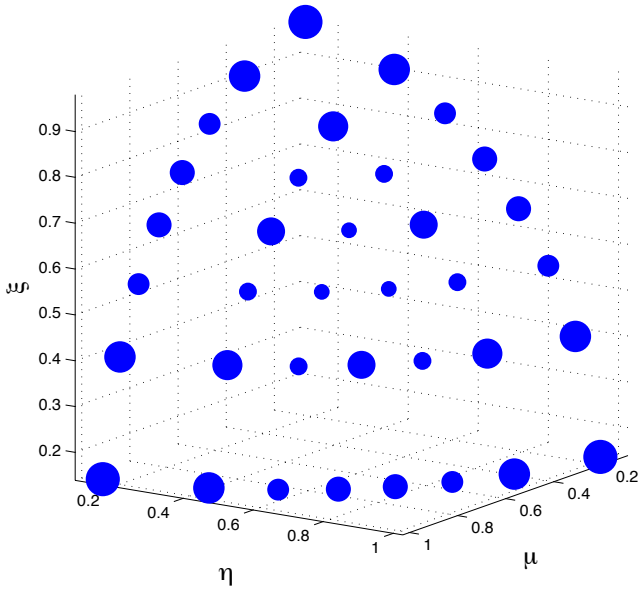

Figure 3.2: S_{16} Level Symmetric angular quadrature over the first octant. Weights are proportional to the dot area.

3.1.2 Gauss-Chebyshev

Gauss-Chebyshev (GC) angular quadratures consist of a one-dimensional (1D) Gauss quadrature over the polar domain, and a 1D Chebyshev quadrature over the azimuthal domain.[9] GC angular quadratures can be generated to be triangular or rectangular. GC angular quadratures can be generated for arbitrarily large numbers of directions without producing negative weights. The S_{16}-like GC angular quadrature is shown in Fig. 3.3. Fig. 3.4 shows the square GC angular quadrature containing eight polar levels, and Fig. 3.5 shows the rectangular GC angular quadrature containing eight polar levels with three quadrature directions per polar level. GC angular quadratures show more uniform direction and weight distributions than LS, which reduces local integration error. GC angular quadratures also produce directions on discrete polar levels, which makes them amenable for use in S_n transport calculations

in cylindrical coordinates.

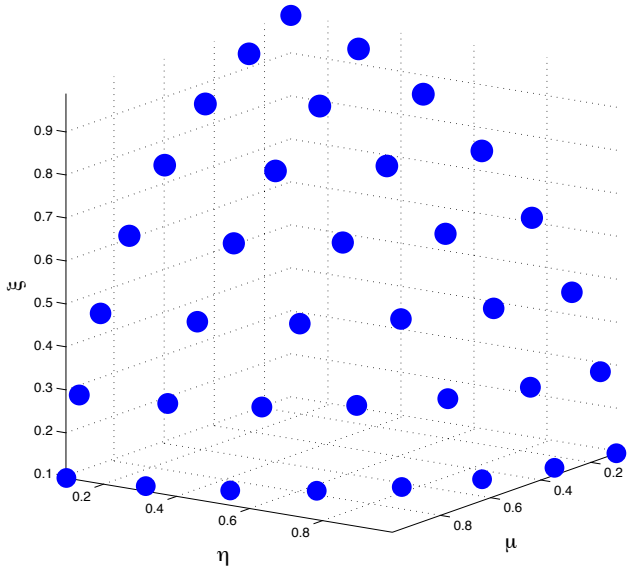

Figure 3.3: S_{16}-like Gauss-Chebyshev angular quadrature over the first octant. Weights are proportional to the dot area.

3.1.3 Quadruple Range

Quadruple Range (QR) angular quadratures exactly integrate SH functions of as high-degree as possible over each octant.[7, 8] Due to the algebraic complexity of solving the required non-linear equations, QR angular quadratures have so far been produced for only up to 18 polar levels and 36 azimuthal directions. The S_{16}-like QR angular quadrature is shown in Fig. 3.6. Fig. 3.7 shows the rectangular QR angular quadrature containing 18 polar levels with four quadrature directions per polar level. QR angular quadratures show less uniform direction and weight distributions than GC, with larger weights near the center of the octant. In addition, QR angular quadratures are only designed to accurately integrate smooth functions over entire octants, and thus may not have accurate sub-octant integration.

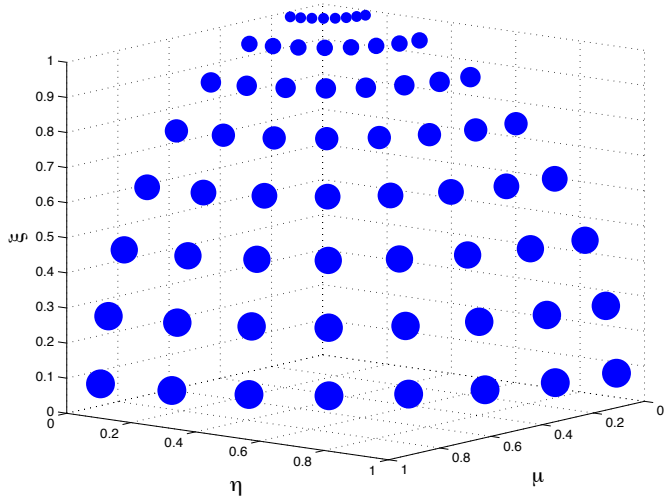

Figure 3.4: Square Gauss-Chebyshev angular quadrature containing eight polar levels over the first octant. Weights are proportional to the dot area.

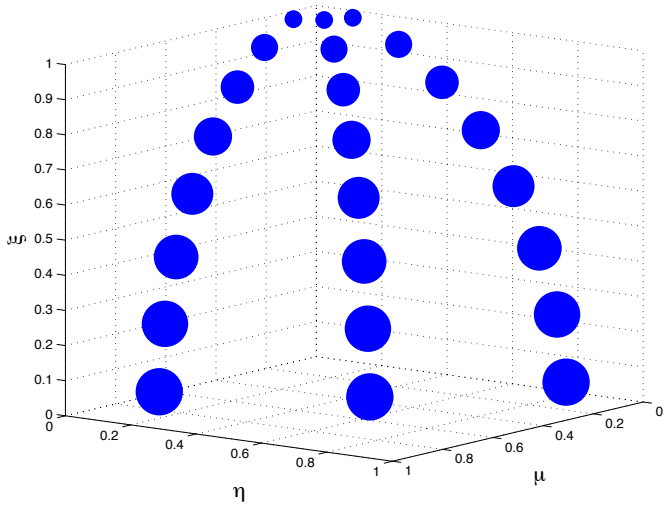

Figure 3.5: Rectangular Gauss-Chebyshev angular quadrature containing eight polar levels with three directions per polar level over the first octant. Weights are proportional to the dot area.

3.2 Discontinuous Finite Element Based Angular Quadratures

DFEM-based angular quadratures partition the global angular domain into a set of non-overlapping angular regions $\Delta\Omega_i, i = 1 : I$. We define DFEM basis functions

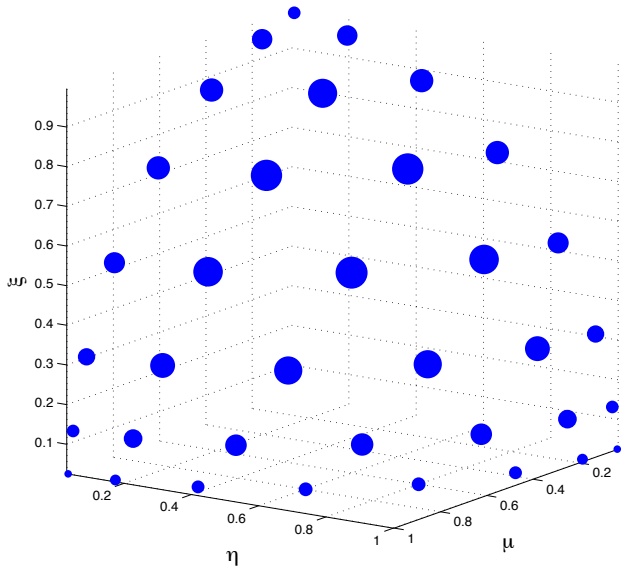

Figure 3.6: S_{16}-like Quadruple Range angular quadrature over the first octant. Weights are proportional to the dot area.

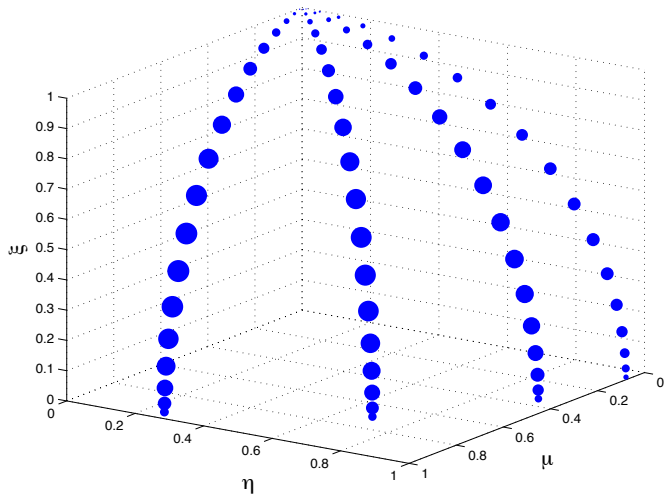

Figure 3.7: Rectangular Quadruple Range angular quadrature containing 18 polar levels with four directions per polar level over the first octant. Weights are proportional to the dot area.

in the direction cosines $b_{ij}\left(\vec{\Omega}\right), j = 1 : J$ over each $\Delta\Omega_i$, where J is the number of degrees of freedom. For example, linear discontinuous finite element (LDFE) basis

functions have four degrees of freedom, and are linear in the directional cosines:

$$b_{ij}\left(\vec{\Omega}\right) = c_j + c_{\mu,j}\mu + c_{\eta,j}\eta + c_{\xi,j}\xi \quad , \quad j = 1:4 \; . \tag{3.5}$$

We note b_{ij} is identically zero outside of $\Delta\Omega_i$. The b_{ij} unknowns (i.e., c-coefficients in Eqn. 3.5) are determined by requiring b_{ij} to be cardinal functions at J selected quadrature directions. For example, using LDFE basis functions requires solving the following linear system to determine the c-coefficients for each angular region:

$$\begin{bmatrix} 1 & \mu_1 & \eta_1 & \xi_1 \\ 1 & \mu_2 & \eta_2 & \xi_2 \\ 1 & \mu_3 & \eta_3 & \xi_3 \\ 1 & \mu_4 & \eta_4 & \xi_4 \end{bmatrix} \begin{bmatrix} c_1 & c_2 & c_3 & c_4 \\ c_{\mu,1} & c_{\mu,2} & c_{\mu,3} & c_{\mu,4} \\ c_{\eta,1} & c_{\eta,2} & c_{\eta,3} & c_{\eta,4} \\ c_{\xi,1} & c_{\xi,2} & c_{\xi,3} & c_{\xi,4} \end{bmatrix} = \begin{bmatrix} 1 & 0 & 0 & 0 \\ 0 & 1 & 0 & 0 \\ 0 & 0 & 1 & 0 \\ 0 & 0 & 0 & 1 \end{bmatrix} \; . \tag{3.6}$$

We expand the angular flux solution in each $\Delta\Omega_i$ using its DFEM basis functions:

$$\Psi_i\left(\vec{\Omega}\right) \approx \psi_i\left(\vec{\Omega}\right) \equiv \sum_{j=1}^{J} \Psi_{ij} b_{ij}\left(\vec{\Omega}\right) \; , \tag{3.7}$$

where Ψ_{ij} are the basis function expansion coefficients. Since b_{ij} are cardinal functions at the selected directions, Ψ_{ij} are equal to the angular flux solution evaluated at the selected directions:

$$\Psi_{ij} = \Psi_i\left(\vec{\Omega}_{ij}\right) \; . \tag{3.8}$$

We apply Eqn. 3.8 to 3.7 to obtain

$$\Psi_i\left(\vec{\Omega}\right) \approx \sum_{j=1}^{J} \Psi_i\left(\vec{\Omega}_{ij}\right) b_{ij}\left(\vec{\Omega}\right) \; . \tag{3.9}$$

We can now apply Eqn. 3.9 to the integration of the angular flux solution over each $\Delta\Omega_i$ to obtain

$$\int_{\Delta\Omega_i} d\Omega \Psi_i \left(\vec{\Omega}\right) \approx \sum_{j=1}^{J} \Psi \left(\vec{\Omega}_{ij}\right) w_{ij} \ , \tag{3.10}$$

where

$$w_{ij} = \int_{\Delta\Omega_i} d\Omega b_{ij} \left(\vec{\Omega}\right) \ . \tag{3.11}$$

The set of directions $\vec{\Omega}_{ij}$ and weights $w_{ij}, j = 1 : J$ forms the DFEM-based angular quadrature for $\Delta\Omega_i$.

DFEM-based angular quadratures have two main advantages over traditional angular quadratures. First, DFEM-based angular quadratures are designed to integrate functions over individual local angular regions. Therefore, their accuracy does not depend on the function being smooth across multiple local angular regions. In contrast, traditional angular quadratures (e.g., LS, GC and QR) are designed to integrate functions that are smooth over at least an entire octant. Therefore, DFEM-based angular quadratures should more accurately integrate non-smooth functions, such as the near-discontinuous angular flux solutions commonly produced in radiation transport problems of interest. Second, DFEM-based angular quadratures support local refinement (i.e., add directions to specific angular regions) by recursively partitioning only the angular regions requiring additional angular resolution. This increases the computational efficiency of radiation transport problems requiring additional angular resolution only for specific angular regions.

A potential drawback of DFEM-based angular quadratures is the inexact integration of high-degree SH functions over the global angular domain, producing particle-conservation errors when the scattering order is greater than the DFEM basis-function order. Another potential concern is that this same lack of exact integration of high-degree SH functions may cause the DFEM-based angular quadra-

tres to be less accurate than other angular quadratures for problems with relatively smooth solutions. However, as discussed in the results section, the integration error of high-degree SH functions rapidly decreases as we increase the number of quadrature directions. In fact, it decreases by a factor of 16 for every factor of 4 increase in the number of quadrature directions. Our limited testing demonstrates the particle-conservation error for a problem with anisotropic scattering is negligibly small compared to the error for a given quantity of interest.

3.2.1 Jarrell and Adams' Linear Discontinuous Finite Element Based Angular Quadratures Over Spherical Triangles

Jarrell and Adams developed DFEM-based angular quadratures using LDFE basis functions in the direction cosines defined over spherical triangular (ST) tessellations of the unit sphere surface [2, 3] as shown in Fig. 3.8. We term their angular quadratures as LDFE-ST angular quadratures. Fig. 3.9 shows the 64-point per octant LDFE-ST angular quadrature over the first octant of the unit sphere.

3.2.2 Extension to Alternative Tessellations

The LDFE-ST angular quadratures have hexagonal rings of directions that form, and much larger weights near the center of the octant as shown in Fig. 3.9. This type of non-uniformity increases local integration error by preferentially weighting angular regions with a higher density of directions or larger weights. In this dissertation, we investigate the use of spherical quadrilateral (SQ) tessellations of the unit sphere surface to produce more uniform direction and weight distributions. The use of SQs over the unit sphere has been successful in other applications, such as discontinuous Galerkin transport for weather modeling.[14] The reduction in local integration errors may result in more accurate angular flux moments for radiation transport problems with discontinuous (or nearly discontinuous) angular flux solutions.

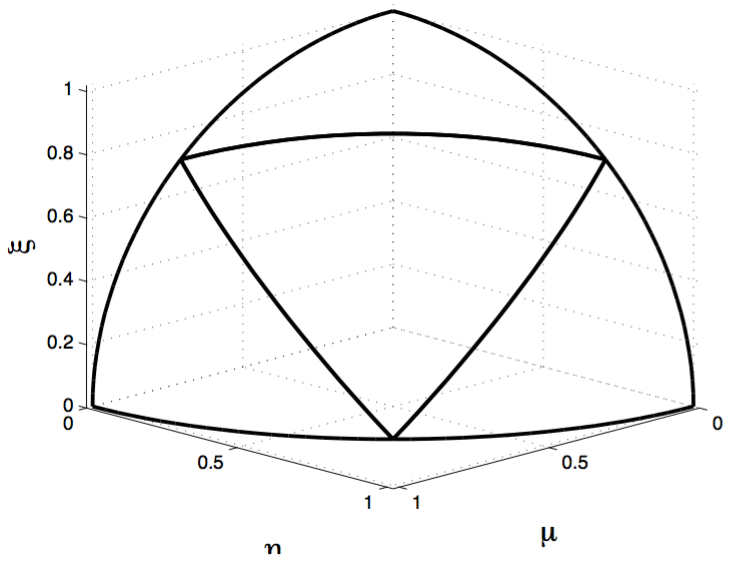

Figure 3.8: Spherical triangular tessellations over the first octant of the unit sphere.

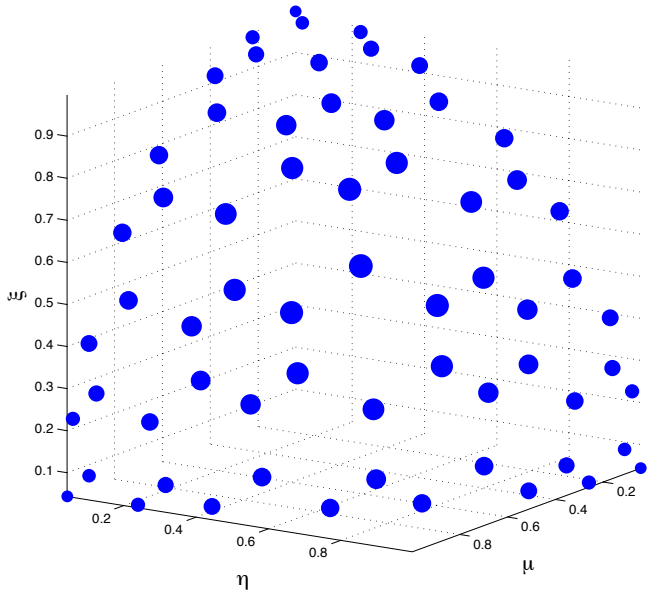

Figure 3.9: Sixty-four point per octant LDFE-ST angular quadrature over the first octant. Weights are proportional to the dot area.

3.2.3 Extension to Higher-Order DFEM Basis Functions

Jarrell and Adams only investigated the use of LDFE basis functions in the direction cosines. The research presented here extends the DFEM-based angular quadrature methodology to quadratic basis functions, thereby paving the way toward higher-order DFEM-based angular quadratures that exactly integrate higher-degree SH functions. This may be important for radiation transport problems with highly anisotropic scattering.

3.2.4 Improvement in Mapping Algorithms

Jarrell and Adams found the use of LDFE-ST angular quadratures in adaptive S_n algorithms to be limited by the accuracy of mapping algorithms required to pass the angular flux solution between spatial regions with differently-refined LDFE-ST angular quadratures. Their mapping algorithm produced over- and under-shoots (including negativities) in the mapped angular flux solution, and only preserved the normal partial current. The Jarrell and Adams mapping algorithm interpolates the incoming angular flux solution using the underlying LDFE basis functions in order to obtain the mapped angular flux solution:

$$\Psi_j\left(\vec{\Omega}_j\right) = \sum_{k=1}^{N_{\text{inc}}} \Psi_k\left(\vec{\Omega}_k\right) b_k\left(\vec{\Omega}_j\right) \quad , \quad j = 1 : N_{\text{map}} \; , \tag{3.12}$$

where j and k are the indices for the mapped and incoming angular flux solutions, respectively. The following conservation factor is then applied to ensure the normal partial current is preserved:

$$F_{\text{conserve}} = \frac{\sum_{k=1}^{N_{\text{inc}}} \left(\vec{\Omega}_k \cdot \vec{n}\right) w_k \Psi_k}{\sum_{j=1}^{N_{\text{map}}} \left(\vec{\Omega}_j \cdot \vec{n}\right) w_j \Psi_j} \; . \tag{3.13}$$

The research presented here aims to develop an "optimal" mapping algorithm, which should preserve both the shape and the angular moments of interest from the incoming angular flux solution.

3.3 Other Angular Quadratures

Many different angular quadratures have been proposed for integrating functions over the surface of the sphere in addition to those described above. In this subsection, we select some of these that have been considered for S_n radiation transport, and briefly discuss their key properties.[10, 11, 12, 13] We highlight some of their advantages over traditional angular quadratures, and their differences compared to DFEM-based angular quadratures.

3.3.1 Spence's Arbitrary Order, Non-Classical, Gauss-Type Angular Quadratures

Spence developed arbitrary order, non-classical, Gauss-type angular quadratures using a known method to generate the abscissae and weights for Gauss-type quadratures that exploits the relationship between orthogonal polynomials and the Gauss-type quadrature rules.[10] The Spence angular quadratures can be used to generate the Quadruple Range (QR) angular quadratures to large numbers of directions, by avoiding the need to iteratively solve the non-linear moment equations.[7, 8] The Spence angular quadratures may be generated over user-specified ranges of the azimuthal and polar angular domains,[10] suggesting accurate local SH function integration, and the possibility of local refinement. However, neither of those claims have been published to date.

3.3.2 Ahrens and Beylkin's Rotationally Invariant Angular Quadratures

Ahrens and Beylkin developed angular quadratures that are rotationally invariant under the icosahedral group.[11] The Ahrens and Beylkin angular quadratures

are similar to the Sobolev [15] angular quadratures, which are also invariant under certain rotational groups. The Ahrens and Beylkin angular quadratures project quadrature directions from the faces, edges and vertices of an iscosahedron onto the surface of the unit sphere, and are designed to integrate very high-degree SH functions (angular quadratures exactly integrating up to 210-degree SH functions have been generated).[11] Unlike the DFEM-based angular quadratures, the Ahrens and Beylkin angular quadratures do not appear amenable to local refinement.

3.3.3 Brown, Chang and Clouse's Locally Refined Quadrature Rules

Brown, Chang and Clouse developed angular quadratures which tessellate the surface of the unit sphere using triangles.[12] One quadrature direction is required to pass through the center of each triangle. A quadratic programming problem is solved to generate quadrature weights that exactly integrate SH functions up to a specified degree. The Brown, Chang and Clouse angular quadratures support local refinement by recursively partitioning specific triangles on the surface of the unit sphere. Unlike the DFEM-based angular quadratures, the Brown, Chang and Clouse angular quadratures are generated to exactly integrate SH functions over the global, rather than local, angular domain.

3.3.4 Fromowitz and Zeigler's Evenly-Spaced Angular Quadratures

Fromowitz and Zeigler developed angular quadratures with as uniform direction distribution as possible over the surface of the unit sphere.[13] The weight of each quadrature direction is equal to the surface area of the patch on the unit sphere formed by the space between each quadrature direction and their neighbors. The Fromowitz and Zeigler angular quadratures reduce ray effects for problems with strong streaming paths. Unlike DFEM-based angular quadratures, the Fromowitz and Zeigler angular quadratures only exactly integrate 0th-degree SH functions. Higher-

degree SH functions are integrated with 1st-order accuracy as a function of the number of directions. Therefore, the Fromowitz and Zeigler angular quadratures may not be suitable for problems with anisotropic scattering.

3.3.5 Summary

As previously discussed, many different angular quadratures have been proposed for integrating functions over the surface of the sphere. In this subsection, we discussed a few selected angular quadratures that have been considered for S_n radiation transport that possess certain characteristics that we seek for the new DFEM-based angular quadratures: accurate local SH integration, ability to be locally refined, and uniform quadrature direction and weight distributions.

4. DISCONTINUOUS FINITE ELEMENT BASED ANGULAR QUADRATURES OVER SPHERICAL QUADRILATERALS

In this section, we present the construction of a new family of discrete-ordinates (S_n) angular quadratures based on discontinuous finite element (DFEM) basis functions in the direction cosines. The angular domain is divided into cones subtended by spherical quadrilaterals (SQs) on the surface of the unit sphere. Linear and quadratic discontinuous finite element (LDFE and QDFE) basis functions in the direction cosines are defined over each SQ. The quadrature directions and weights are chosen to exactly integrate the underlying basis functions. We discuss advantages the new (LDFE-SQ and QDFE-SQ) angular quadratures have over previous DFEM-based angular quadratures, [2, 3] which can be attributed to having more uniform direction and weight distributions.

4.1 Angular Quadrature Construction

We present the construction of the new (LDFE-SQ and QDFE-SQ) angular quadratures which can be summarized in four steps: 1) tessellate the surface of the unit sphere into SQs; 2) select J quadrature directions for each SQ, where J is the number of degrees of freedom for a given DFEM basis function order; 3) solve for the basis function unknowns by requiring the basis functions to be cardinal functions at the selected quadrature directions; and 4) determine the quadrature weights, which are the basis functions integrated over each SQ.

4.1.1 Spherical Quadrilateral Tessellation

The construction of the new angular quadratures begins by inscribing a cube into the unit sphere as shown in Fig. 4.1. To maintain rotational symmetry between each

octant, the angular quadratures are generated over one octant then rotated to the rest. Therefore, we only consider the corner of the cube belonging to the first octant ($\mu > 0$, $\eta > 0$, and $\xi > 0$). The cube faces in each octant are divided into sub-squares as shown in Fig. 4.2, and projected onto the surface of the unit sphere to form SQs as shown in Fig. 4.3. The cone subtended by each SQ represents a unique partition of the angular domain. To maintain rotational symmetry within each octant, the angular quadratures are generated over one of the cube faces within each octant, then rotated to the rest. Therefore, we consider only the cube face perpendicular to the μ-axis in the first octant. We note the above symmetry requirements are imposed only for uniformly-refined angular quadratures. Locally-refined angular quadratures may select specific SQs to further partition.

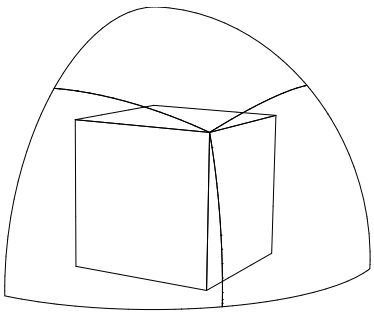

Figure 4.1: Corner of the cube inscribed into the first octant of the unit sphere.

4.1.2 Discontinuous Finite Element Basis Functions in the Direction Cosines

We define DFEM basis functions in the direction cosines $b_{ij}\left(\vec{\Omega}\right), j = 1 : J$ over each SQ i, where J is the number of degrees of freedom. For LDFE-SQ angular quadratures, we use LDFE basis functions in the direction cosines, which have four

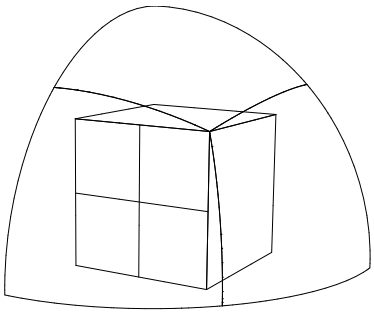

Figure 4.2: One of the cube faces divided into sub-squares.

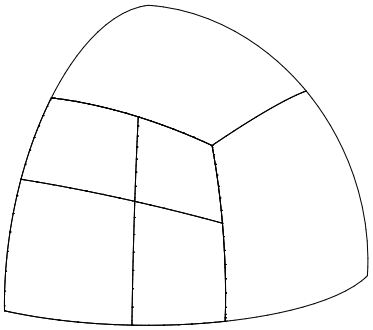

Figure 4.3: Sub-squares projected onto the surface of the unit sphere forming spherical quadrilaterals.

degrees of freedom, and are linear in the direction cosines:

$$b_{ij}\left(\vec{\Omega}\right) = c_j + c_{\mu,j}\mu + c_{\eta,j}\eta + c_{\xi,j}\xi \quad , \quad j = 1:4 \; . \tag{4.1}$$

We note that b_{ij} is identically zero outside of SQ i. The b_{ij} unknowns (i.e., c-coefficients in Eqn. 4.1) are determined by requiring b_{ij} to be cardinal functions at four selected quadrature directions. Therefore, we solve the following linear system

to find the c-coefficients for each SQ:

$$\begin{bmatrix} 1 & \mu_1 & \eta_1 & \xi_1 \\ 1 & \mu_2 & \eta_2 & \xi_2 \\ 1 & \mu_3 & \eta_3 & \xi_3 \\ 1 & \mu_4 & \eta_4 & \xi_4 \end{bmatrix} \begin{bmatrix} c_1 & c_2 & c_3 & c_4 \\ c_{\mu,1} & c_{\mu,2} & c_{\mu,3} & c_{\mu,4} \\ c_{\eta,1} & c_{\eta,2} & c_{\eta,3} & c_{\eta,4} \\ c_{\xi,1} & c_{\xi,2} & c_{\xi,3} & c_{\xi,4} \end{bmatrix} = \begin{bmatrix} 1 & 0 & 0 & 0 \\ 0 & 1 & 0 & 0 \\ 0 & 0 & 1 & 0 \\ 0 & 0 & 0 & 1 \end{bmatrix}, \tag{4.2}$$

Fig. 4.4 plots four sample LDFE basis functions over a SQ.

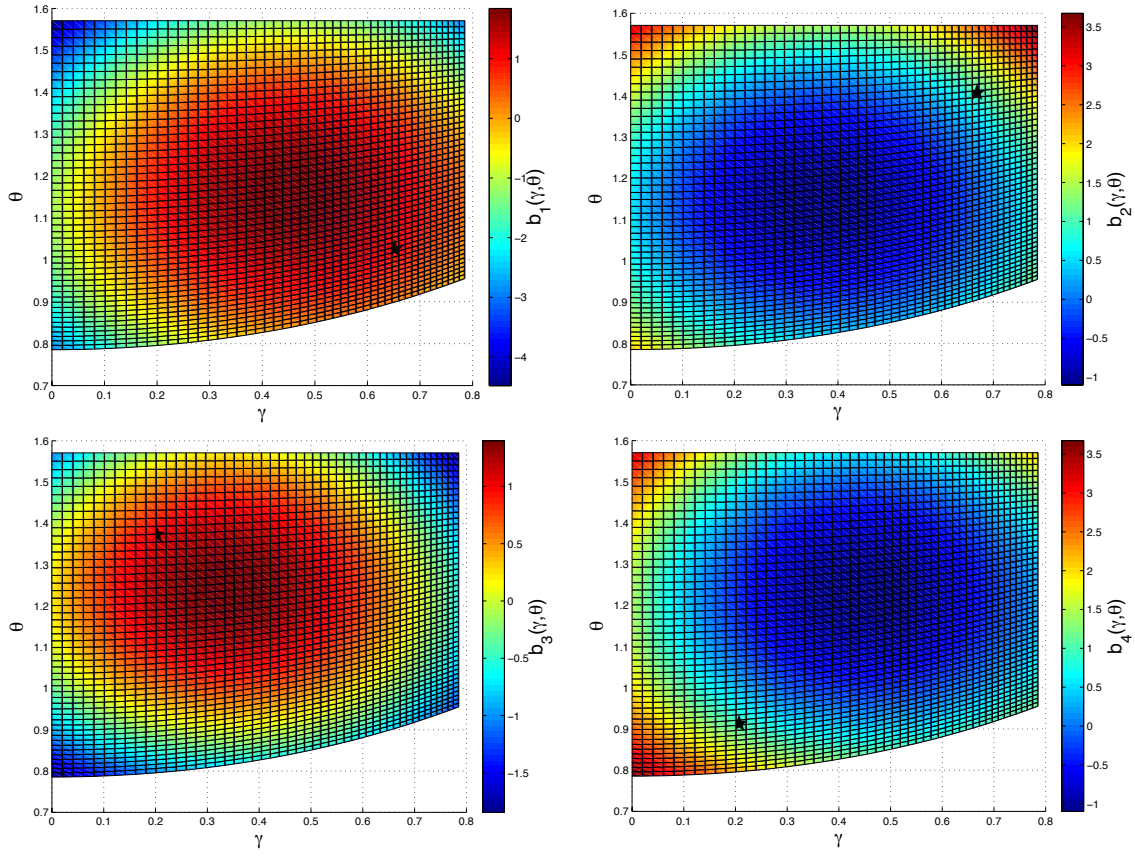

Figure 4.4: Sample linear discontinuous finite element basis functions in the direction cosines over a spherical quadrilateral. Stars indicate the quadrature direction associated with each basis function. While the basis functions sum to one at every point in the SQ, each individual basis function has negative values and values that exceed one.

For QDFE-SQ angular quadratures, we use QDFE basis functions in the direction cosines, which have nine degrees of freedom and are quadratic in the direction cosines:

$$b_{ij}\left(\vec{\Omega}\right) = c_j + c_{\mu,j}\mu + c_{\eta,j}\eta + c_{\xi,j}\xi + c_{\mu\eta,j}\mu\eta + c_{\mu\xi,j}\mu\xi \quad + \\ c_{\eta\xi,j}\eta\xi + c_{\xi^2,j}\xi^2 + c_{\mu^2-\eta^2,j}\left(\mu^2-\eta^2\right) \quad , \quad j = 1:9\ . \tag{4.3}$$

Again, b_{ij} is identically zero outside of SQ i, and the b_{ij} unknowns (i.e., c-coefficients in Eqn. 4.3) are determined by requiring b_{ij} to be cardinal functions at nine selected quadrature directions. Therefore, we solve the following linear system to find the c-coefficients for each SQ:

$$\begin{bmatrix} 1 & \mu_1 & \cdots & \mu_1^2-\eta_1^2 \\ 1 & \mu_2 & \cdots & \mu_2^2-\eta_2^2 \\ \vdots & \vdots & \ddots & \vdots \\ 1 & \mu_9 & \cdots & \mu_9^2-\eta_9^2 \end{bmatrix} \begin{bmatrix} c_1 & c_2 & \cdots & c_9 \\ c_{\mu,1} & c_{\mu,2} & \cdots & c_{\mu,9} \\ \vdots & \vdots & \ddots & \vdots \\ c_{\mu^2-\eta^2,1} & c_{\mu^2-\eta^2,2} & \cdots & c_{\mu^2-\eta^2,9} \end{bmatrix} = \\ \begin{bmatrix} 1 & 0 & \cdots & 0 \\ 0 & 1 & \ddots & 0 \\ \vdots & \vdots & \ddots & \vdots \\ 0 & 0 & \cdots & 1 \end{bmatrix}\ . \tag{4.4}$$

Figs. 4.5 and 4.6 plot nine sample QDFE basis functions over a SQ.

4.1.3 Weight Determination

As discussed in Section 3.2, the weight of each quadrature direction is the integral of its associated DFEM basis function (i.e., the basis function for which it is cardinal) over its SQ. We define local $(\tilde{x}, \tilde{y})$ coordinates over the cube face perpendicular to the μ-axis in the first octant as shown in Fig. A.1. The LDFE (Eqns. 4.1) and QDFE

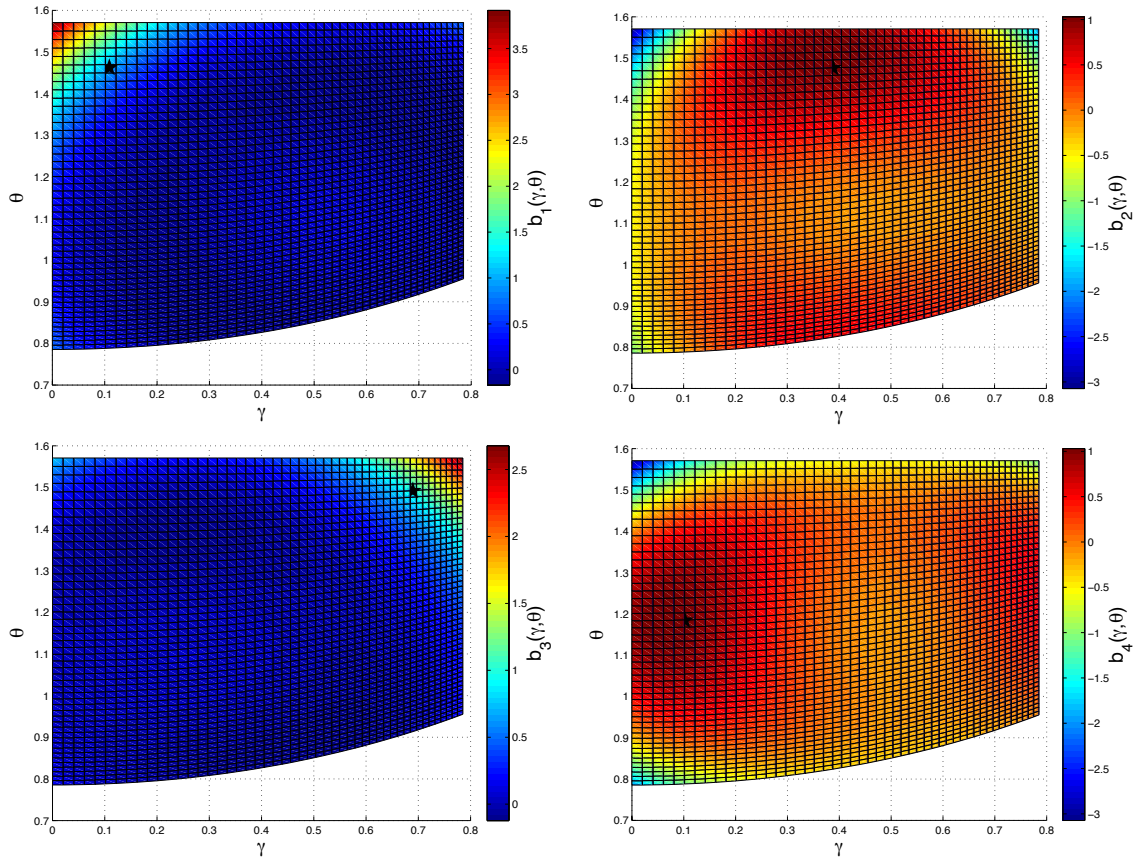

Figure 4.5: Sample quadratic discontinuous finite element basis functions in the direction cosines over a spherical quadrilateral (1-4). Stars indicate the quadrature direction associated with each basis function. While the basis functions sum to one at every point in the SQ, each individual basis function has negative values and values that exceed one.

(Eqn. 4.3) basis functions can be transformed to the $(\tilde{x}, \tilde{y})$ coordinates by using the following relationships derived in Appendix A.1:

$$\mu = \frac{a}{r} \,, \tag{4.5}$$

$$\eta = \frac{\tilde{x}}{r} \,, \tag{4.6}$$

and

$$\xi = \frac{\tilde{y}}{r} \ , \tag{4.7}$$

where $a = 1/\sqrt{3}$ and $r = \sqrt{\tilde{x}^2 + \tilde{y}^2 + a^2}$. The resulting LDFE basis functions are

$$b_{ij}\left(\tilde{x}, \tilde{y}\right) = c_j + c_{\mu,j}\frac{a}{r} + c_{\eta,j}\frac{\tilde{x}}{r} + c_{\xi,j}\frac{\tilde{y}}{r} \quad , \quad j = 1:4 \ , \tag{4.8}$$

and the resulting QDFE basis functions are

$$\begin{aligned} b_{ij}\left(\tilde{x}, \tilde{y}\right) = c_j + c_{\mu,j}\frac{a}{r} + c_{\eta,j}\frac{\tilde{x}}{r} + c_{\xi,j}\frac{\tilde{y}}{r} + c_{\mu\eta,j}\frac{a\tilde{x}}{r^2} + c_{\mu\xi,j}\frac{a\tilde{y}}{r^2} \quad + \\ c_{\eta\xi,j}\frac{\tilde{x}\tilde{y}}{r^2} + c_{\xi^2,j}\frac{\tilde{y}^2}{r^2} + c_{\mu^2-\eta^2}\frac{a^2 - \tilde{x}^2}{r^2} \quad , \quad j = 1:9 \ . \end{aligned} \tag{4.9}$$

The integration of the DFEM basis functions over each SQ i is performed over the sub-square SQ i is projected from in the $(\tilde{x}, \tilde{y})$ coordinates:

$$w_{ij} = \int_{\Delta\tilde{x}_i}\int_{\Delta\tilde{y}_i} d\tilde{x}d\tilde{y}|J|b_{ij}\left(\tilde{x}, \tilde{y}\right) \ , \tag{4.10}$$

where $J = a/r^3$ is the Jacobian mapping from the $(\tilde{x}, \tilde{y})$ coordinates to the surface of the unit sphere as derived in Appendix A.1. One-dimensional Gauss-Legendre quadratures (using 32 points, above which no changes to machine precision are observed) are used to perform the double integral in Eqn. 4.10. The sum of the weights over all octants is normalized to 4π.

4.1.4 Direction Determination

As discussed in Sections 4.1.2 and 4.1.3, the placement of the quadrature directions in each SQ fully determines its DFEM basis functions, which subsequently determines its weights. To determine the placement of the quadrature directions in each SQ, we divide each sub-square into sub-sub-squares as shown in Fig. 4.7. One

quadrature direction starting from the unit sphere origin is required to pass through each sub-sub-square as shown in Fig. 4.8. To reduce the degrees of freedom in the placement of the quadrature directions, each direction is required to lie on the radius of its sub-sub-square as shown in Fig. 4.9.

We use a multi-variate Secant method to iteratively place the quadrature directions such that each resulting weight equals the surface area of the SQ projected by its sub-sub-square. This results in a geometric angular quadrature, ensuring strictly positive weights and providing a physical significance to the weight distribution. We define the following ratio for each sub-sub-square i:

$$\rho_i = \frac{d}{L} \, , \tag{4.11}$$

where d is the distance of the quadrature direction along the sub-sub-square radius, and L is the total length of the sub-sub-square radius. The multi-variate Secant method begins by making an initial guess for the sub-sub-square ratios $\rho_i^{[0]}$ (e.g., 0.5), and calculating the resulting weights $w_i^{[0]}$. Next, the weights are re-calculated by individually perturbing each ratio by a small factor ϵ (e.g., 0.25):

$$\rho_i^{[1]} = \rho_i^{[0]} + \epsilon \, . \tag{4.12}$$

The initial $w_i^{[0]}$ and new $w_i^{[1]}$ weights are stored into a weight matrix:

$$W^{[1]} = \begin{bmatrix} w_1^{[0]} & w_2^{[0]} & \cdots & w_J^{[0]} \\ w_{11}^{[1]} & w_{21}^{[1]} & \cdots & w_{J1}^{[1]} \\ \vdots & \vdots & \ddots & \vdots \\ w_{1J}^{[1]} & w_{2J}^{[1]} & \cdots & w_{JJ}^{[1]} \end{bmatrix} \, , \tag{4.13}$$

where w_{ij} is the quadrature weight in sub-sub-square i produced by perturbing the ratio of sub-sub-square j. We consider ratio i to be converged if row i and the first row in the weight matrix are equal. If no ratios are converged, then we solve the following linear system to get the change in ratios δ_i for the next iteration:

$$\begin{bmatrix} \frac{w_{11}^{[1]}-w_1^{[0]}}{\rho_1^{[1]}-\rho_1^{[0]}} & \frac{w_{12}^{[1]}-w_1^{[0]}}{\rho_2^{[1]}-\rho_2^{[0]}} & \cdots & \frac{w_{1J}^{[1]}-w_1^{[0]}}{\rho_J^{[1]}-\rho_J^{[0]}} \\ \frac{w_{21}^{[1]}-w_2^{[0]}}{\rho_1^{[1]}-\rho_1^{[0]}} & \frac{w_{22}^{[1]}-w_2^{[0]}}{\rho_2^{[1]}-\rho_2^{[0]}} & \cdots & \frac{w_{2J}^{[1]}-w_2^{[0]}}{\rho_J^{[1]}-\rho_J^{[0]}} \\ \vdots & \vdots & \ddots & \vdots \\ \frac{w_{J1}^{[1]}-w_J^{[0]}}{\rho_1^{[1]}-\rho_1^{[0]}} & \frac{w_{J2}^{[1]}-w_J^{[0]}}{\rho_2^{[1]}-\rho_2^{[0]}} & \cdots & \frac{w_{JJ}^{[1]}-w_J^{[0]}}{\rho_J^{[1]}-\rho_J^{[0]}} \end{bmatrix} \begin{bmatrix} \delta_1 \\ \delta_2 \\ \vdots \\ \delta_J \end{bmatrix} = \begin{bmatrix} SA_1 - w_1^{[0]} \\ SA_2 - w_2^{[0]} \\ \vdots \\ SA_J - w_J^{[0]} \end{bmatrix}, \tag{4.14}$$

where SA_i is the surface area of the SQ projected by sub-sub-square i. If one or more ratios are converged, we eliminate the corresponding rows and columns from Eqn. 4.14. Lastly, we calculate the ratios for the next iteration:

$$\rho_i^{[2]} = \rho_i^{[1]} + \delta_i \ . \tag{4.15}$$

The multi-variate Secant iterations are repeated until $|\delta_i|$ is less than the user-prescribed tolerance for all sub-sub-squares. We note convergence becomes more difficult with refinement. We found the algorithm described here can converge to $|\delta_i| \leq 10^{-7}$ for up to 161,376 and 146,016 directions over all octants for the LDFE-SQ and QDFE-SQ angular quadratures, respectively.

4.1.5 Spherical Quadrilateral Tessellation for Uniform Weights

As discussed in Section 3.2, a uniform weight distribution is desired to reduce local integration errors. Therefore, we set the sub-sub-square divisions in the $(\tilde{x}, \tilde{y})$ coordinates such that the surface areas of their projected SQ are as uniform as possible. We group sub-sub-squares for each cube face within an octant into rings

starting from the upper-right corner as shown in Fig. 4.10. The ideal SQ surface area producing a uniform weight distribution is

$$SA_{\text{ideal, sq}} = \frac{\pi}{6N_{\text{sq}}} \ , \tag{4.16}$$

where N_{sq} is the number of sub-sub-squares on the cube face within an octant, and $\pi/6 = 4\pi/(8 \times 3)$ is the total solid angle associated with the cube face within an octant. Therefore, the ideal surface area for each ring i is

$$SA_{\text{ideal, i}} = SA_{\text{ideal, sq}} N_{\text{sq, i}} \ , \tag{4.17}$$

where $N_{\text{sq, i}}$ is the number of sub-sub-squares in ring i. The sub-sub-square divisions are set such that Eqn. 4.17 is satisfied for each ring. However, Eqn. 4.16 may not be satisfied for each sub-sub-square since the SQ surface areas may differ within a ring. The resulting maximum-to-minimum (resp., maximum-to-average) weight ratios are no greater than 1.3 (resp., 1.1) for up to 161,376 and 146,016 directions over all octants for LDFE-SQ and QDFE-SQ angular quadratures, respectively.

4.1.6 Refinement Strategy

For uniformly-refined LDFE-SQ and QDFE-SQ angular quadratures, we specify a refinement parameter n, and divide each of the three cube faces within an octant into $(n+1)^2$ sub-squares. The number of quadrature directions per octant as a function of n for LDFE-SQ and QDFE-SQ angular quadratures are

$$N_{\text{dirs,oct}}^{\text{LDFE-SQ}} = 12\,(n+1)^2 \ , \tag{4.18}$$

and

$$N_{\text{dirs,oct}}^{\text{QDFE-SQ}} = 27\,(n+1)^2 \ , \tag{4.19}$$

respectively. Table 4.1 shows the number of LDFE-SQ and QDFE-SQ angular quadrature directions per octant as a function of n. The LDFE-ST and LS angular quadrature direction counts are also provided for comparison. For LDFE-ST, the number of directions per octant as a function of n is given by

$$N_{\text{dirs,oct}}^{\text{LDFE-ST}} = 4\,(n+1)^2 \ , \tag{4.20}$$

where for each n the base triangle per octant is divided into $(n+1)^2$ triangles. For LS, we use the standard refinement parameter definition for LS-like angular quadratures [1] given by

$$N_{\text{dirs,oct}}^{\text{LS}} = \frac{n\,(n+1)}{8} \ , \tag{4.21}$$

where n must be an even number between 2 and 24 (highest n with strictly positive weights). We see major differences between the direction counts per octant for the DFEM and LS angular quadratures for each n, which highlights the difficulty in establishing a common refinement parameter for different angular quadratures.

For locally-refined LDFE-SQ and QDFE-SQ angular quadratures, we select specific sub-squares to refine. The refinement of an LDFE-SQ sub-square divides it into four sub-squares by using the old sub-sub-square divisions as the new sub-square divisions. Similarly, the refinement of a QDFE-SQ sub-square divides it into nine sub-squares. We define the original sub-square as the parent, and the new sub-squares it produces as the daughters.

Table 4.1: Number of directions per octant for LDFE-SQ, QDFE-SQ, LDFE-ST and LS as a function of refinement parameter n.

n	LDFE-SQ	QDFE-SQ	LDFE-ST	LS
0	12	27	4	NA
1	48	108	16	NA
2	108	243	36	1
3	192	432	64	NA
4	300	675	100	3
5	432	972	144	NA
6	588	1323	196	6
7	768	1728	256	NA
8	972	2028	324	10
9	1200	2700	400	NA
10	1452	3267	484	15
25	8112	18252	2704	NA
40	20172	45387	6724	NA

4.2 Comparison of New and Previous DFEM-Based Angular Quadratures

As discussed in Section 3.3, the previous DFEM-based (LDFE-ST) angular quadratures developed by Jarrell and Adams [2, 3] used spherical triangular tessellations of the unit sphere surface, which produced non-uniform direction and weight distributions. The LDFE-ST angular quadratures formed hexagonal rings of directions with much larger weights near the center of the octant as shown in Fig. 3.9. Fig. 4.11 shows the 108-point per octant LDFE-SQ and QDFE-SQ angular quadratures, which have much more uniform direction distributions than LDFE-ST. Additionally, as discussed in Section 4.1.5, the LDFE-SQ and QDFE-SQ angular quadratures have a maximum-to-minimum weight ratio of no greater than 1.3 - significantly lower than 5.1 for LDFE-ST. We note that the LDFE-SQ angular quadratures appear to have a more uniform direction distribution than QDFE-SQ. This is a result of the direction placement strategy discussed in Section 4.1.4. While the non-uniformity of the

QDFE-SQ direction placement could conceivably reduce accuracy in some problems, we observed no negative impact on the results provided in Section 6.

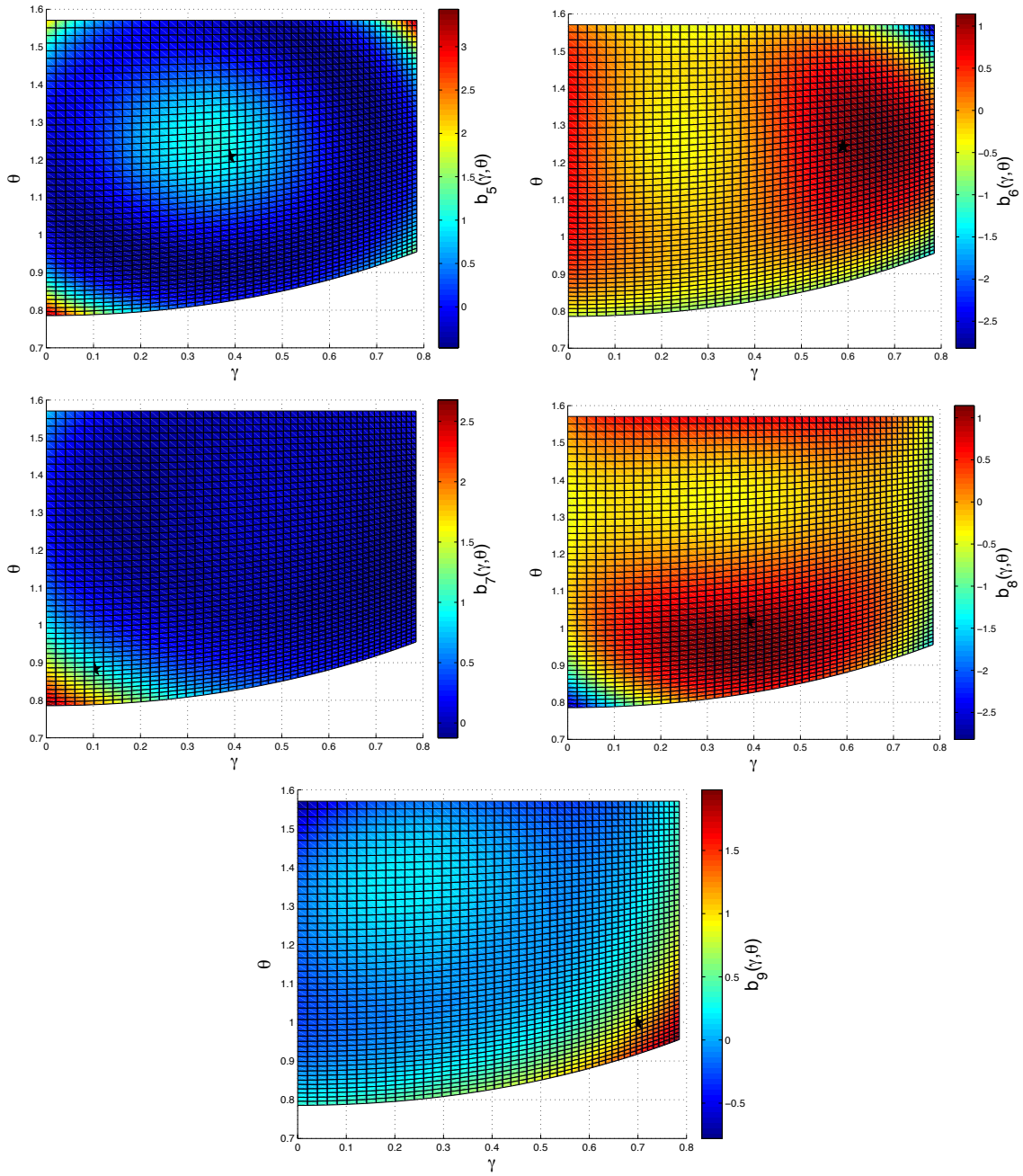

Figure 4.6: Sample quadratic discontinuous finite element basis functions in the direction cosines over a spherical quadrilateral (5-9). Stars indicate the quadrature direction associated with each basis function. While the basis functions sum to one at every point in the SQ, each individual basis function has negative values and values that exceed one.

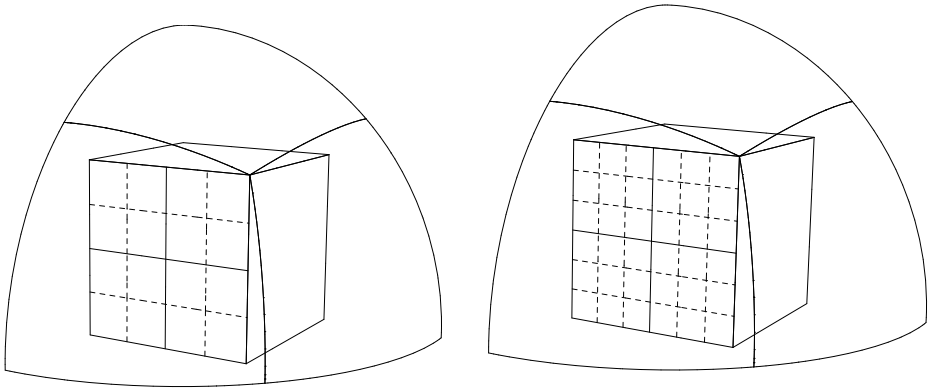

Figure 4.7: LDFE-SQ (left) and QDFE-SQ (right) sub-sub-square divisions are delineated by dotted lines.

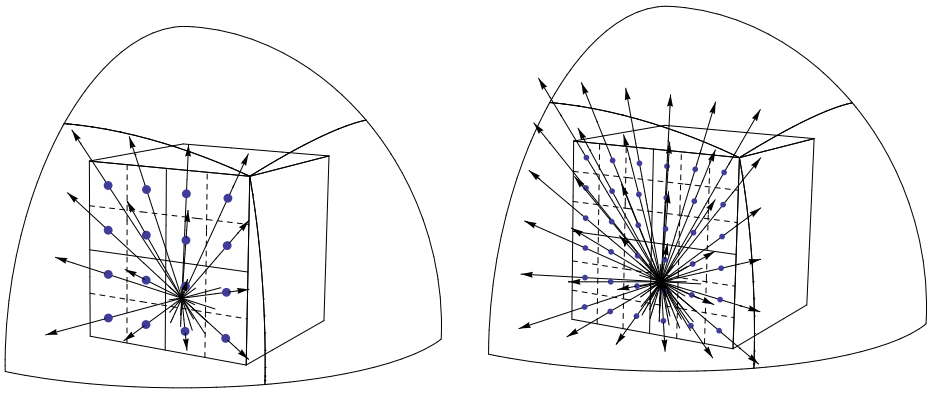

Figure 4.8: LDFE-SQ (left) and QDFE-SQ (right) directions are indicated by the arrows. One quadrature direction is required to pass through each sub-sub-square.

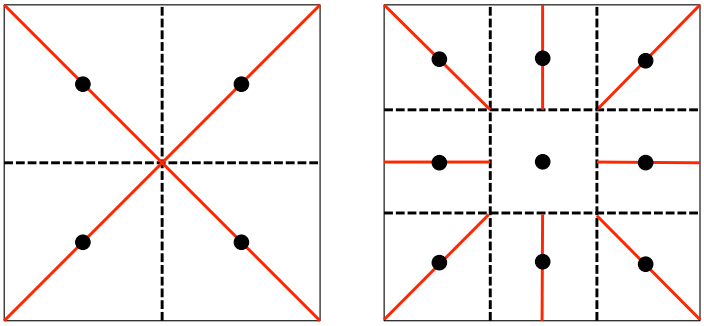

Figure 4.9: LDFE-SQ (left) and QDFE-SQ (right) sub-sub-square radii delineated by red lines. One quadrature direction (indicated by the black dots) must pass through each sub-sub-square radii.

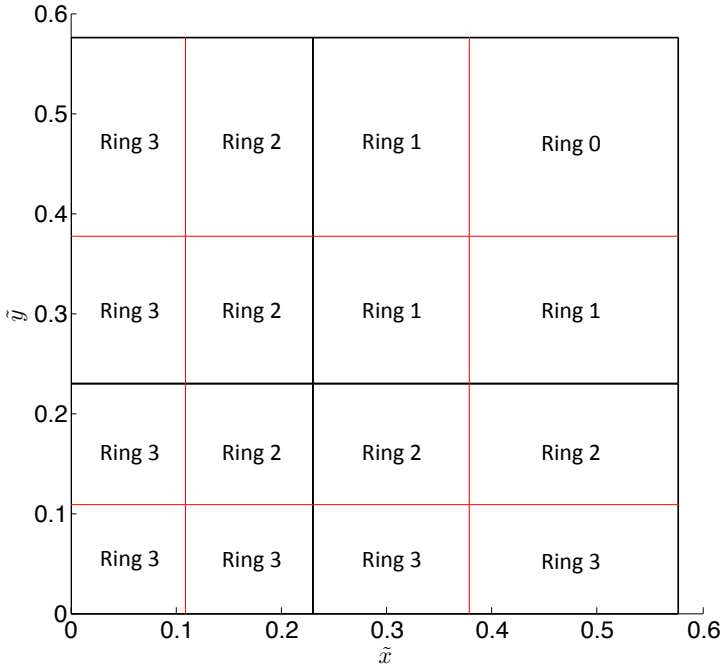

Figure 4.10: Sub-square (black lines) and sub-sub-square (red lines) divisions are set such that the weight of each ring of sub-sub-squares equals the ideal weight for a uniform sub-sub-square spherical quadrilateral surface area distribution.

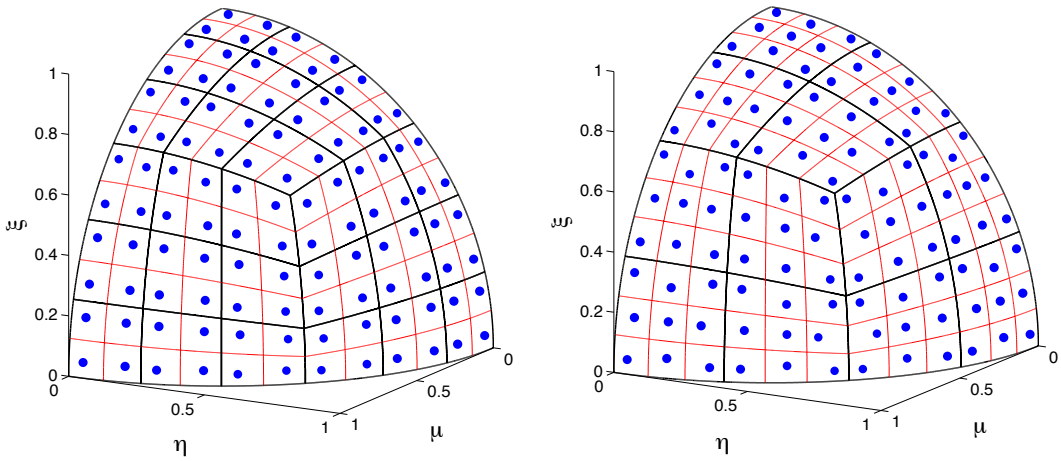

Figure 4.11: 108-point per octant LDFE-SQ (left) and QDFE-SQ (right) angular quadratures. Sub-square and sub-sub-square divisions are delineated by the black and red lines, respectively. Weights are proportional to the dot area.

5. MAPPING

In this section, we present a new mapping algorithm for passing the angular flux solution between spatial regions with differently-refined DFEM-based angular quadratures. As discussed in Section 3.2.4, an "optimal" mapping algorithm should preserve both the shape and the angular moments of interest from the incoming solution. We present a new mapping algorithm which is nearly "optimal" for mapping smooth solutions away from octant boundaries (small pointwise errors are introduced into the mapped solution even when the incoming solution lives in the underlying DFEM basis space, due to the preservation of the higher angular moments). However, over and under-shoots (including negativities) occur when mapping near solution discontinuities and octant boundaries. To address these instances, we present a new fix-up algorithm that uses multi-objective optimization (MOOP) to ensure that the mapped solution satisfies a set of prescribed limits. The mapping exactly preserves the 0th angular moment of the incoming solution while preserving the higher angular moments of interest as well as possible.

5.1 Mapping Algorithm Derivation

Mapping algorithms are required to pass the angular flux solution between spatial regions with differently-refined DFEM-based angular quadratures. Figs. 5.1 and 5.2 illustrate mapping between the parent and daughter sub-squares (defined in Section 4.1.6) for LDFE-SQ and QDFE-SQ angular quadratures, respectively. We define coarse-to-fine mapping as passing the solution from a parent sub-square to its daughters, and fine-to-coarse mapping as passing the solution from a group of daughter sub-squares to their common parent. The mapping algorithms presented in this section map across only one refinement level but can be recursively applied

to map across multiple refinement levels. An "optimal" mapping algorithm should preserve both the shape and the angular moments of interest from the incoming solution. The following equality, if it can be enforced, ensures the mapped solution $\Psi_{\text{map},j}, j = 1 : N_{\text{map}}$ preserves the angular moments of interest from the incoming solution $\Psi_{\text{inc},k}, k = 1 : N_{\text{inc}}$:

$$\sum_{j=1}^{N_{\text{map}}} w_{\text{map},j} Y_{ln}\left(\vec{\Omega}_{\text{map},j}\right) \Psi_{\text{map},j} = \sum_{k=1}^{N_{\text{inc}}} w_{\text{inc},k} Y_{ln}\left(\vec{\Omega}_{\text{inc},k}\right) \Psi_{\text{inc},k} \ , \tag{5.1}$$

where $(w_{\text{map},j}, \vec{\Omega}_{\text{map},j}), j = 1 : N_{\text{map}}$ is the angular quadrature for the mapped solution, $(w_{\text{inc},k}, \vec{\Omega}_{\text{inc},k}), k = 1 : N_{\text{inc}}$ is the angular quadrature for the incoming solution, and $Y_{ln}(\vec{\Omega})$ is the spherical harmonic (SH) function for the (l, n)-th angular moment. For LDFE-SQ angular quadratures, we are interested in preserving the 0th and 1st angular moments since, as discussed in Section 6.1, the LDFE-SQ angular quadratures exactly integrate the 0th and 1st-degree SH functions. For QDFE-SQ angular quadratures, we are interested in preserving the 0th through 2nd angular moments since the QDFE-SQ angular quadratures exactly integrate the 0th through 2nd-degree SH functions.

5.1.1 Fine-to-Coarse Mapping

For LDFE-SQ fine-to-coarse mapping, we have four equations (Eqn. 5.1 preserving the 0th and 1st angular moments) and four unknowns in the mapped solution,

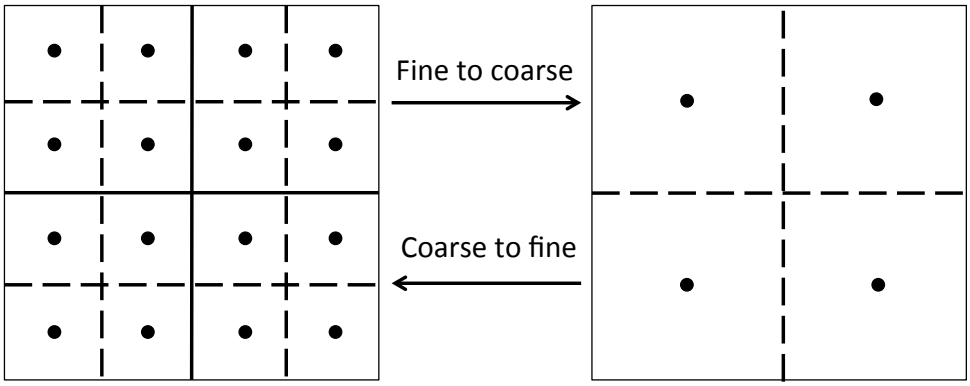

Figure 5.1: LDFE-SQ mapping between a parent sub-square and its daughter sub-squares. Sub-squares and sub-sub-squares are delineated by solid and dotted lines, respectively. Dots indicate quadrature directions.

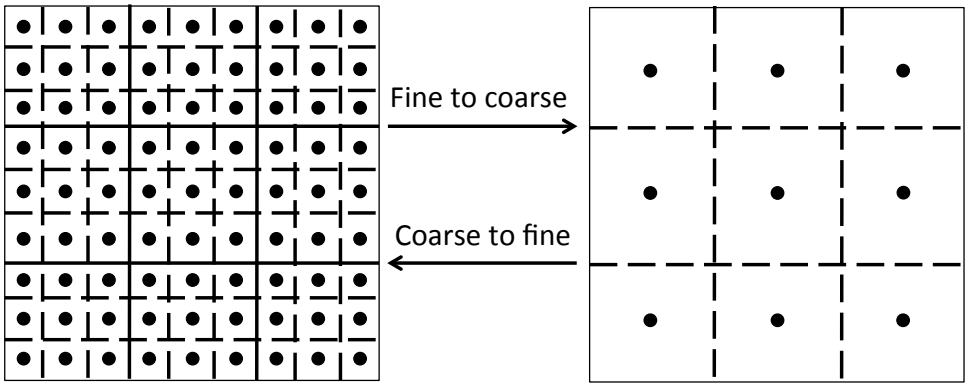

Figure 5.2: QDFE-SQ mapping between a parent sub-sqaure and its daughter sub-squares. Sub-squares and sub-sub-squares are delineated by solid and dotted lines, respectively. Dots indicate quadrature directions.

which results in the following linear system:

$$\begin{bmatrix} w_{c,1} & \cdots & w_{c,4} \\ w_{c,1}\mu_{c,1} & \cdots & w_{c,4}\mu_{c,4} \\ w_{c,1}\eta_{c,1} & \cdots & w_{c,4}\eta_{c,4} \\ w_{c,1}\xi_{c,1} & \cdots & w_{c,4}\xi_{c,4} \end{bmatrix} \begin{bmatrix} \Psi_{c,1} \\ \Psi_{c,2} \\ \Psi_{c,3} \\ \Psi_{c,4} \end{bmatrix} = \begin{bmatrix} \sum_{m=1}^{16} w_{f,m}\Psi_{f,m} \\ \sum_{m=1}^{16} w_{f,m}\mu_{f,m}\Psi_{f,m} \\ \sum_{m=1}^{16} w_{f,m}\eta_{f,m}\Psi_{f,m} \\ \sum_{m=1}^{16} w_{f,m}\xi_{f,m}\Psi_{f,m} \end{bmatrix}, \tag{5.2}$$

where f and c denote the fine (incoming) and coarse (mapped) angular quadrature quantities, respectively. Eqn. 5.2 is solved for the mapped solution $\Psi_{c,n}, n = 1:4$.

For QDFE-SQ fine-to-coarse mapping, we have nine equations (Eqn. 5.1 preserving the 0th through 2nd angular moments) and nine unknowns in the mapped solution, which results in the following linear system:

$$\begin{bmatrix} w_{c,1} & \cdots & w_{c,9} \\ w_{c,1}\mu_{c,1} & \cdots & w_{c,9}\mu_{c,9} \\ w_{c,1}\eta_{c,1} & \cdots & w_{c,9}\eta_{c,9} \\ w_{c,1}\xi_{c,1} & \cdots & w_{c,9}\xi_{c,9} \\ w_{c,1}\mu_{c,1}\eta_{c,1} & \cdots & w_{c,9}\mu_{c,9}\eta_{c,9} \\ w_{c,1}\mu_{c,1}\xi_{c,1} & \cdots & w_{c,9}\mu_{c,9}\xi_{c,9} \\ w_{c,1}\eta_{c,1}\xi_{c,1} & \cdots & w_{c,9}\eta_{c,9}\xi_{c,9} \\ w_{c,1}\xi_{c,1}^2 & \cdots & w_{c,9}\xi_{c,9}^2 \\ w_{c,1}\left(\mu_{c,1}^2 - \eta_{c,1}^2\right) & \cdots & w_{c,9}\left(\mu_{c,9}^2 - \eta_{c,9}^2\right) \end{bmatrix} \begin{bmatrix} \Psi_{c,1} \\ \Psi_{c,2} \\ \Psi_{c,3} \\ \Psi_{c,4} \\ \Psi_{c,5} \\ \Psi_{c,6} \\ \Psi_{c,7} \\ \Psi_{c,8} \\ \Psi_{c,9} \end{bmatrix} = \tag{5.3}$$

$$\begin{bmatrix} \sum_{m=1}^{81} w_{f,m}\Psi_{f,m} \\ \sum_{m=1}^{81} w_{f,m}\mu_{f,m}\Psi_{f,m} \\ \sum_{m=1}^{81} w_{f,m}\eta_{f,m}\Psi_{f,m} \\ \sum_{m=1}^{81} w_{f,m}\xi_{f,m}\Psi_{f,m} \\ \sum_{m=1}^{81} w_{f,m}\mu_{f,m}\eta_{f,m}\Psi_{f,m} \\ \sum_{m=1}^{81} w_{f,m}\mu_{f,m}\xi_{f,m}\Psi_{f,m} \\ \sum_{m=1}^{81} w_{f,m}\eta_{f,m}\xi_{f,m}\Psi_{f,m} \\ \sum_{m=1}^{81} w_{f,m}\xi_{f,m}^2\Psi_{f,m} \\ \sum_{m=1}^{81} w_{f,m}\left(\mu_{f,m}^2 - \eta_{f,m}^2\right)\Psi_{f,m} \end{bmatrix},$$

where f and c denote the fine (incoming) and coarse (mapped) angular quadrature

quantities, respectively. Eqn. 5.3 is solved for the mapped solution $\Psi_{c,n}, n = 1:9$.

5.1.2 Coarse-to-Fine Mapping

For LDFE-SQ coarse-to-fine mapping, we have four equations (Eqn. 5.1 preserving the 0th and 1st angular moments) and 16 unknowns in the mapped solution, which results in an under-determined system. We close the system by projecting the fine solution onto the coarse LDFE basis functions:

$$\Psi_{f,m} = \sum_{n=1}^{4} \tilde{\Psi}_{c,n} b_{c,n} \left(\vec{\Omega}_{f,m} \right) \quad , \quad m = 1:16 \; . \tag{5.4}$$

Eqn. 5.4 is applied to the four equations resulting in the following linear system:

$$\begin{bmatrix} \sum_{m=1}^{16} w_{f,m} b_{c,1} \left(\vec{\Omega}_{f,m} \right) & \cdots & \sum_{m=1}^{16} w_{f,m} b_{c,4} \left(\vec{\Omega}_{f,m} \right) \\ \sum_{m=1}^{16} w_{f,m} \mu_{f,m} b_{c,1} \left(\vec{\Omega}_{f,m} \right) & \cdots & \sum_{m=1}^{16} w_{f,m} \mu_{f,m} b_{c,4} \left(\vec{\Omega}_{f,m} \right) \\ \sum_{m=1}^{16} w_{f,m} \eta_{f,m} b_{c,1} \left(\vec{\Omega}_{f,m} \right) & \cdots & \sum_{m=1}^{16} w_{f,m} \eta_{f,m} b_{c,4} \left(\vec{\Omega}_{f,m} \right) \\ \sum_{m=1}^{16} w_{f,m} \xi_{f,m} b_{c,1} \left(\vec{\Omega}_{f,m} \right) & \cdots & \sum_{m=1}^{16} w_{f,m} \xi_{f,m} b_{c,4} \left(\vec{\Omega}_{f,m} \right) \end{bmatrix} \begin{bmatrix} \tilde{\Psi}_{c,1} \\ \tilde{\Psi}_{c,2} \\ \tilde{\Psi}_{c,3} \\ \tilde{\Psi}_{c,4} \end{bmatrix} = \begin{bmatrix} \sum_{n=1}^{4} w_{c,n} \Psi_{c,n} \\ \sum_{n=1}^{4} w_{c,n} \mu_{c,n} \Psi_{c,n} \\ \sum_{n=1}^{4} w_{c,n} \eta_{c,n} \Psi_{c,n} \\ \sum_{n=1}^{4} w_{c,n} \xi_{c,n} \Psi_{c,n} \end{bmatrix} . \tag{5.5}$$

Eqn. 5.5 is solved for $\tilde{\Psi}_{c,n}, n = 1:4$, which are inserted back into Eqn. 5.4 to obtain the mapped solution $\Psi_{f,m}, m = 1:16$.

For QDFE-SQ coarse-to-fine mapping, we have nine equations (Eqn. 5.1 preserving the 0th through 2nd angular moments) and 81 unknowns in the mapped solution, which results in an under-determined system. We again close the system

by projecting the fine solution onto the coarse QDFE basis functions:

$$\Psi_{f,m} = \sum_{n=1}^{9} \tilde{\Psi}_{c,n} b_{c,n} \left(\vec{\Omega}_{f,m} \right) \quad , \quad m = 1:81 \; . \tag{5.6}$$

Eqn. 5.6 is applied to the nine equations resulting in the following linear system:

$$\begin{bmatrix} \sum_{m=1}^{81} w_{f,m} b_{c,1} \left(\vec{\Omega}_{f,m} \right) & \cdots & \sum_{m=1}^{81} w_{f,m} b_{c,9} \left(\vec{\Omega}_{f,m} \right) \\ \sum_{m=1}^{81} w_{f,m} \mu_{f,m} b_{c,1} \left(\vec{\Omega}_{f,m} \right) & \cdots & \sum_{m=1}^{81} w_{f,m} \mu_{f,m} b_{c,9} \left(\vec{\Omega}_{f,m} \right) \\ \sum_{m=1}^{81} w_{f,m} \eta_{f,m} b_{c,1} \left(\vec{\Omega}_{f,m} \right) & \cdots & \sum_{m=1}^{81} w_{f,m} \eta_{f,m} b_{c,9} \left(\vec{\Omega}_{f,m} \right) \\ \sum_{m=1}^{81} w_{f,m} \xi_{f,m} b_{c,1} \left(\vec{\Omega}_{f,m} \right) & \cdots & \sum_{m=1}^{81} w_{f,m} \xi_{f,m} b_{c,9} \left(\vec{\Omega}_{f,m} \right) \\ \sum_{m=1}^{81} w_{f,m} \mu_{f,m} \eta_m^f b_{c,1} \left(\vec{\Omega}_{f,m} \right) & \cdots & \sum_{m=1}^{81} w_{f,m} \mu_{f,m} \eta_{f,m} b_{c,9} \left(\vec{\Omega}_{f,m} \right) \\ \sum_{m=1}^{81} w_{f,m} \mu_{f,m} \xi_m^f b_{c,1} \left(\vec{\Omega}_{f,m} \right) & \cdots & \sum_{m=1}^{81} w_{f,m} \mu_{f,m} \xi_{f,m} b_{c,9} \left(\vec{\Omega}_{f,m} \right) \\ \sum_{m=1}^{81} w_{f,m} \eta_{f,m} \xi_m^f b_{c,1} \left(\vec{\Omega}_{f,m} \right) & \cdots & \sum_{m=1}^{81} w_{f,m} \eta_{f,m} \xi_{f,m} b_{c,9} \left(\vec{\Omega}_{f,m} \right) \\ \sum_{m=1}^{81} w_{f,m} \xi_{f,m}^2 b_{c,1} \left(\vec{\Omega}_{f,m} \right) & \cdots & \sum_{m=1}^{81} w_{f,m} \xi_{f,m}^2 b_{c,9} \left(\vec{\Omega}_{f,m} \right) \\ \sum_{m=1}^{81} w_{f,m} \left(\mu_{f,m}^2 - \eta_{f,m}^2 \right) b_{c,1} \left(\vec{\Omega}_{f,m} \right) & \cdots & \sum_{m=1}^{81} w_{f,m} \left(\mu_{f,m}^2 - \eta_{f,m}^2 \right) b_{c,9} \left(\vec{\Omega}_{f,m} \right) \end{bmatrix} \tag{5.7}$$

$$\begin{bmatrix} \tilde{\Psi}_{c,1} \\ \tilde{\Psi}_{c,2} \\ \tilde{\Psi}_{c,3} \\ \tilde{\Psi}_{c,4} \\ \tilde{\Psi}_{c,5} \\ \tilde{\Psi}_{c,6} \\ \tilde{\Psi}_{c,7} \\ \tilde{\Psi}_{c,8} \\ \tilde{\Psi}_{c,9} \end{bmatrix} = \begin{bmatrix} \sum_{m=1}^{9} w_{c,m} \Psi_{c,m} \\ \sum_{m=1}^{9} w_{c,m} \mu_{c,m} \Psi_{c,m} \\ \sum_{m=1}^{9} w_{c,m} \eta_{c,m} \Psi_{c,m} \\ \sum_{m=1}^{9} w_{c,m} \xi_{c,m} \Psi_{c,m} \\ \sum_{m=1}^{9} w_{c,m} \mu_{c,m} \eta_{c,m} \Psi_{c,m} \\ \sum_{m=1}^{9} w_{c,m} \mu_{c,m} \xi_{c,m} \Psi_{c,m} \\ \sum_{m=1}^{9} w_{c,m} \eta_{c,m} \xi_{c,m} \Psi_{c,m} \\ \sum_{m=1}^{9} w_{c,m} \xi_{c,m}^2 \Psi_{c,m} \\ \sum_{m=1}^{9} w_{c,m} \left(\mu_{c,m}^2 - \eta_{c,m}^2 \right) \Psi_{c,m} \end{bmatrix} .$$

Eqn. 5.7 is solved for $\tilde{\Psi}_{c,n}, n = 1:9$, which are inserted back into Eqn. 5.6 to obtain the mapped solution $\Psi_{f,m}, m = 1:81$.

5.2 Fix-Up Algorithm Derivation

The mapping algorithms presented in Section 5.1 are nearly "optimal" when mapping sufficiently smooth solutions away from octant boundaries (small pointwise errors are introduced into the mapped solution even when the incoming solution lives in the underlying DFEM basis space, due to the preservation of the higher angular moments). However, over- and under-shoots (including negativities) may occur when mapping near solution discontinuities or octant boundaries. If the mapped solution does not satisfy a set of prescribed limits (in this research we use either the analytical or empirical limits; Section 7 suggests alternative methods):

$$\Psi_{\min} \leq \Psi_{\text{map},j} \leq \Psi_{\max} \quad , \quad j = 1 : N_{\text{map}} \ , \tag{5.8}$$

then we apply a fix-up algorithm which recasts the mapping problem as a multi-objective optimization problem (MOOP). MOOP minimizes the total difference between a set of objective functions and their associated goals, while ensuring that the solution satisfies a set of constraints.[16] The fix-up algorithm ensures the mapped solution satisfies the prescribed limits, and preserves the 0th angular moment to machine precision, while preserving the higher angular moments of interest as well as possible.

For LDFE-SQ fix-up, the objective functions $Z_i, i = 1 : 3$ are the 1st angular moments of the mapped solution:

$$Z_1 = \sum_{j=1}^{N_{\text{map}}} \Psi_{\text{map},j} \mu_{\text{map},j} w_{\text{map},j} \ , \tag{5.9}$$

$$Z_2 = \sum_{j=1}^{N_{\text{map}}} \Psi_{\text{map},j} \eta_{\text{map},j} w_{\text{map},j} \ , \tag{5.10}$$

and

$$Z_3 = \sum_{j=1}^{N_{\text{map}}} \Psi_{\text{map},j} \xi_{\text{map},j} w_{\text{map},j} \ . \tag{5.11}$$

Their associated goals $G_i, i = 1:3$ are the 1st angular moments of the incoming solution:

$$G_1 = \sum_{k=1}^{N_{\text{inc}}} \Psi_{\text{inc},k} \mu_{\text{inc},k} w_{\text{inc},k} \ , \tag{5.12}$$

$$G_2 = \sum_{k=1}^{N_{\text{inc}}} \Psi_{\text{inc},k} \eta_{\text{inc},k} w_{\text{inc},k} \ , \tag{5.13}$$

and

$$G_3 = \sum_{k=1}^{N_{\text{inc}}} \Psi_{\text{inc},k} \xi_{\text{inc},k} w_{\text{inc},k} \ . \tag{5.14}$$

For QDFE-SQ fix-up, the first three objective functions $Z_i, i = 1:3$ are the same as Eqns. 5.9 to 5.11. The remaining objective functions $Z_i, i = 4:8$ are the 2nd angular moments of the mapped solution:

$$Z_4 = \sum_{j=1}^{N_{\text{map}}} \Psi_{\text{map},j} \mu_{\text{map},j} \eta_{\text{map},j} w_{\text{map},j} \ , \tag{5.15}$$

$$Z_5 = \sum_{j=1}^{N_{\text{map}}} \Psi_{\text{map},j} \mu_{\text{map},j} \xi_{\text{map},j} w_{\text{map},j} \ , \tag{5.16}$$

$$Z_6 = \sum_{j=1}^{N_{\text{map}}} \Psi_{\text{map},j} \eta_{\text{map},j} \xi_{\text{map},j} w_{\text{map},j} \ , \tag{5.17}$$

$$Z_7 = \sum_{j=1}^{N_{\text{map}}} \Psi_{\text{map},j} \xi^2_{\text{map},j} w_{\text{map},j} \ , \tag{5.18}$$

and

$$Z_8 = \sum_{j=1}^{N_{\text{map}}} \Psi_{\text{map},j} \left(\mu^2_{\text{map},j} - \eta^2_{\text{map},j} \right) w_{\text{map},j} \ . \tag{5.19}$$

We note that Eqn. 5.19 preserves $\mu^2-\eta^2$ rather than μ^2, η^2 or each individually. This can be understood by considering the relationship between the directional cosines provided in Eqn. 3.4: $\mu^2+\eta^2+\xi^2=1$, which suggests satisfying Eqn. 5.18 also preserves $1-\mu^2-\eta^2$. SHs must be independent functions, and thus $\mu^2-\eta^2$ is used.

The first three goals $G_i, i=1:3$ are the same as Eqns. 5.12 to 5.14. The remaining goals $G_i, i=4:8$ are the 2nd angular moments of the incoming solution:

$$G_4=\sum_{k=1}^{N_{\text{inc}}}\Psi_{\text{inc},k}\mu_{\text{inc},k}\eta_{\text{inc},k}w_{\text{inc},k}\ , \tag{5.20}$$

$$G_5=\sum_{k=1}^{N_{\text{inc}}}\Psi_{\text{inc},k}\mu_{\text{inc},k}\xi_{\text{inc},k}w_{\text{inc},k}\ , \tag{5.21}$$

$$G_6=\sum_{k=1}^{N_{\text{inc}}}\Psi_{\text{inc},k}\eta_{\text{inc},k}\xi_{\text{inc},k}w_{\text{inc},k}\ , \tag{5.22}$$

$$G_7=\sum_{k=1}^{N_{\text{inc}}}\Psi_{\text{inc},k}\xi_{\text{inc},k}^2w_{\text{inc},k}\ , \tag{5.23}$$

and

$$G_8=\sum_{k=1}^{N_{\text{inc}}}\Psi_{\text{inc},k}\left(\mu_{\text{inc},k}^2-\eta_{\text{inc},k}^2\right)w_{\text{inc},k}\ . \tag{5.24}$$

The following equality constraint preserves the 0th angular moment from the incoming solution:

$$\sum_{j=1}^{N_{\text{map}}}\Psi_{\text{map},j}w_{\text{map},j}=\sum_{k=1}^{N_{\text{inc}}}\Psi_{\text{inc},k}w_{\text{inc},k}\ . \tag{5.25}$$

Additional inequality constraints are set to ensure the prescribed limits in Eqn. 5.8 are satisfied.

The goal programming (GP) method combines the objectives and goals of the MOOP into a single-objective optimization problem (SOOP), which can be solved using any standard linear program (LP), e.g., Simplex or Interior Point methods.[16,

17, 18, 19] We chose to use the simplest version of the Simplex method (i.e., the revised Simplex method)[17] as a proof-of-concept due to its robustness and simplicity in implementation. As discussed in Section 7, future work should investigate the use of other LPs to optimize the speed of the fix-up algorithm. Appendix B discusses the GP method, derives the standard form of the SOOP required for LPs, and provides the revised Simplex method pseudocode for the fix-up algorithm.

5.3 Adaptive Strategies

This research provides the necessary tools to effectively use DFEM-based angular quadratures within an adaptive S_n algorithm. The new DFEM-based angular quadratures, along with the new mapping and fix-up algorithms, can be directly used within the adaptive S_n algorithm presented by Jarrell and Adams. [2] Its effective implementation in parallel S_n codes is left for future work. We present a simplified adaptive S_n algorithm, which only considers local refinement (i.e., ignores coarsening). This simplified adaptive S_n algorithm will be used to generate locally-refined angular quadratures for testing the new mapping and fix-up algorithms in Section 6.

In adaptive S_n algorithms, the spatial domain is decomposed into quadrature regions, which are allowed to have differently-refined DFEM-based angular quadratures. The new mapping and fix-up algorithms are used to pass the angular flux solution between quadrature regions. After every user-specified number of source iterations, the angular flux solution is tested at each quadrature region boundary to determine if any angular regions (i.e., SQs) need to be refined (i.e., replaced with its daughter sub-squares as defined in Section 4.1.6).

To determine if a SQ needs to be refined, we first apply the new mapping algorithm to obtain the mapped angular flux solution for its daughter SQs $\Psi_{\text{map,j}}, j = 1 : N_{\text{daughters}}$. Next, we sweep across the quadrature region using the latest itera-

tion's boundary conditions and scattering source, to obtain the swept angular flux solution for the same daughter SQs $\Psi_{\text{swept,j}}, j = 1 : N_{\text{daughters}}$. Lastly, we calculate the difference between the mapped and swept angular flux solutions:

$$\Delta\Psi_j = |\Psi_{\text{map,j}} - \Psi_{\text{swept,j}}| \quad , \quad j = 1 : N_{\text{daughters}} \ . \tag{5.26}$$

If any $\Delta\Psi_j$ exceeds both of the following limits at any quadrature region boundary, then we refine the SQ containing quadrature direction j:

$$\Delta\Psi_j > \epsilon_{pw}\Psi_{\text{swept,j}} \ , \tag{5.27}$$

and

$$\Delta\Psi_j > \epsilon_{oc}\frac{j_{\text{octant}}}{\left(\vec{\Omega}_j \cdot \vec{n}\right)} \ , \tag{5.28}$$

where ϵ_{pw} is the pointwise error tolerance, ϵ_{oc} is the octantwise error tolerance, and j_{octant} is the octant current defined as

$$j_{\text{octant}} = \frac{\sum_{m=1}^{M} w_m \left(\vec{\Omega}_m \cdot \vec{n}\right) \Psi_m}{\sum_{m=1}^{M} w_m} \ , \tag{5.29}$$

where m is the index of the directions in the same octant as direction j. Eqn. 5.28 is imposed to prevent the over-refinement of SQs with angular flux solution near zero.

6. RESULTS

In this section, we present computational results using the new LDFE-SQ and QDFE-SQ angular quadratures, and the new mapping and fix-up algorithms. We also test the LDFE-ST, Level Symmetric (LS), triangular Gauss-Chebyshev (GC), and triangular Quadruple Range (QR) angular quadratures. We note that only triangular (not rectangular) GC and QR angular quadratures were tested since previous testing [2, 3] showed similar results for triangular and rectangular GC angular quadratures, and higher performance for triangular over rectangular QR angular quadratures for radiation transport problems similar to the ones performed in this research.

6.1 Angular Quadrature Performance

We demonstrate the ability of the LDFE-SQ and QDFE-SQ angular quadratures to: (1) accurately integrate increasing-degree spherical harmonics (SH) functions; (2) accurately form the scalar flux for both simple and complex radiation transport problems, while producing particle-conservation errors that are small compared to other discretization errors for radiation transport problems with anisotropic scattering; (3) decrease local integration errors compared to the previous DFEM-based angular quadratures; and (4) increase computational efficiency for certain radiation transport problems by using local refinement. The radiation transport problems were performed using PDT,[20, 21] a massively parallel discrete-ordinates (S_n) transport code developed at Texas A&M University using the STAPL library.[22, 23]

6.1.1 Spherical Harmonics Integration

As discussed in Section 2.3.2, angular quadratures must accurately integrate SH functions of increasing degree in order to avoid particle-conservation errors, and

to accurately form angular flux moments. The LDFE-SQ and QDFE-SQ angular quadratures were tested to integrate up to 24th-degree SH functions. Due to the octant rotational symmetry of the LDFE-SQ and QDFE-SQ angular quadratures, integrations were only performed over the first octant. The computational results show LDFE-SQ and QDFE-SQ angular quadratures exactly integrate up to 1st and 2nd-degree SH functions, respectively. The LDFE-SQ and QDFE-SQ angular quadratures both integrate all higher-degree SH functions tested with 4th-order accuracy as a function of angular mesh length, defined as

$$h = \frac{1}{\sqrt{\text{number of directions}}} \, . \tag{6.1}$$

That is, decreasing h by a factor of n reduces the integration error by n^4. The reference solutions were obtained analytically. Figs. 6.1 to 6.3 plot integration error as a function of h for selected SH functions ($\mu\eta$, $\mu^3\eta\xi$ and $\xi^3\mu^6\xi^{15}$). We have tested many other polynomials, and all results are similar to those shown. The LDFE-SQ and QDFE-SQ angular quadratures were tested up to 161,376 and 146,016 directions over all octants, respectively. We note that one might expect the LDFE-based and QDFE-based angular quadratures would exhibit 2nd-order and 3rd-order integration accuracies, respectively. We do not have a theoretical explanation for the observed higher accuracy, which is also seen with the LDFE-ST angular quadratures.

6.1.2 One-Cell Problem

The one-cell problem demonstrates the ability of the LDFE-SQ and QDFE-SQ angular quadratures to accurately form the scalar flux for a simple radiation transport problem. The one-cell problem is a cube with 1.0 cm sides made of pure-absorber material ($\Sigma_a = 1.0 \text{ cm}^{-1}$) containing uniformly-distributed isotropic source ($q = 1.0$ neutron/cm^{3}s $\cdot$ ster) surrounded by vacuum. The piecewise linear discontinuous

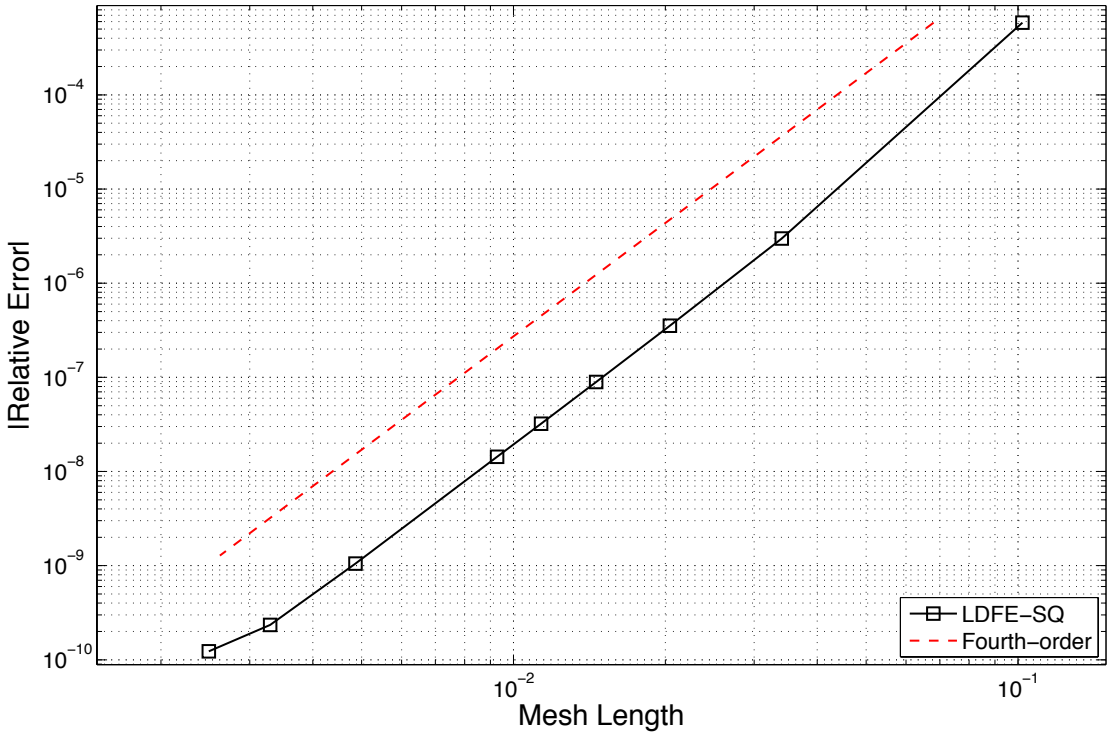

Figure 6.1: Integration error for $\mu\eta$ over the first octant using LDFE-SQ. Integration error for $\mu\eta$ using QDFE-SQ is exact to machine precision.

finite-element method (PWLD) is used for spatial discretization.[24] The one-cell problem was performed using PDT. Fig. 6.4 plots scalar flux error as a function of h. The reference solution was generated using the finest LDFE-ST angular quadrature available containing 524,288 directions over all octants. The computational results show the LDFE-SQ and QDFE-SQ angular quadratures form the scalar flux with 4th-order accuracy as a function of h - significantly better than LS at 1.5-order, triangular GC at 2nd-order, and on-par with triangular QR and LDFE-ST angular quadratures also at 4th-order. The LDFE-SQ and QDFE-SQ angular quadratures were tested up to 161,376 and 146,016 directions over all octants, respectively.

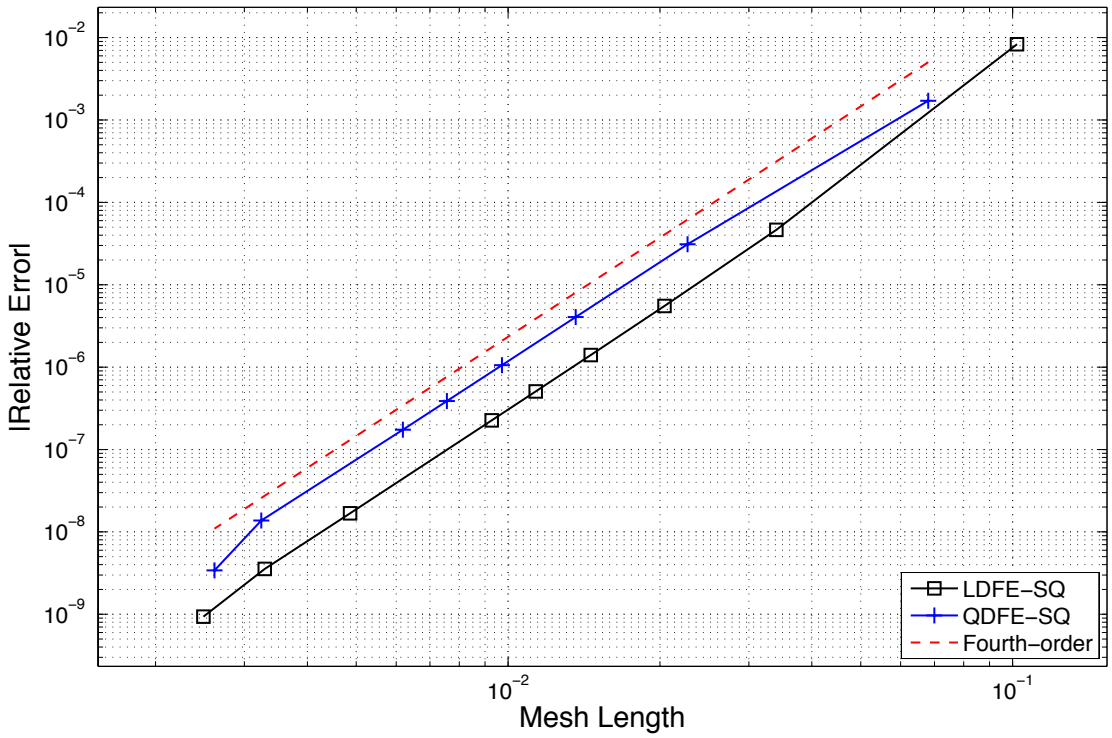

Figure 6.2: Integration error for $\mu^3\eta\xi$ over the first octant using LDFE-SQ and QDFE-SQ.

6.1.3 Pin-Cell Problem

The pin-cell problem provides a qualitative measure of local integration error for the traditional and DFEM-based angular quadratures. As discussed in Section 2.3.2, ray effects (i.e., artificial peaks in the scalar flux spatial distribution) are caused by the inability of angular quadratures to accurately integrate the angular flux solution over local angular regions. A desirable angular quadrature should minimize the magnitude and wavelength of ray effects. The pin-cell problem is a two-dimensional pin with 0.5 cm radius made of pure-absorber material ($\Sigma_a = 1.0$ cm^{-1}) containing uniformly-distributed isotropic source ($q = 1.0$ neutron/cm^{3}s $\cdot$ ster) surrounded by vacuum. The PWLD method is used for spatial discretization. The pin-cell problem

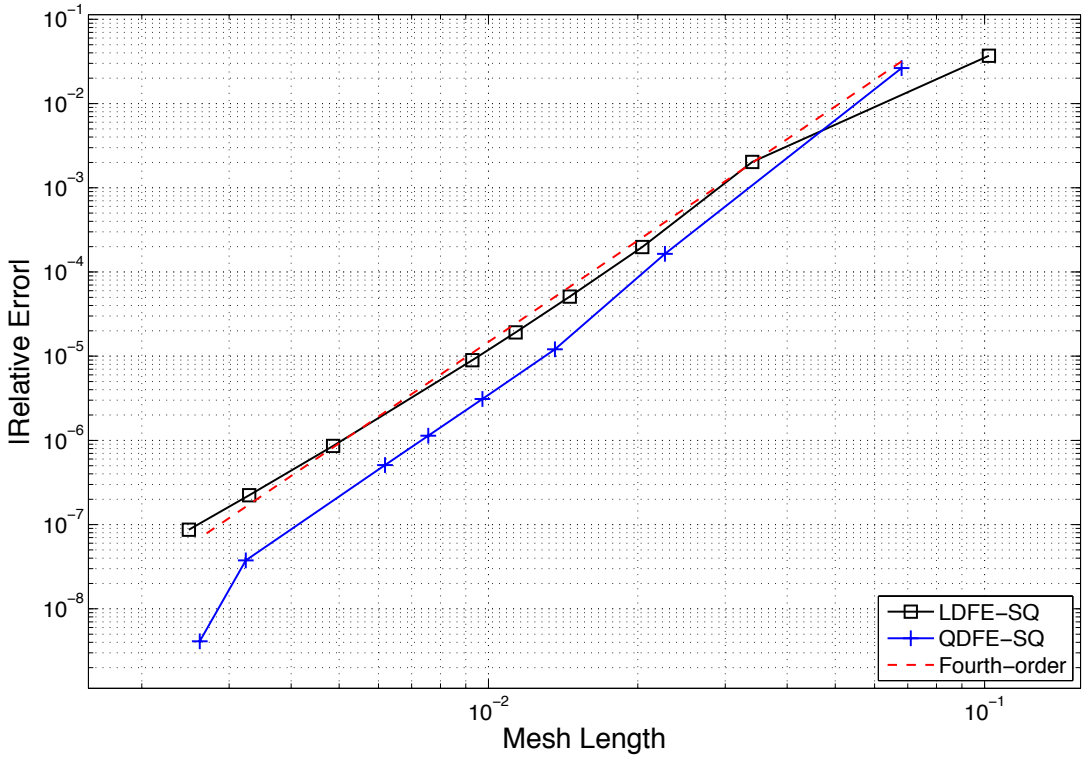

Figure 6.3: Integration error for $\mu^3\eta^6\xi^{15}$ over the first octant using LDFE-SQ and QDFE-SQ.

was performed using PDT. The spatial mesh used for this problem is shown in Fig. 6.5.

Fig. 6.6 plots scalar flux contours moving away from the pin using LS, triangular GC, triangular QR, LDFE-ST, LDFE-SQ and QDFE-SQ angular quadratures with $\approx$ 100 directions. Analytically, the scalar flux should produce perfectly circular contours of decreasing magnitude moving away from the pin. However, the computational results show significant ray effects for all angular quadratures at such low angle counts. The S_{24} (78-point per octant) LS angular quadrature (greatest number of directions with strictly positive weights) produces the most pronounced (i.e., highest peaks and longest wavelengths) ray effects among the quadratures tested here. The

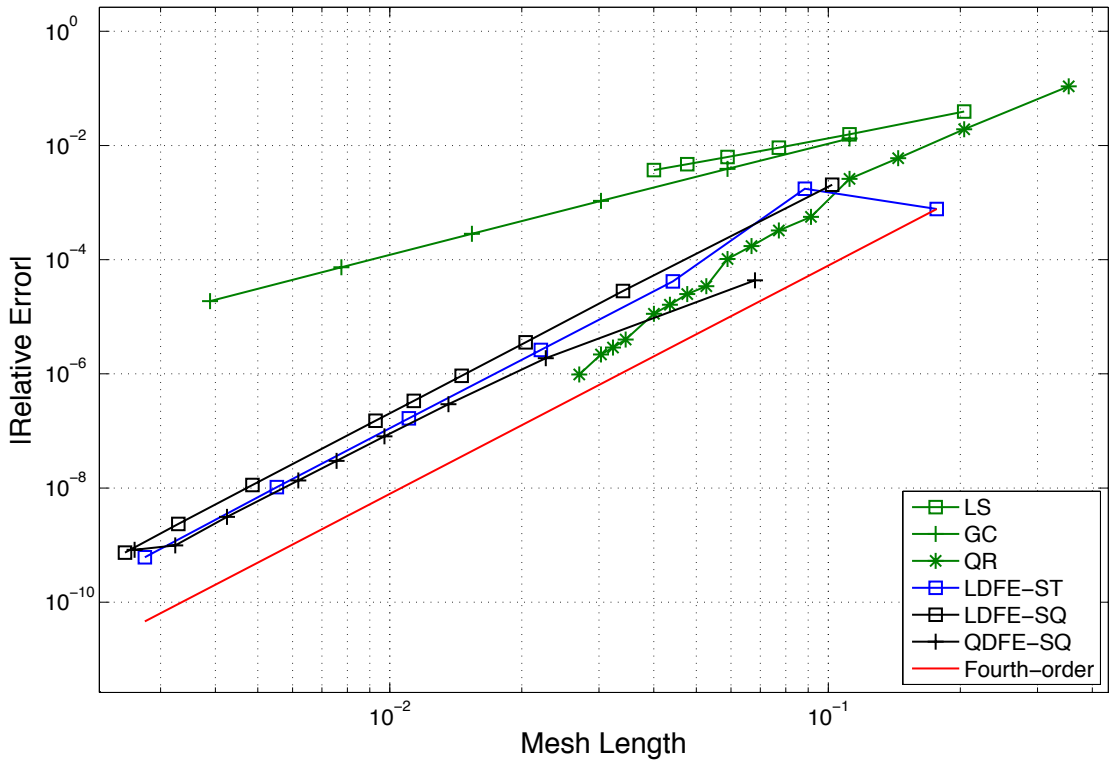

Figure 6.4: Scalar flux error for the one-cell problem using LS, triangular GC, triangular QR, LDFE-ST, LDFE-SQ and QDFE-SQ.

78-point per octant triangular GC and triangular QR angular quadratures produce significantly less pronounced ray effects than LS. The 64-point per octant LDFE-ST angular quadrature produces slightly more pronouned ray effects than triangular GC and triangular QR, which may be partially attributed to having less directions (next available refinement produces 256 directions per octant). The 108-point per octant LDFE-SQ and QDFE-SQ angular quadratures produce less pronounced ray effects than LDFE-ST, which may be partially attributed to having more directions (previous refinement produces only 48 directions per octant). Fig. 6.7 plots scalar flux contours moving away from the pin using triangular GC, LDFE-ST, LDFE-SQ and QDFE-SQ angular quadratures with $\approx$ 1000 directions per octant. The results

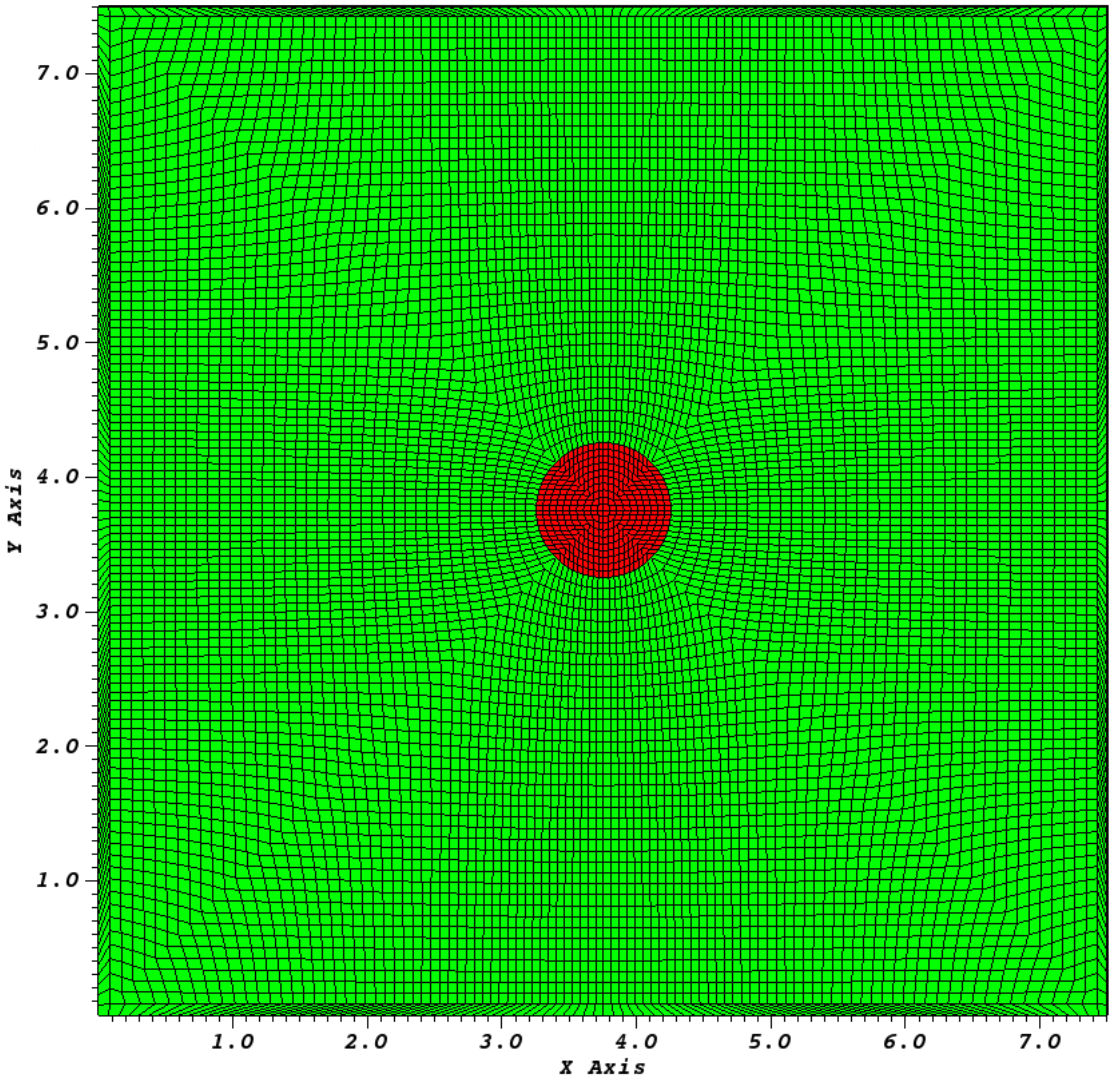

Figure 6.5: Spatial mesh used for the pin-cell problem. Red and green regions indicate source and vacuum materials, respectively.

show ray effects are nearly eliminated for all of these angular quadratures at such high angle counts for the specified distances away from the pin. We note that pronounced ray effects would re-appear using these angular quadratures as we move farther away from the pin.

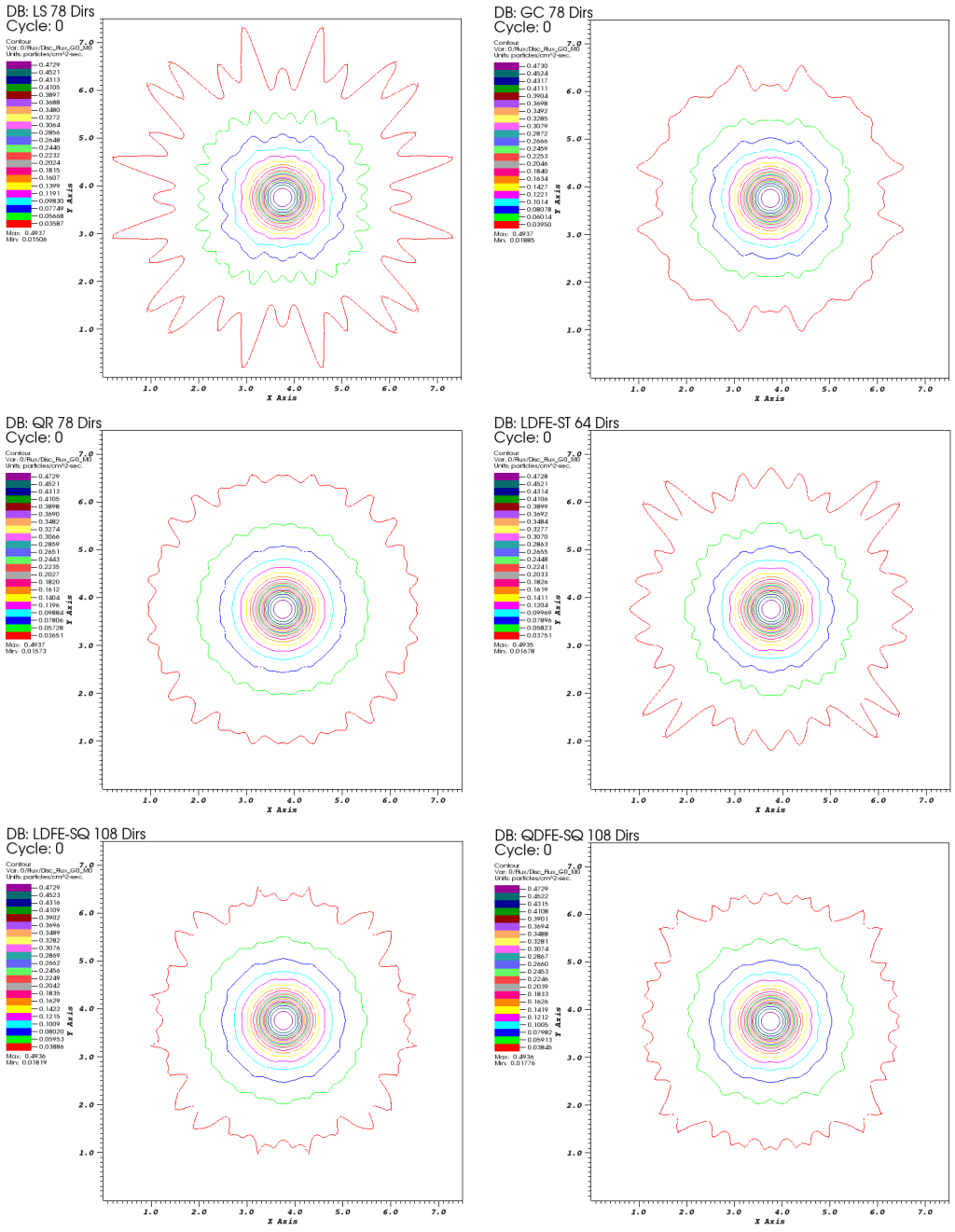

Figure 6.6: Scalar flux contours for the pin-cell problem using LS (top left), triangular GC (top right), triangular QR (middle left), LDFE-ST (middle right), LDFE-SQ (bottom left) and QDFE-SQ (bottom right) with ≈ 100 directions per octant.

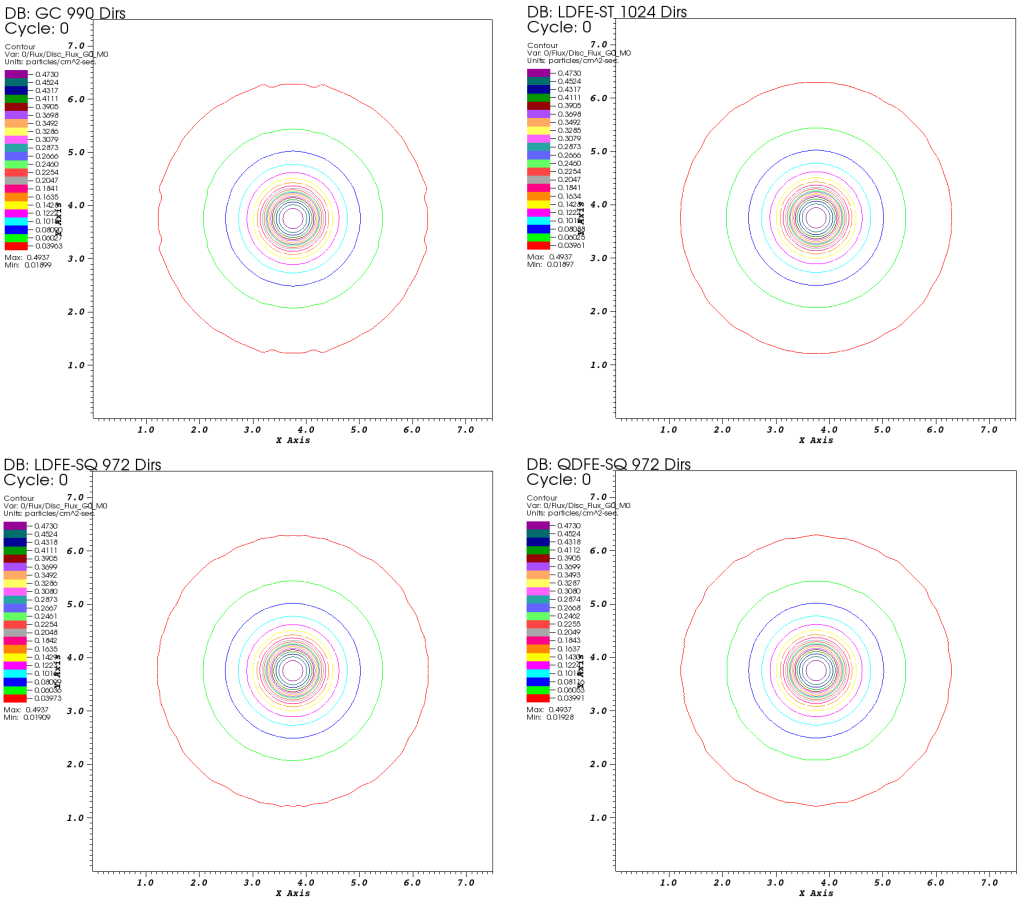

Figure 6.7: Scalar flux contours for the pin-cell problem using triangular GC (top left), LDFE-ST (top right), LDFE-SQ (bottom left) and QDFE-SQ (bottom right) with ≈ 1000 directions per octant.

6.1.4 Spherical Source Problem

The spherical source problem provides a quantitative measure of local integration error for the traditional and DFEM-based angular quadratures. The spherical source problem consists of a spherical source surrounded by vacuum. The spherical source has a radius of 1.0 cm, and is made of a pure-absorber material ($\Sigma_a = 1.0$ cm^{-1}) containing uniformly-distributed isotropic source ($q = 1.0$ neutron/cm^{3}s $\cdot$ ster). The spherical source problem used a ray-tracing method where the scalar flux at a spatial

point $\vec{r}$ outside of the spherical source is defined as

$$\phi\left(\vec{r}\right) = \frac{q}{\Sigma_a} \sum_{m=1}^{M} w_m \left(1 - \exp\left(-\Sigma_a \ell_m\right)\right) \ , \tag{6.2}$$

where M is the total number of quadrature directions, w_m is the weight of quadrature direction m, and ℓ_m is the chord length for direction m starting from spatial point $\vec{r}$ through the spherical source. The quantity of interest (QOI) is the scalar flux at thousands of spatial points distributed across a spherical surface of radius $d = 5.0$ cm concentric with the spherical source. We select the spatial points such that the directions from within the spherical source to each spatial point remains in the first octant. Analytically, the scalar flux should remain constant regardless of position, if d is fixed. However, computational results show the calculated scalar flux changes with position due to angular quadrature local integration error. As discussed in Section 6.1.3, a desirable angular quadrature should minimize the magnitude and wavelength of these scalar flux oscillations, also known as ray effects. The reference solution was generated using the finest LDFE-ST angular quadrature available containing 524,288 directions over all octants.

Fig. 6.8 plots scalar flux error as a function of spatial position using LS, triangular GC, triangular QR, LDFE-ST, and the directional adaptive mesh refinement (DAMR) angular quadrature provided by Brown et al. [12] with ≈70 directions per octant. The 78-point per octant LS angular quadrature (greatest number of directions with strictly positive weights) produces the most prominent ray effects including the most negative error peaking (-6.6E-1) and the highest root-means-square (RMS) error (2.6E-1). The 78-point per octant triangular GC angular quadrature produces much less prominent ray effects than LS as evident by its lower error peaking (-2.7E-1 to 2.7E-1) and RMS error (9.4E-2). The 78-point per octant triangular QR angu-

lar quadrature also produces less prominent ray effects than LS, but has comparable negative error peaking (-5.9E-1). The 64-point per octant LDFE-ST angular quadrature was run using slightly less directions since the next available refinement produces 256 directions per octant. The results show LDFE-ST angular quadrature produces three very large error peaks with the highest positive error peaking (7.1E-1). The location of the peaks center around the hexagonal rings of direction that form as discussed in Section 3.2.2. The 64-point per octant DAMR angular quadrature was run with the same number of directions as LDFE-ST, since the next available refinement also produces 256 directions per octant. The results show the DAMR angular quadratures produce less prominent ray effects than LDFE-ST including lower error peaking (-3.8E-1 to 6.4E-1), and lower RMS error (1.7E-1). Table 6.1 summarizes the above results.

Table 6.1: Summary of the results for the spherical source problem using LS, triangular GC, triangular QR, LDFE-ST, and DAMR with ≈70 directions per octant.

Parameter	LS	GC	QR	LDFE-ST	DAMR
Direction count	78	78	78	64	64
Minimum error	-6.6E-1	-2.7E-1	-5.9E-1	-4.4E-1	-3.8E-1
Maximum error	5.7E-1	2.7E-1	3.8E-1	7.1E-1	6.4E-1
RMS error	2.6E-1	9.4E-2	1.5E-1	2.0E-1	1.7E-1

Fig. 6.9 plots the scalar flux error as a function of detector position using triangular GC, triangular QR, LDFE-SQ and QDFE-SQ with ≈105 directions per octant. Overall, the 105-point per octant triangular QR angular quadrature produces the most prominent ray effects including the most negative (-3.5E-1) and positive (3.1E-1) error peaking, and the highest RMS error (9.7E-2). The 105-point per octant triangular GC angular quadrature produces less prominent ray effects than triangu-

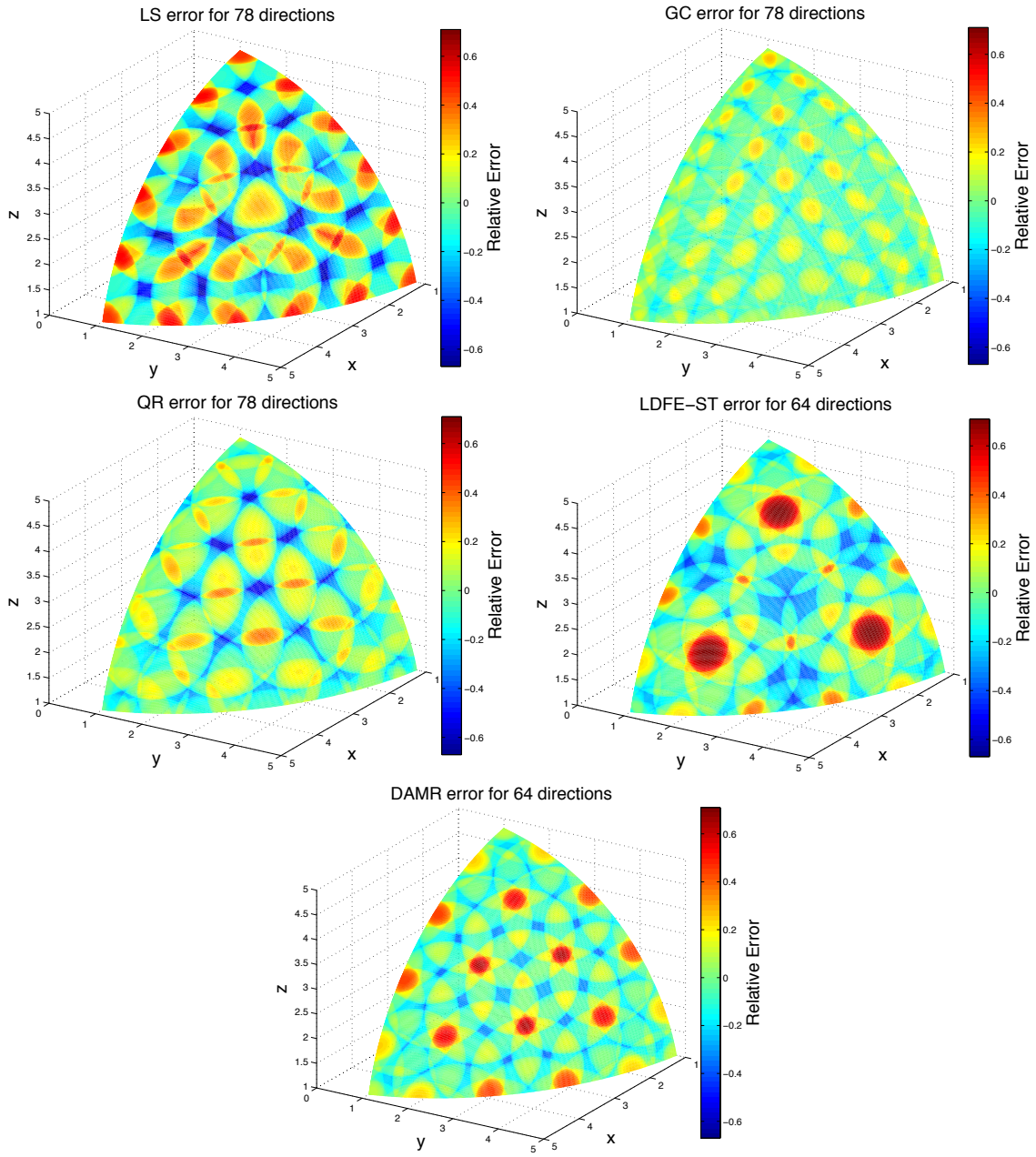

Figure 6.8: Scalar flux error as a function of position for the spherical source problem using LS (top left), triangular GC (top right), triangular QR (center left), LDFE-ST (center right), and DAMR (bottom) with ≈70 directions per octant. Color scales are identical.

lar QR as is evident from its lower error peaking (-2.4E-1 to 2.3E-1) and RMS error (7.2E-2). The 108-point per octant LDFE-SQ and QDFE-SQ angular quadratures produce lower positive error peaking (1.8E-1 and 1.9E-1, respectively) than both triangular GC and triangular QR angular quadratures. The LDFE-SQ and QDFE-SQ angular quadratures produce negative error peaking (-3.5E-1 and -2.5E-1, respectively) that is similar to triangular GC and triangular QR. Table 6.2 summarizes the above results.

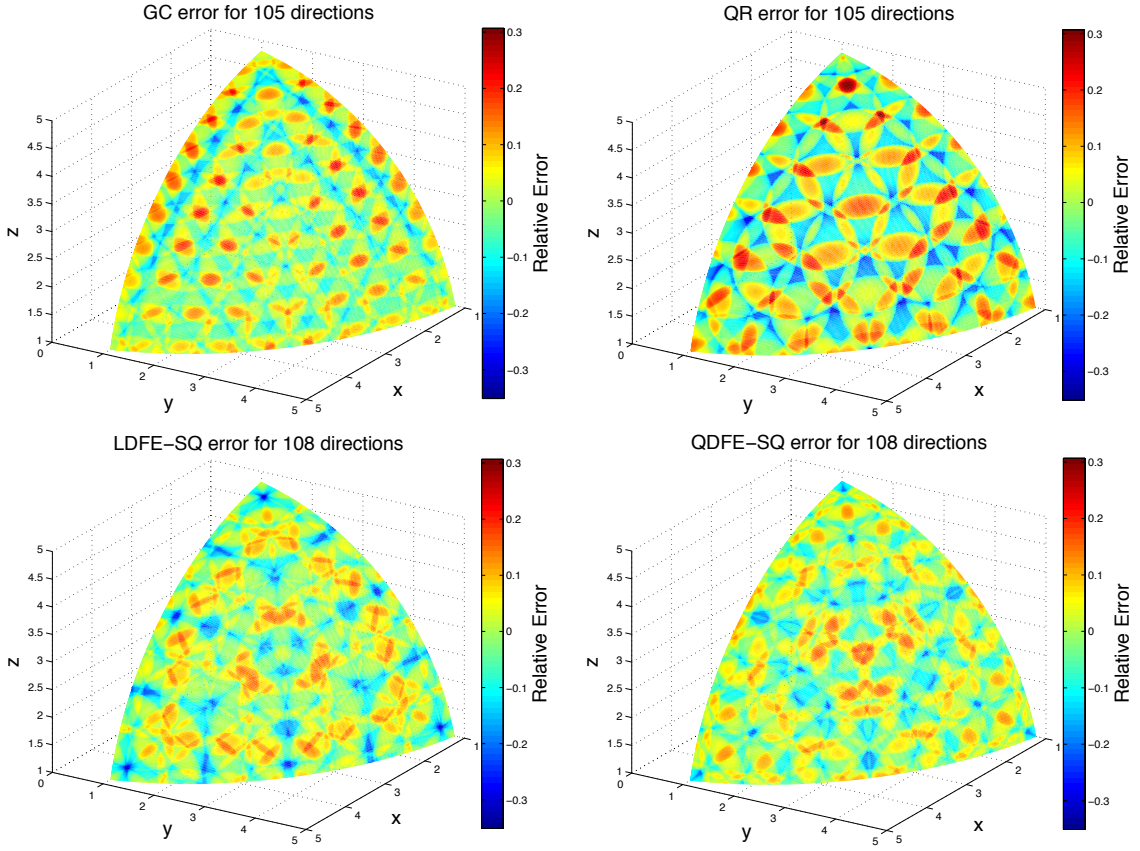

Figure 6.9: Scalar flux error as a function of position for the spherical source problem using triangular GC (top left), triangular QR (top right), LDFE-SQ (bottom left), and QDFE-SQ (bottom right) with ≈105 directions per octant. Color scales are identical.

Table 6.2: Summary of the results for the spherical source problem using triangular GC, triangular QR, LDFE-SQ, and QDFE-SQ with ≈105 directions per octant.

Parameter	GC	QR	LDFE-SQ	QDFE-SQ
Direction count	105	105	108	108
Minimum error	-2.4E-1	-3.5E-1	-3.5E-1	-2.5E-1
Maximum error	2.3E-1	3.1E-1	1.8E-1	1.9E-1
RMS error	7.2E-2	9.7E-2	7.3E-2	6.7E-2

Fig. 6.10 plots the scalar flux error as a function of position using triangular GC, LDFE-ST, LDFE-SQ, QDFE-SQ, and DAMR with ≈1000 directions per octant. The 1024-point per octant LDFE-ST angular quadrature produces the most prominent ray effects including the most negative (-5.3E-2) and positive (6.3E-2) error peaking, and the highest RMS error (1.2E-2). This is true despite the fact that the LDFE-ST angular quadrature has a slightly larger number of directions. The location of the most positive error peaks once again center around the hexagonal rings of directions that form. Table 6.3 summarizes the above results.

Table 6.3: Summary of the results for the spherical source problem using triangular GC, LDFE-ST, LDFE-SQ, QDFE-SQ, and DAMR with ≈1000 directions per octant.

Parameter	GC	LDFE-ST	LDFE-SQ	QDFE-SQ	DAMR
Direction count	990	1024	972	972	1024
Minimum error	-3.6E-2	-5.3E-2	-3.5E-2	-3.7E-2	-3.8E-2
Maximum error	2.8E-2	6.3E-2	3.8E-2	3.5E-2	4.5E-2
RMS error	8.0E-3	1.2E-2	1.0E-2	9.7E-3	1.1E-2

Fig. 6.11 plots the RMS error as a function of angular mesh length. The results show the RMS error reduces by 2nd-order as a function of h for all angular quadratures except LS.

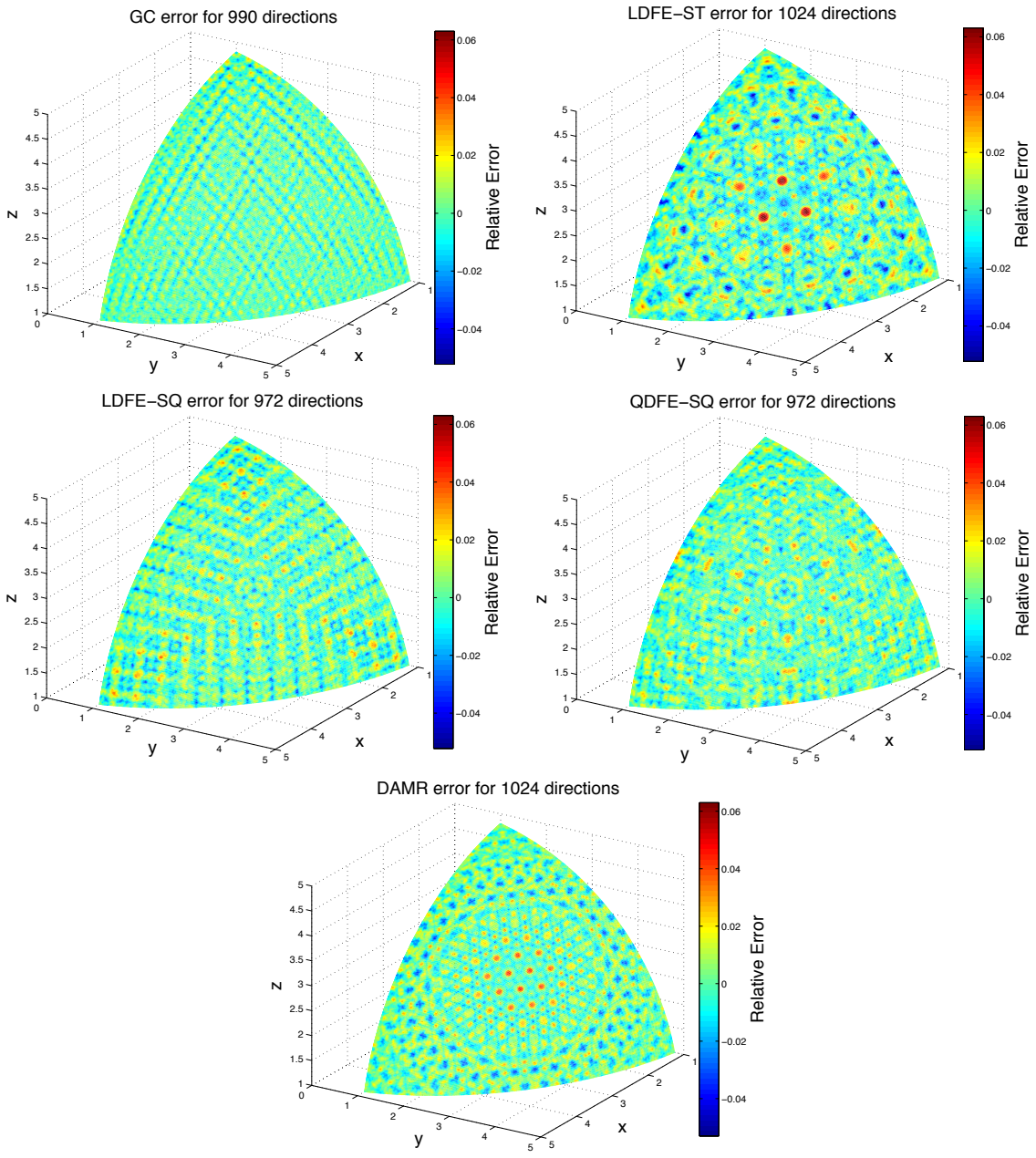

Figure 6.10: Scalar flux error as a function of position for the spherical source problem using triangular GC (top left), LDFE-ST (top right), LDFE-SQ (center left), QDFE-SQ (center right), and DAMR (bottom) with ≈1000 directions per octant. Color scales are indentical.

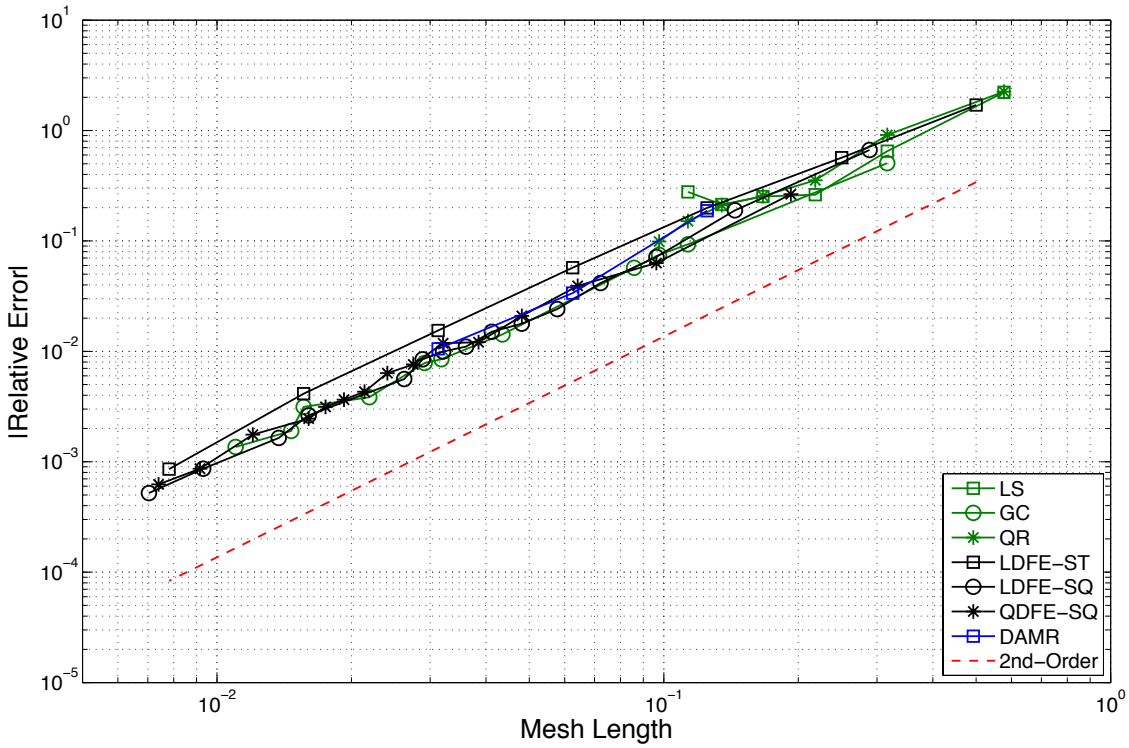

Figure 6.11: RMS error as a function of angular mesh length h for LS, triangular GC, triangular QR, LDFE-ST, LDFE-SQ, QDFE-SQ and DAMR.

6.1.5 Kobayashi Problem

The Kobayashi problem [25] demonstrates the ability of the LDFE-SQ and QDFE-SQ angular quadratures to accurately form the scalar flux for a complex radiation transport problem. The particular Kobayashi problem is a rectangular block made of pure-absorber material ($\Sigma_{a,1} = 1.0$ cm^{-1}) containing a duct ($\Sigma_{a,2} = 10^{-4}$ cm^{-1}) with sharp, discontinuous bends as shown in Fig. 6.12. The void duct inlet contains a uniformly-distributed isotropic source ($q = 1.0$ neutron/cm^{3}s $\cdot$ ster and $\Sigma_{a,3} = 1.0$ cm^{-1}). The Kobayashi problem used a ray-tracing method where the scalar flux

at a spatial point $\vec{r}$ outside of the source is defined as

$$\phi\left(\vec{r}\right) = \frac{q}{\Sigma_{a,3}} \sum_{m=1}^{M} w_m \exp\left(-\Sigma_{a,1}\ell_{m,1} - \Sigma_{a,2}\ell_{m,2}\right)\left(1 - \exp\left(-\Sigma_{a,3}\ell_{m,3}\right)\right) \ , \tag{6.3}$$

where M is the total number of quadrature directions, w_m is the weight of quadrature direction m, $\ell_{m,1}$ is the path length along direction m starting from spatial point $\vec{r}$ through the rectangular block made of pure-absorber material, $\ell_{m,2}$ is the path length along direction m starting from spatial point $\vec{r}$ through the duct, and $\ell_{m,3}$ is the path length along direction m starting from spatial point $\vec{r}$ through the source at the duct inlet. The QOI is the scalar flux near the duct outlet, specifically at (35 cm, 95 cm, 35 cm). The LDFE-SQ and QDFE-SQ angular quadratures were tested up to 161,376 and 146,016 directions over all octants, respectively. The published reference solution [25] was used to calculate the scalar flux errors.

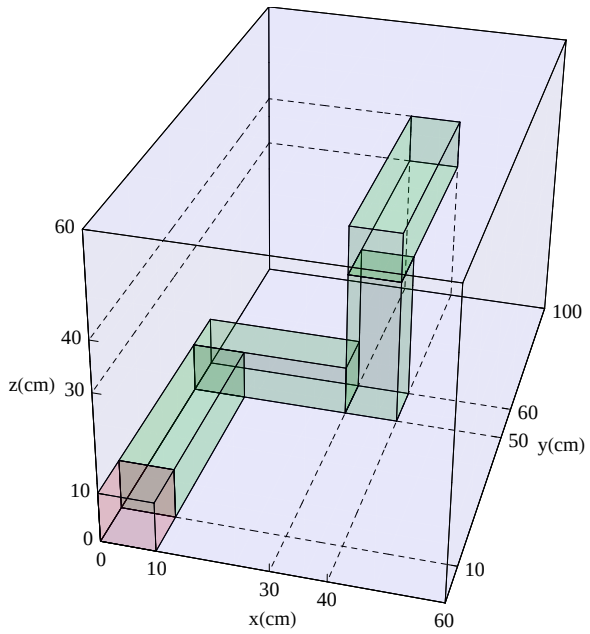

Figure 6.12: Problem setup for Kobayashi problem with pure-absorber shielding (blue), uniformly-distributed isotropic source (red) and duct (green).

We note that other versions of the Kobayashi benchmark problem include scattering. In this research, we chose the pure-absorber version because the addition of scattering tends to smooth the angular variation of the angular flux, thereby making it easier for angular quadratures to integrate. Other pure-absorber problems could have been chosen for this study, and we recognize the duct does not play a large role in the solution when there is no scattering. We chose the Kobayashi benchmark problem because it is well-known, and has a well-vetted published reference solution.

6.1.5.1 Uniform Refinement

Fig. 6.13 plots scalar flux error as a function of h, which shows the order of convergence has decreased for all DFEM angular quadratures compared to the simple one-cell problem from Section 6.1.4. The computational results show LS angular quadrature produces scalar flux error that oscillates with refinement, and remains above 100% until S_{24} (greatest number of directions with strictly positive weights). The remaining angular quadratures (i.e., triangular GC, triangular QR, LDFE-ST, LDFE-SQ and QDFE-SQ) all produce scalar flux errors that decrease by ≈2nd-order.

6.1.5.2 Local Refinement

As discussed in Section 3.3, LDFE-SQ and QDFE-SQ angular quadratures support local refinement by recursively refining only the angular regions requiring additional resolution. For the Kobayashi benchmark problem, only the angular regions within the cone-of-angle between the source at the duct inlet and the spatial point of interest at the duct outlet (35 cm, 95 cm, 35 cm) contribute to the QOI. We can reduce memory and run-time requirements without losing accuracy by refining only the angular regions within the cone-of-angle. Fig. 6.14 illustrates the local refinement process beginning with a uniformly-refined LDFE-SQ angular quadrature followed by several local refinement steps, which recursively refine the angular regions contained

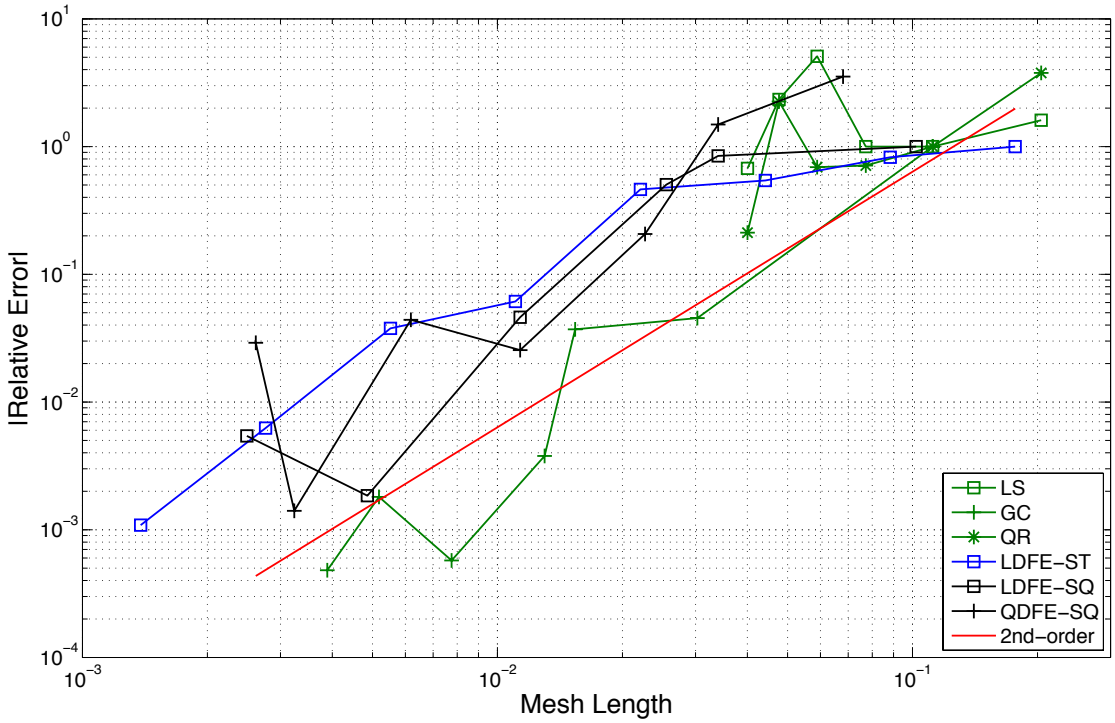

Figure 6.13: Scalar flux error at the duct outlet (35 cm, 95 cm, 35 cm) for the Kobayashi problem using uniform LS, triangular GC, triangular QR, LDFE-ST, LDFE-SQ and QDFE-SQ.

within the cone-of-angle. Fig. 6.15 plots scalar flux error as a function of h using locally-refined LDFE-SQ angular quadrature, which shows the order of convergence increases from ≈2nd-order using uniform refinement to ≈4th-order using local refinement. The difference in scalar flux error between the uniform and locally-refined LDFE-SQ angular quadratures increases with refinement. For example, the uniform LDFE-SQ angular quadrature with h ≈2E-2 produces a relative error of ≈2E-1, whereas the locally-refined LDFE-SQ angular quadrature with approximately the same h produces a relative error of ≈2E-3.

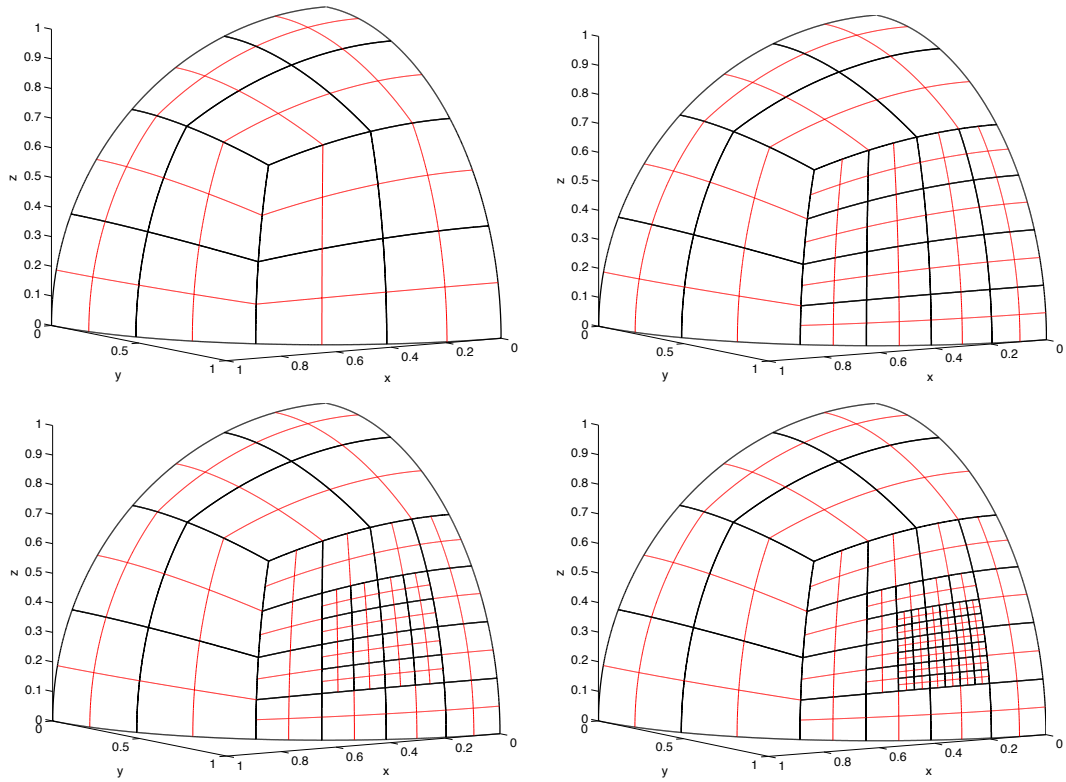

Figure 6.14: LDFE-SQ sub-square (black lines) and sub-sub-square (red lines) divisions after three local refinements for the Kobayashi problem. Top left figure shows the initial uniform LDFE-SQ angular quadrature.

6.1.5.3 Artificial Angular Smoothing

In this subsection, we demonstrate the concept of artificial angular smoothing caused by poor spatial discretization (i.e., false scattering or numerical diffusion).[26, 27] We re-ran the Kobayashi problem using uniform angular quadratures with PWLD spatial discretization in PDT. Figs. 6.16 and 6.17 plot scalar flux error as a function of h using 1.0 cm and 0.5 cm spatial mesh lengths, respectively. The reference solutions were obtained using the triangular GC angular quadrature with 263,168 directions over all octants. The reference solutions represent the angularly resolved solution for the given spatial discretization including its artificial angular smoothing.

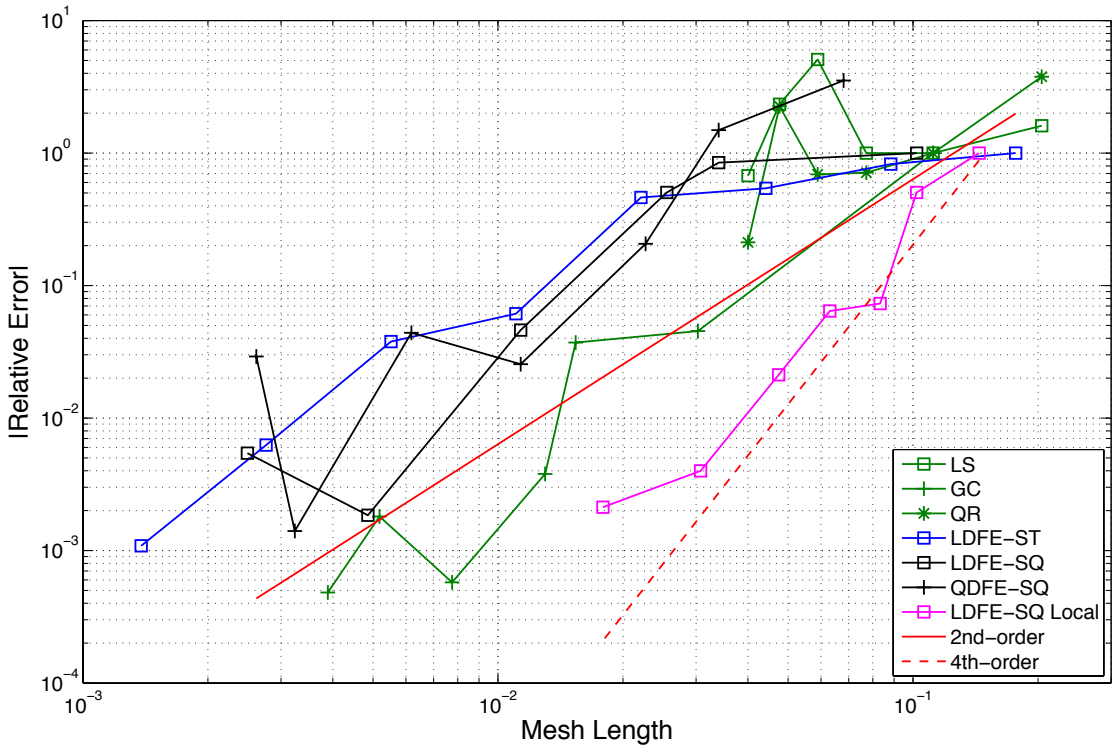

Figure 6.15: Scalar flux error at the duct outlet (35 cm, 95 cm, 35 cm) for the Kobayashi problem using locally-refined LDFE-SQ.

The computational results show LS angular quadrature continues to produce scalar flux error that oscillates with refinement, and remains above 100% until S_{24}. The remaining angular quadratures produce scalar flux errors that also continue to decrease by ≈2nd-order at intermediate refinement. However, at high refinement, triangular GC, LDFE-ST, LDFE-SQ and QDFE-SQ angular quadratures produce scalar flux errors that rapidly decrease due to artificial angular smoothing of the angular flux caused by poor spatial discretization. The degree of angular smoothing increases with larger spatial mesh lengths, producing angular flux that are easier for angular quadratures to integrate. This is evident by comparing Figs. 6.16 and 6.17 showing significant decrease in the magnitude of the change in scalar flux errors (from 12 to 7 decades) as we decrease spatial mesh length from 1.0 cm to 0.5 cm. For example, the

scalar flux error using S_{128} GC angular quadrature with 1.0 cm spatial mesh length is ≈1.0E-7 whereas the scalar flux error using the same angular quadrature with 0.5 cm spatial mesh length is ≈1.0E-4. The performance gap between triangular GC and the DFEM-based angular quadratures should further decrease with increasing spatial resolution, since triangular GC relies on having smooth angular flux solution for accuracy. The scalar flux error plot with increasing spatial resolution should approach the semi-analytic solution provided in Fig. 6.13, which contains no spatial discretization error.

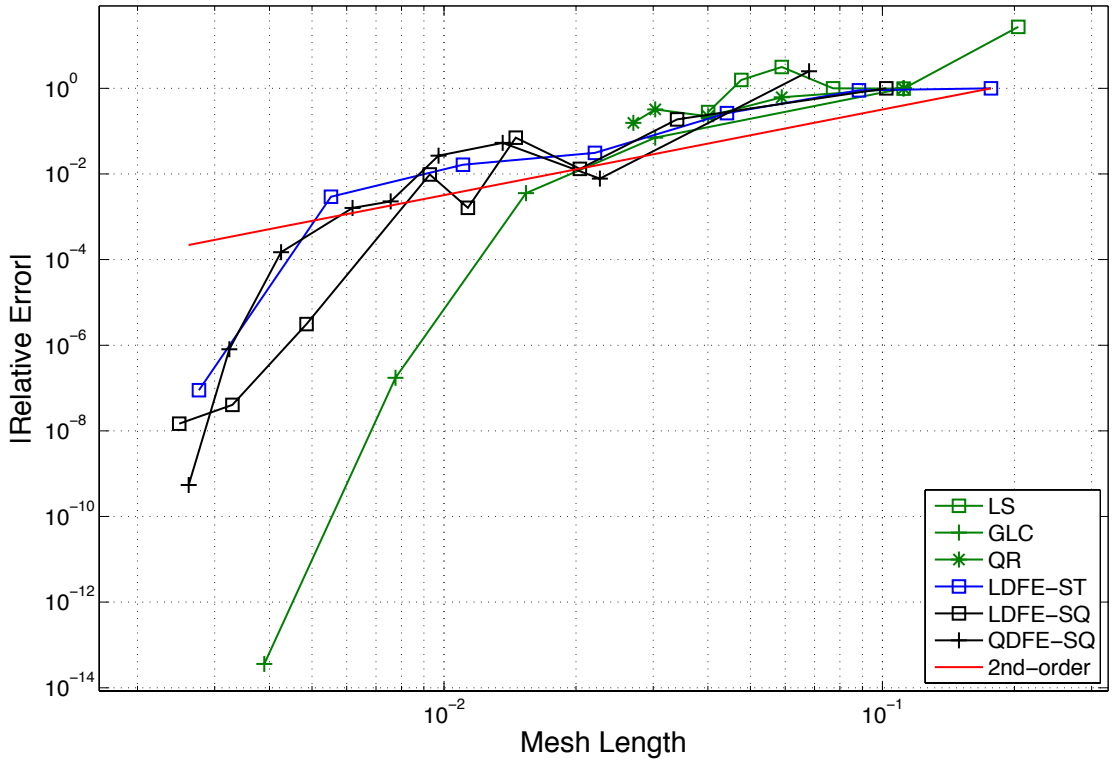

Figure 6.16: Scalar flux error at the duct outlet (35 cm, 95 cm, 35 cm) for the Kobayashi problem using 1.0 cm spatial cells with uniform LS, triangular GC, triangular QR, LDFE-ST, LDFE-SQ and QDFE-SQ.

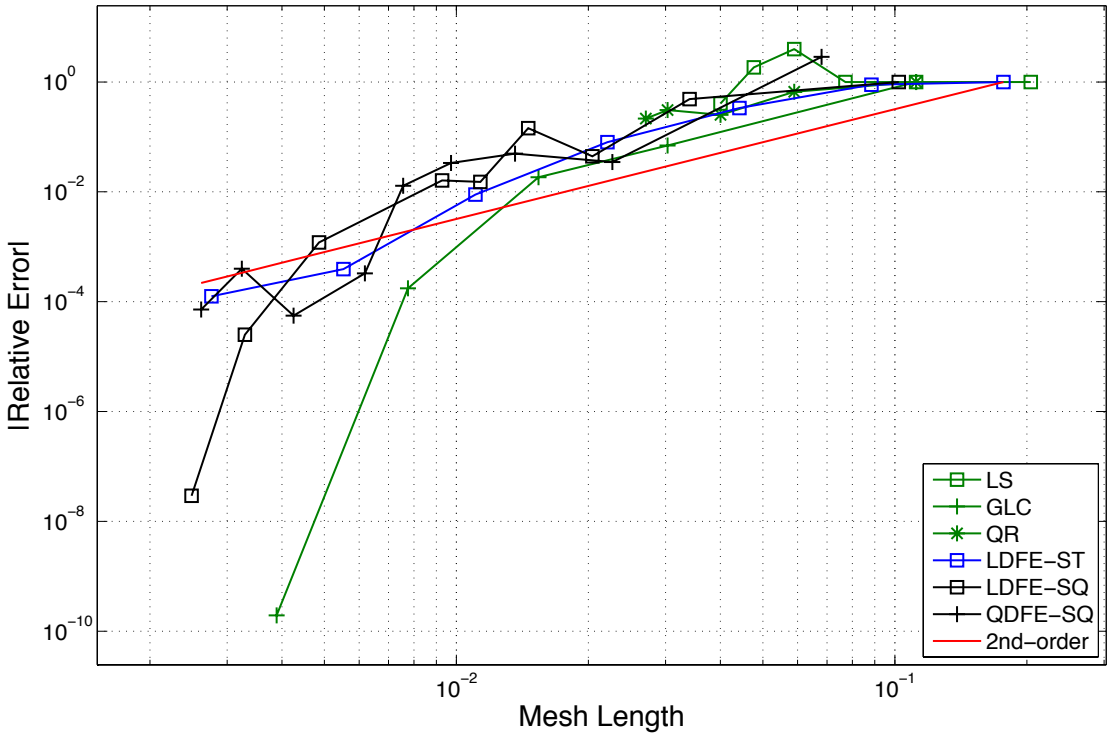

Figure 6.17: Scalar flux error at the duct outlet (35 cm, 95 cm, 35 cm) for the Kobayashi problem using 0.5 cm spatial cells with uniform LS, triangular GC, triangular QR, LDFE-ST, LDFE-SQ and QDFE-SQ.

6.1.6 IM-1 Problem

The Impurity-Model-1 (IM-1) problem from the Texas A&M Center for Exascale Radiation Transport demonstrates the ability of the LDFE-SQ and QDFE-SQ angular quadratures to accurately form the scalar flux for a problem with anisotropic scattering, while producing particle-conservation errors that are small compared to other discretization errors affecting the solution. The purpose of the IM-1 experiment is to infer the impurity concentration within a graphite slab, with impurities modeled as an equivalent boron concentration. The IM-1 experiment is illustrated in Fig. 6.18, consisting of an AmBe source surrounded by high-density polyethelene (HDPE). An air channel connects the AmBe source to a block of graphite. A boron

trifluoride (BF3) detector is placed on the other side of the graphite block to measure the exiting neutron flux. The absorption rate in the BF3 detector is used to determine the impurity concentration within the graphite slab. The IM-1 experiment is modeled using 4th-order (P4) scattering. Previous testing have indicated that the calculated absorption rate in the BF3 detector does not change significantly using above 3rd-order (P3) scattering. The majority of the anisotropic scattering is due to carbon-12 in the graphite and polyethylene as well as hydrogen in the polyethylene. Fig. 6.19 plots the carbon-12 neutron elastic scattering probability per unit cosine, in the center-of-mass reference frame, for various neutron energies, which shows scattering is forward-peaked (i.e., much more likely to scatter with a cosine angle close to one) at some higher neutron energies (>2.0E6 eV) and backward-peaked at others. The QOIs for this problem are the absorption rate error in the detector, and the maximum particle-conservation error over all spatial cells as a function of h. The absorption rate is

$$R = \sum_{i=1}^{N_e} \sum_{j=1}^{N_s} \Sigma_{a,i} \Phi_{ij} V_j \ , \tag{6.4}$$

where N_e is the total number of energy groups, N_s is the total number of spatial cells within the detector, $\Sigma_{a,i}$ is the absorption cross section for energy group i, Φ_{ij} is the scalar flux for energy group i in spatial cell j, and V_j is the volume of spatial cell j. The particle-conservation error for each spatial cell is

$$\epsilon = \frac{G - L}{G}, \tag{6.5}$$

where G is the gain rate (from external sources, scattering sources, and inflow), and L is the loss rate (from absorption and outflow). The IM-1 problem uses the PWLD method for spatial discretization along with a 99-group structure for energy

discretization (see Section 2.2 for a discussion on energy discretization).

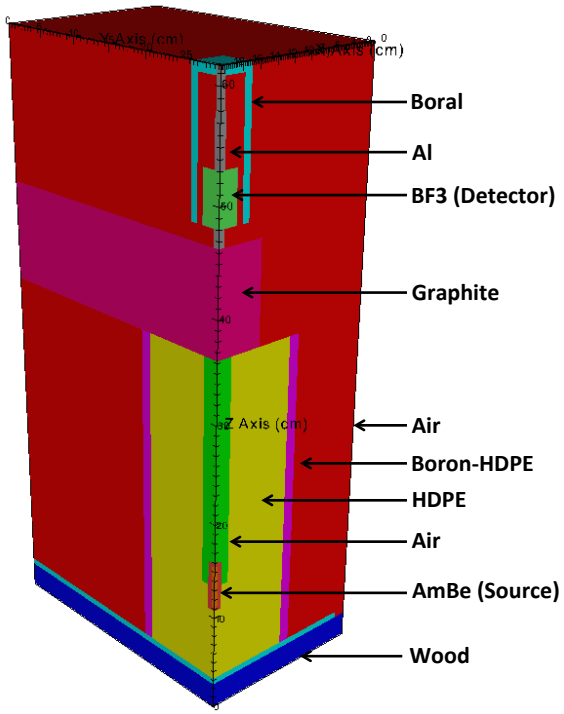

Figure 6.18: Problem setup for the IM-1 problem. Materials as marked.

Fig. 6.20 plots the absorption rate error (equivalent to a weighted scalar-flux error, with lower-energy groups having more weight) in the BF3 detector, and the maximum particle-conservation error over all spatial cells as a function of h. Due to the large computational resources required to run this problem, we could not perform a high-direction angular quadrature run to obtain the reference solution. Instead, the reference solution was found by fitting

$$R_{\text{ref}} - R_h = Ch^P \ , \tag{6.6}$$

where R_{ref} is the reference absorption rate, R_h is the absorption rate for a given h,

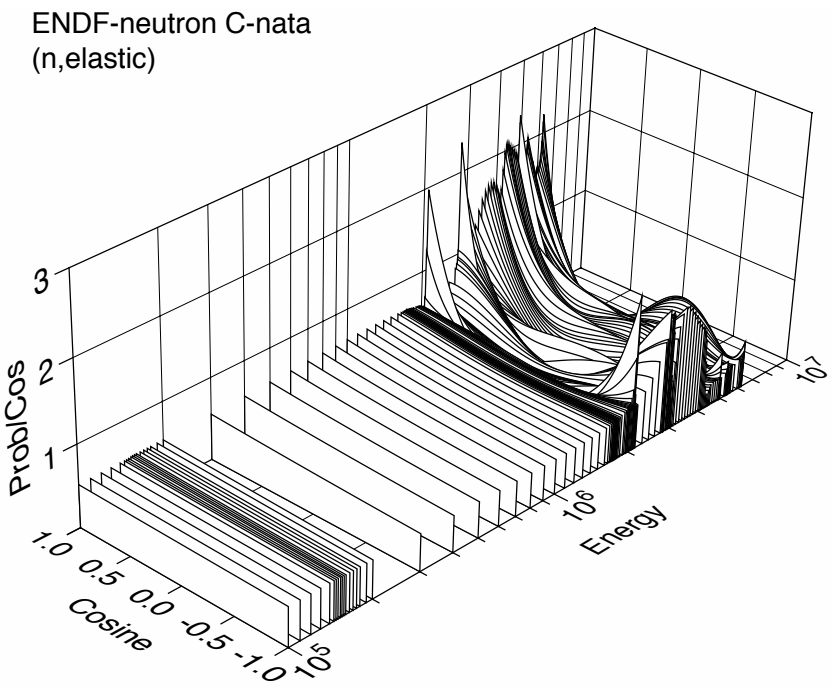

Figure 6.19: Carbon-12 neutron elastic scattering probability per unit cosine, in the center-of-mass reference frame, for various neutron energies.

C is a constant, and P is the error convergence rate. The results show absorption rate error decreases by ≈2.5-order for all DFEM-based angular quadratures, and the maximum particle-conservation error decreases by ≈4th-order as a function of h. We note that the particle-conservation error is several orders of magnitude lower than the absorption rate error for all h.

6.1.7 Criticality Problem

This subsection demonstrates the ability of the LDFE-SQ and QDFE-SQ angular quadratures to accurately calculate the eigenvalue (k_{eff}) of a simple criticality problem, while producing particle-conservation errors that are small compared to other discretization errors affecting the solution. The criticality problem at hand is a two-dimensional square with 12 cm sides surrounded by vacuum. The square is composed

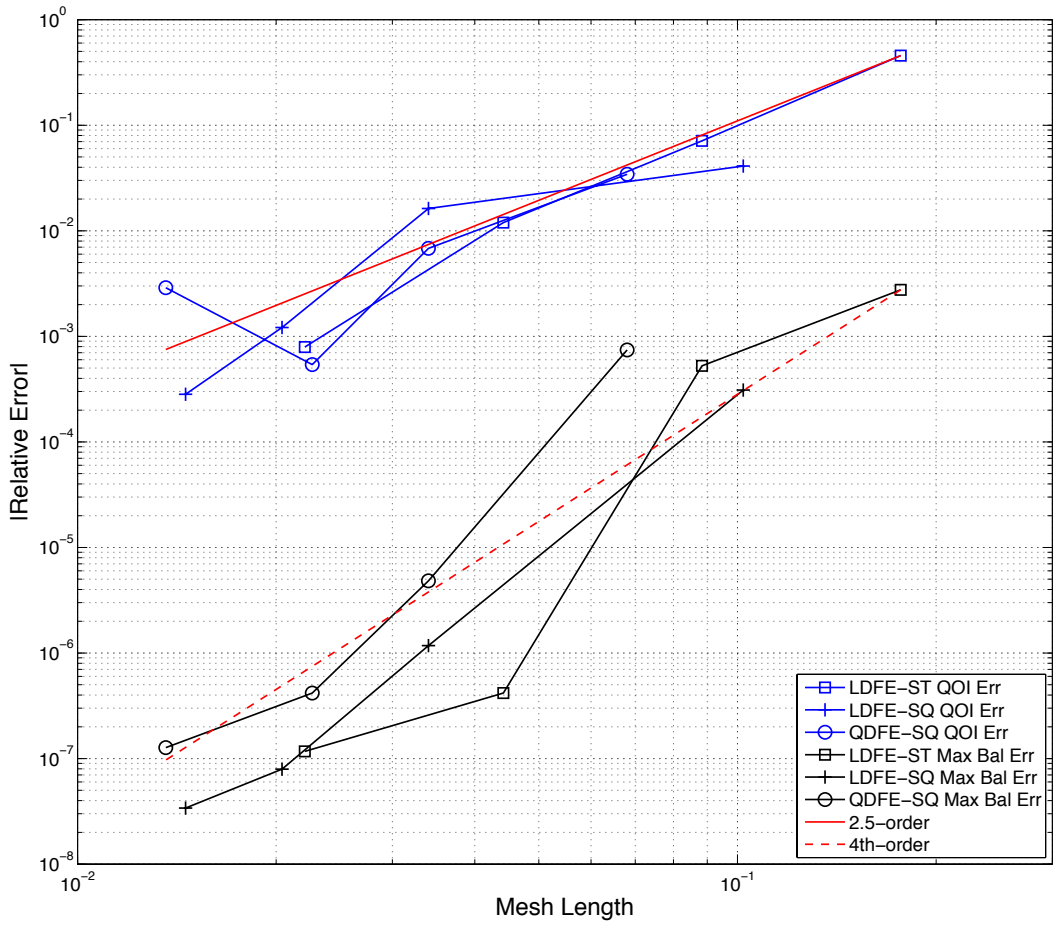

Figure 6.20: QOI (absorption rate) error and maximum particle-conservation error as a function of angular mesh length.

of uranium (U-235 and U-238 composite) and modeled using a 33-group structure for energy discretization (see Section 2.2 for a discussion on energy discretization) with third-order (P3) scattering. The problem was run in PDT using the PWLD method for spatial discretization.

The computational results show the DFEM angular quadratures (i.e., LDFE-ST, LDFE-SQ and QDFE-SQ) produce small particle-conservation errors (≈1E-8 to 1E-9) for this particular problem even at low direction counts. Fig. 6.21 plots k-eff error as a function of h using triangular GC, LDFE-ST, LDFE-SQ and QDFE-

SQ angular quadratures. The reference solution was obtained using an 8256-point per quadrant triangular GC angular quadrature. The LDFE-ST, LDFE-SQ and QDFE-SQ angular quadratures were tested up to 4096, 3888 and 5292 directions per quadrant, respectively. The computational results show the DFEM angular quadratures rapidly converge to the reference solution before plateauing at the k-eff error tolerance of 1E-6. The triangular GC angular quadrature converges to the reference solution by 2nd-order.

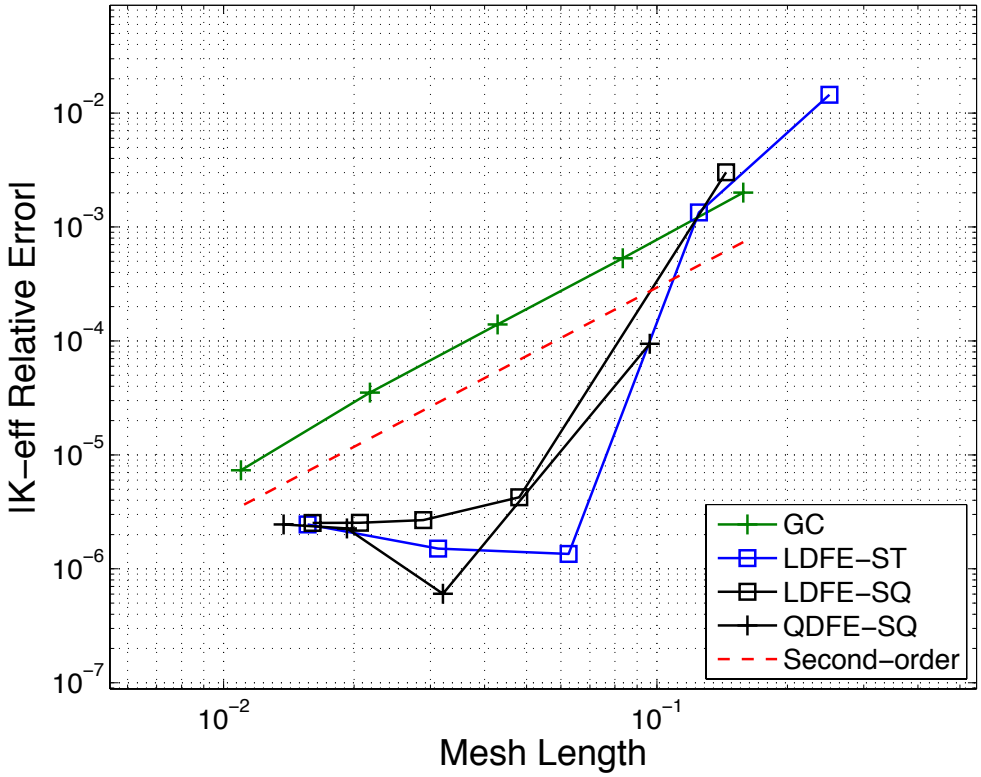

Figure 6.21: K-eff error as a function of angular mesh length using triangular GC, LDFE-ST, LDFE-SQ and QDFE-SQ.

6.2 Mapping Performance

We demonstrate the ability of the new mapping and fix-up algorithms to pass increasing-degree SH functions, and the angular flux solution for a difficult radiation transport problem between differently-refined LDFE-SQ and QDFE-SQ angular quadratures. As discussed in Section 5, an "optimal" mapping algorithm should preserve both the shape and the angular moments of interest from the incoming solution.

6.2.1 Spherical Harmonics Mapping

For certain radiation transport problems of interest, the angular flux solution is smooth, and thus can be well-approximated by SH expansions. However, for other problems of interest, the angular flux solution may be discontinuous or nearly discontinuous in angle. Therefore, it is important to demonstrate the new mapping and fix-up algorithms can accurately pass both increasing-degree SH functions and discontinuous functions in angle between differently-refined LDFE-SQ and QDFE-SQ angular quadratures. As discussed in Section 5, we are interested in preserving the 0th and 1st angular moments for LDFE-SQ mapping, and the 0th through 2nd angular moments for QDFE-SQ mapping. The fix-up algorithm is applied when the mapped solution does not satisfy prescribed limits, which are set as the analytic minimum and maximum for the given angular-flux function. For LDFE-SQ coarse-to-fine (resp., fine-to-coarse) mapping, in this subsection we pass SH functions over the first octant from a 192-point per octant to a 768-point per octant (resp., a 3072-point per octant to a 768-point per octant) LDFE-SQ angular quadrature. For QDFE-SQ coarse-to-fine (resp., fine-to-coarse) mapping, we pass SH functions from a 243-point per octant to a 2187-point per octant (resp., a 19,683-point per octant to a 2187-point per octant) QDFE-SQ angular quadrature. Figs. 6.22 to 6.33 plot

the LDFE-SQ and QDFE-SQ mapped results over the azimuthal (γ) and polar (θ) angular domains in the first octant. The meshed surface represents the analytic solution, and the color of each mapped solution point represents its relative error compared to the analytic solution. Tables 6.4 to 6.6 summarize the LDFE-SQ and QDFE-SQ mapped results.

6.2.1.1 Linear Spherical Harmonics Function

Consider the following linear SH function:

$$f\left(\vec{\Omega}\right) = 1 + \mu + \eta + \xi \; . \tag{6.7}$$

Figs. 6.22 and 6.23 show the LDFE-SQ coarse-to-fine and fine-to-coarse mapped solutions, respectively. The results show both coarse-to-fine and fine-to-coarse LDFE-SQ mapping preserves the 0th and 1st angular moments to machine precision (MP) defined as $\leq$1E-12 relative error. The relative error in the coarse-to-fine mapped solution ranges from -4.2E-3 to +4.6E-3, and does not require fix-up. The relative error in the fine-to-coarse mapped solution ranges from -9.2E-2 to +9.3E-2, and requires fix-up. The fix-up algorithm produces a mapped solution which satisfies the prescribed limits, and preserves the 0th angular moment to MP, but introduces $\approx$1.0E-9 relative error into the 1st angular moment preservation.

Figs. 6.24 and 6.25 show the QDFE-SQ coarse-to-fine and fine-to-coarse mapped solutions, respectively. The results show both coarse-to-fine and fine-to-coarse QDFE-SQ mapping preserves the 0th through 2nd angular moments to MP. The relative error in the coarse-to-fine mapped solution ranges from -8.2E-3 to +1.4E-2, and requires fix-up. The fix-up algorithm produces a mapped solution which satisfies the prescribed limits, and preserves the 0th angular moment to MP, but introduces $\approx$1.0E-8 and $\approx$1.0E-7 relative errors into the 1st and 2nd angular moment preserva-

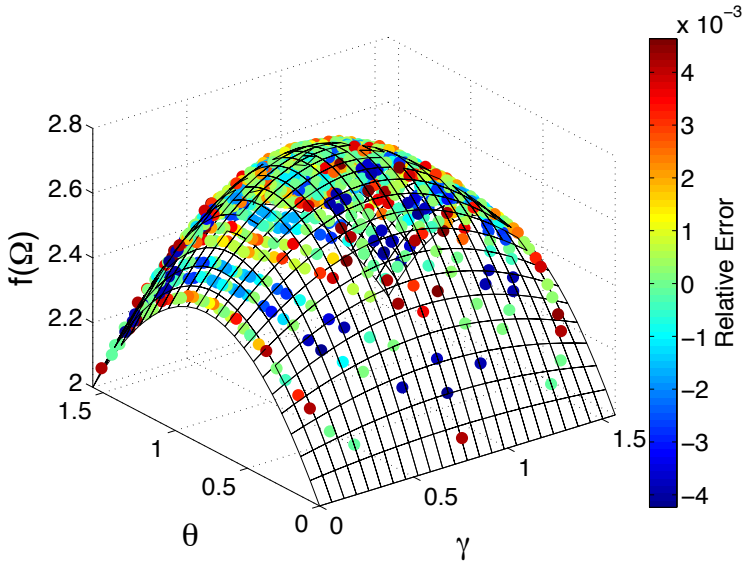

Figure 6.22: LDFE-SQ coarse-to-fine mapping for $f(\vec{\Omega}) = 1 + \mu + \eta + \xi$ from a 192-point to a 768-point per octant LDFE-SQ angular quadrature without fix-up (not required).

tions, respectively. The relative error in the fine-to-coarse mapped solution ranges from -2.6E-3 to +3.5E-3, and also requires fix-up. The fix-up algorithm produces a mapped solution which satisfies the prescribed limits, and preserves the 0th angular moment to MP, but introduces ≈1.0E-8 and ≈1.0E-7 relative errors into the 1st and 2nd angular moment preservations, respectively. We note that simple interpolation of the QDFE basis functions for mapping linear SH functions should produce mapped solutions that have no error relative to the analytic solution, since the linear SH function lives in the basis space for both the coarse and fine QDFE-SQ angular quadratures. The mapped solution should also exactly preserve the 0th and 1st angular moments, which only require the integration of up to 2nd-degree SH functions (shown to be exact in Section 6.1.1). Errors in the mapped solution relative to the analytic solution are introduced by the requirement of the QDFE-SQ mapping to exactly preserve the 2nd angular moments, which requires integration of up to

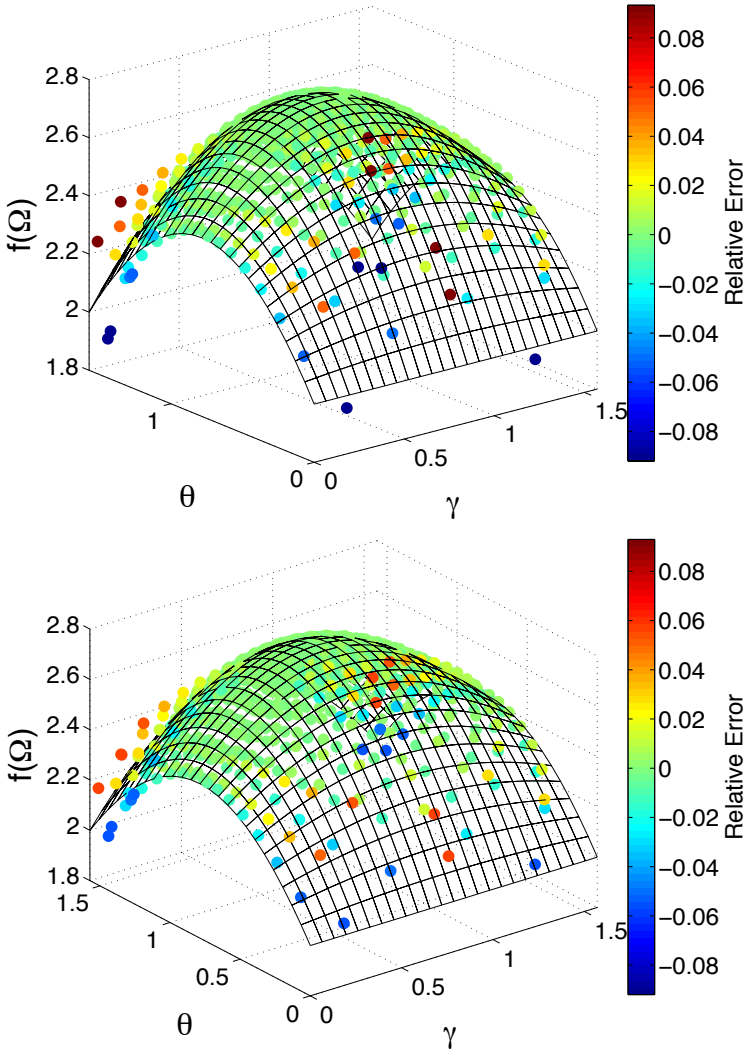

Figure 6.23: LDFE-SQ fine-to-coarse mapping for $f(\vec{\Omega}) = 1 + \mu + \eta + \xi$ from a 3072-point to a 768-point per octant LDFE-SQ angular quadrature without (top) and with (bottom) fix-up.

3rd-degree SH functions.

6.2.1.2 Fifth-Degree Spherical Harmonics Function

Consider the following 5th-degree SH function:

$$f\left(\vec{\Omega}\right) = 1 + \mu^5 + \eta^5 + \xi^5 \; . \tag{6.8}$$

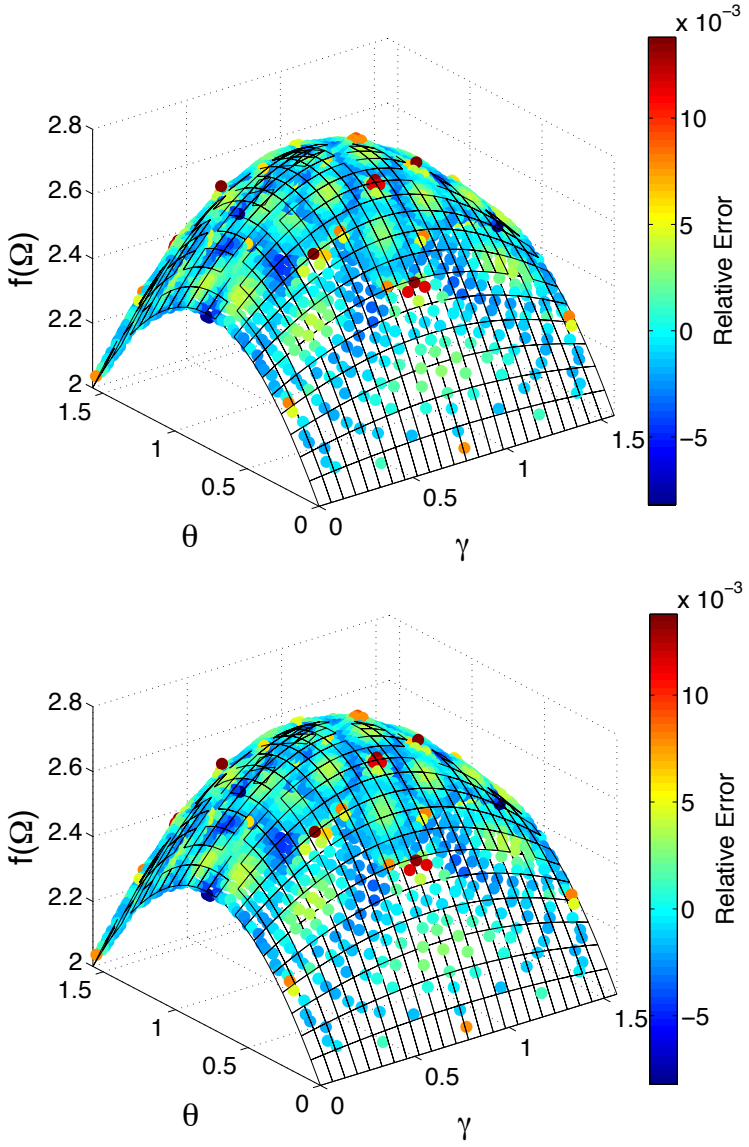

Figure 6.24: QDFE-SQ coarse-to-fine mapping for $f(\vec{\Omega}) = 1 + \mu + \eta + \xi$ from a 243-point to a 2187-point per octant QDFE-SQ angular quadrature without (top) and with (bottom) fix-up.

Figs. 6.26 and 6.27 show the LDFE-SQ coarse-to-fine and fine-to-coarse mapped solutions, respectively. The results show both coarse-to-fine and fine-to-coarse LDFE-SQ mapping preserves the 0th and 1st angular moments to MP. The relative error in the coarse-to-fine mapped solution ranges from -1.2E-2 to +9.8E-3, and requires fix-up.

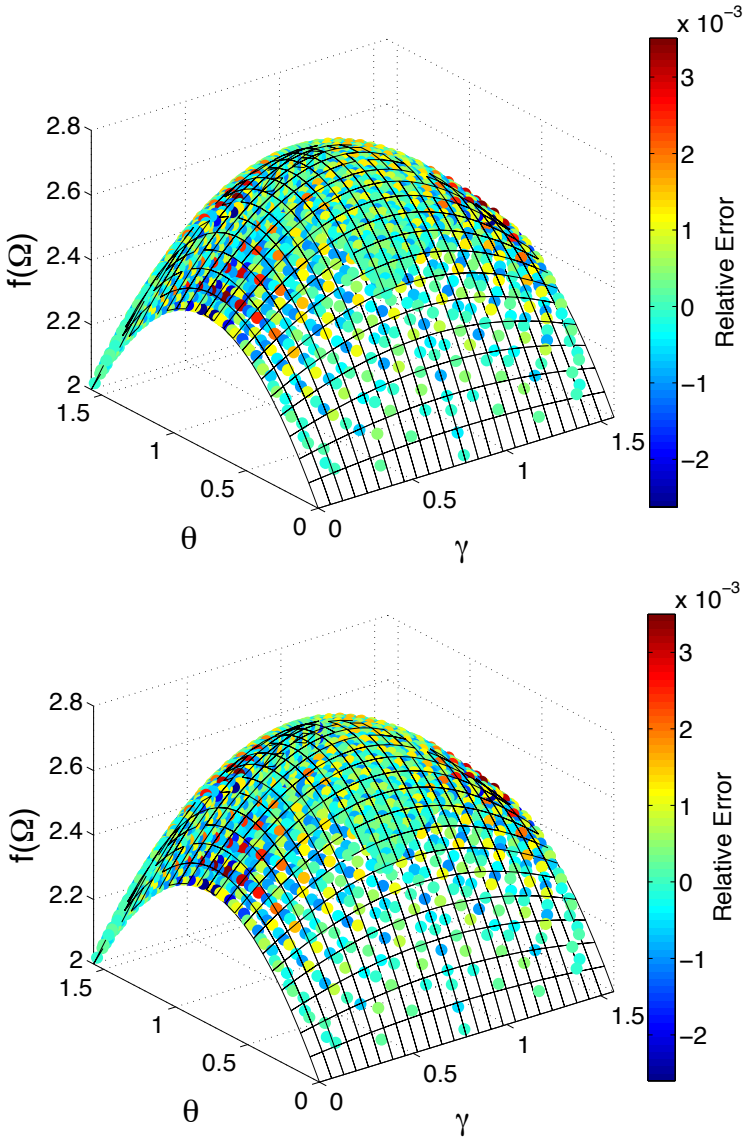

Figure 6.25: QDFE-SQ fine-to-coarse mapping for $f(\vec{\Omega}) = 1 + \mu + \eta + \xi$ from a 19,683-point to a 2187-point per octant QDFE-SQ angular quadrature without (top) and with (bottom) fix-up.

The fix-up algorithm produces a mapped solution which satisfies the prescribed limits, and preserves the 0th angular moment to MP, but introduces ≈1.0E-6 relative error into the 1st angular moment preservation. The relative error in the fine-to-coarse mapped solution ranges from -2.9E-1 to +3.0E-1, and requires fix-up. The

majority of the error is attributed to over- and under-shoots near the octant boundaries. The fix-up algorithm produces a mapped solution which satisfies the prescribed limits, and preserves the 0th angular moment to MP, but introduces ≈1.0E-7 relative error into the 1st angular moment preservation.

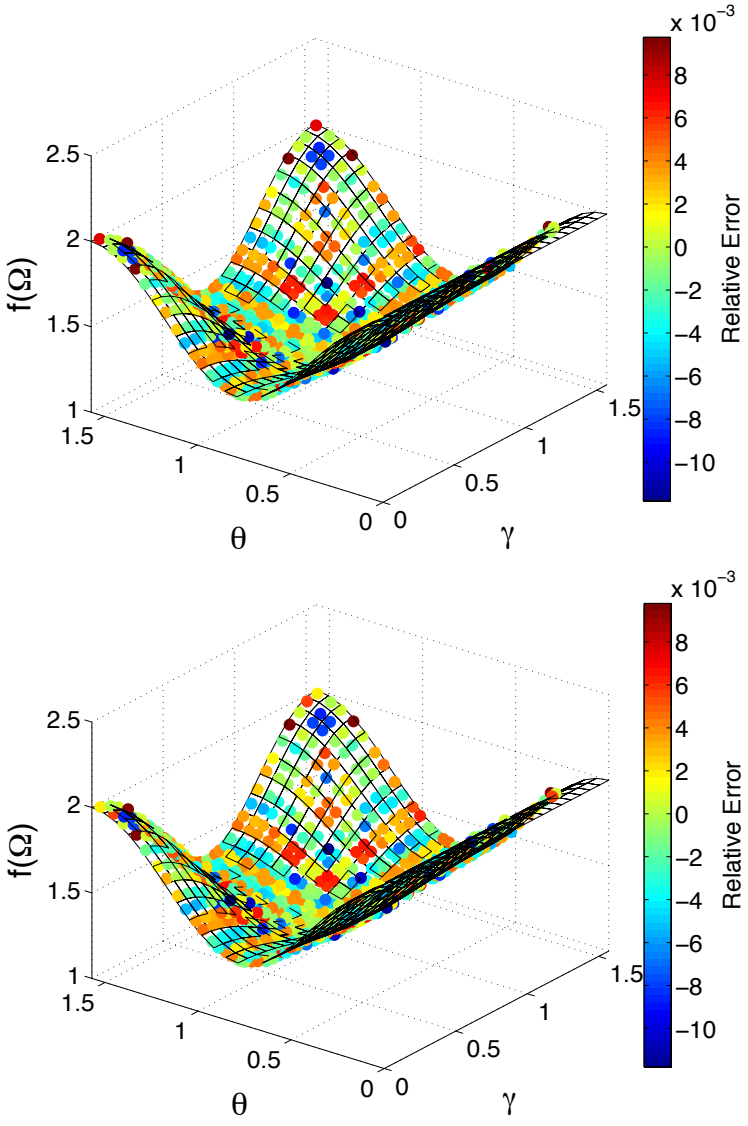

Figure 6.26: LDFE-SQ coarse-to-fine mapping for $f(\vec{\Omega}) = 1 + \mu^5 + \eta^5 + \xi^5$ from a 192-point to a 768-point per octant LDFE-SQ angular quadrature without (top) and with (bottom) fix-up.

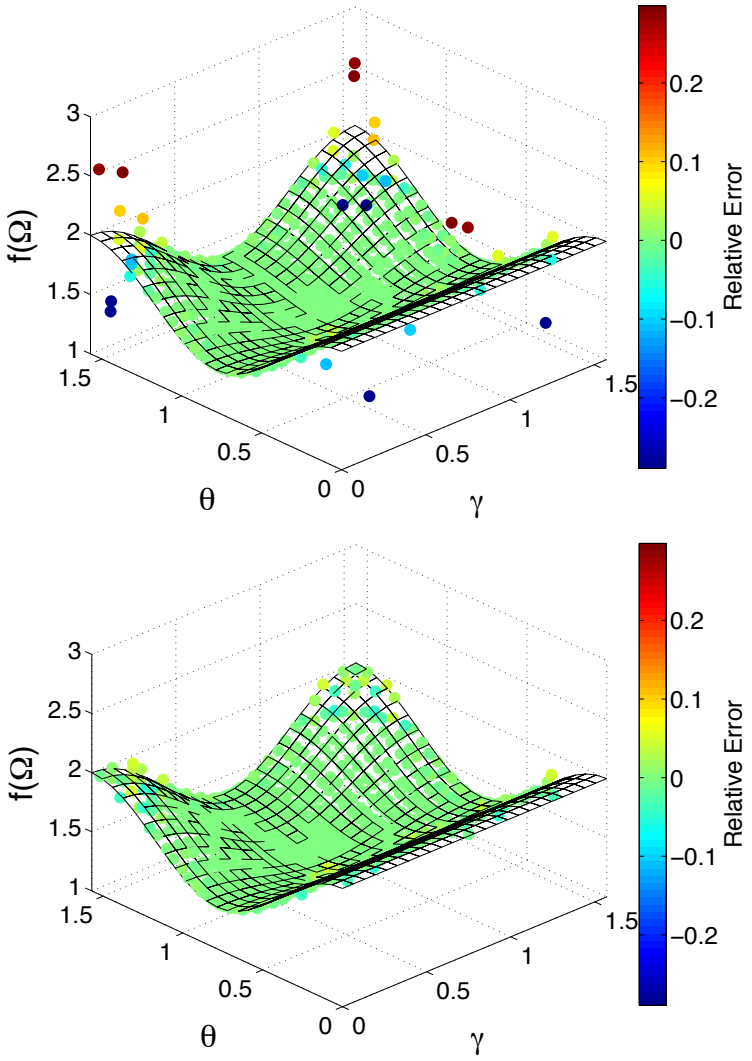

Figure 6.27: LDFE-SQ fine-to-coarse mapping for $f(\vec{\Omega}) = 1 + \mu^5 + \eta^5 + \xi^5$ from a 3072-point to a 768-point per octant LDFE-SQ angular quadrature without (top) and with (bottom) fix-up.

Figs. 6.28 and 6.29 show the QDFE-SQ coarse-to-fine and fine-to-coarse mapped solutions, respectively. The results show both coarse-to-fine and fine-to-coarse QDFE-SQ mapping preserves the 0th through 2nd angular moments to MP. The relative error in the coarse-to-fine mapped solution ranges from -3.2E-2 to +1.8E-2, and requires fix-up. The fix-up algorithm produces a mapped solution which satisfies

the prescribed limits, and preserves the 0th angular moment to MP, but introduces ≈1.0E-7 relative error into both the 1st and 2nd angular moment preservations. The relative error in the fine-to-coarse mapped solution ranges from -5.7E-3 to +6.7E-3, and requires fix-up. The fix-up algorithm produces a mapped solution which satisfies the prescribed limits, and preserves the 0th angular moment to MP, but introduces ≈1.0E-9 and ≈1.0E-8 relative errors into the 1st and 2nd angular moment preservations, respectively.

6.2.1.3 Discontinuous Function

Consider the following discontinuous function:

$$f\left(\vec{\Omega}\right) = \begin{cases} 1, \ \Delta\gamma \text{ and } \Delta\theta \in (\pi/8, 3\pi/8) \\ 0, \ \text{Elsewhere} \end{cases} . \tag{6.9}$$

Figs. 6.26 and 6.27 show the LDFE-SQ coarse-to-fine and fine-to-coarse mapped solutions, respectively. The results show both coarse-to-fine and fine-to-coarse LDFE-SQ mapping preserves the 0th and 1st angular moments to MP. The absolute error in the coarse-to-fine mapped solution ranges from -1.0E0 to +1.0E0, and requires fix-up. The majority of the error is attributed to over- and under-shoots near the solution discontinuity. The fix-up algorithm produces a mapped solution which satisfies the prescribed limits, and preserves the 0th angular moment to MP, but introduces ≈1.0E-3 relative error into the 1st angular moment preservation. The absolute error in the fine-to-coarse mapped solution ranges from -8.9E-1 to +9.6E-1, and also requires fix-up. The majority of the error is again attributed to over- and under-shoots near the solution discontinuity. The fix-up algorithm produces a mapped solution which satisfies the prescribed limits, and preserves the 0th angular moment to MP, but introduces ≈1.0E-4 relative error into the 1st angular moment preservation.

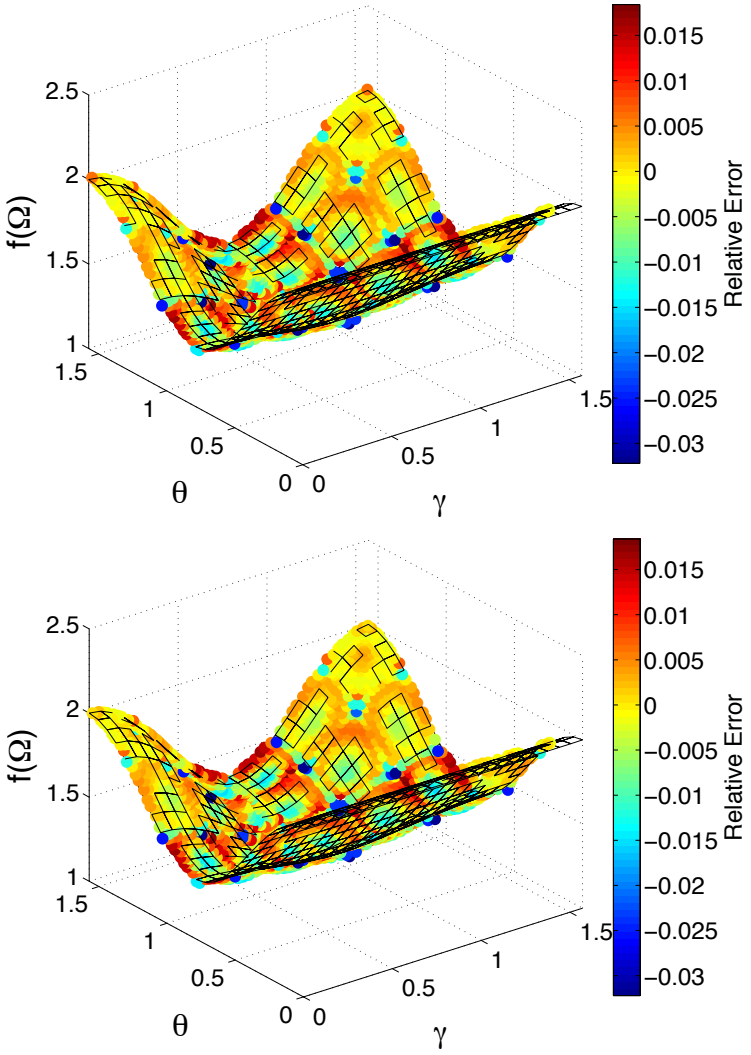

Figure 6.28: QDFE-SQ coarse-to-fine mapping for $f(\vec{\Omega}) = 1 + \mu^5 + \eta^5 + \xi^5$ from a 243-point to a 2187-point per octant QDFE-SQ angular quadrature without (top) and with (bottom) fix-up.

Figs. 6.32 and 6.33 show the QDFE-SQ coarse-to-fine and fine-to-coarse mapped solutions, respectively. The results show both coarse-to-fine and fine-to-coarse QDFE-SQ mapping preserves the 0th through 2nd angular moments to MP. The absolute error in the coarse-to-fine mapped solution ranges from -1.0E0 to +1.0E0, and requires fix-up. The majority of the error is attributed to over- and under-shoots near

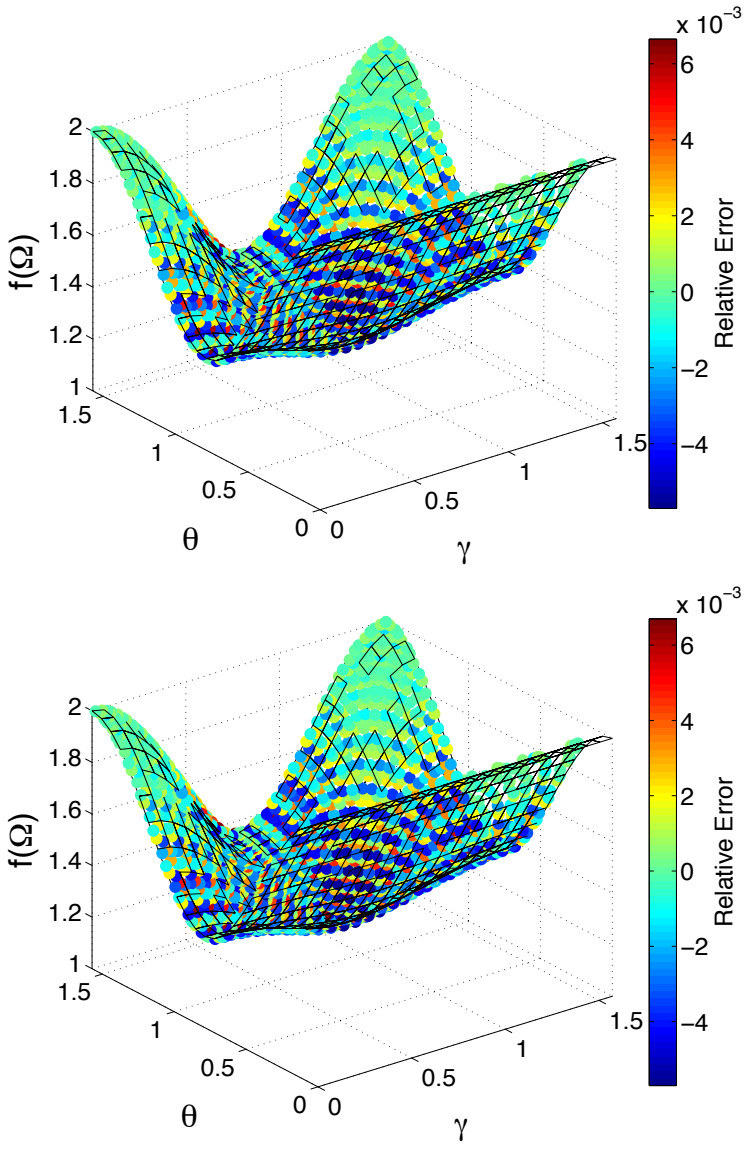

Figure 6.29: QDFE-SQ fine-to-coarse mapping for $f(\vec{\Omega}) = 1 + \mu^5 + \eta^5 + \xi^5$ from a 19,683-point to a 2187-point per octant QDFE-SQ angular quadrature without (top) and with (bottom) fix-up.

the solution discontinuity. The fix-up algorithm produces a mapped solution which satisfies the prescribed limits, and preserves the 0th angular moment to MP, but introduces ≈1.0E-3 relative error into both the 1st and 2nd angular moment preser-

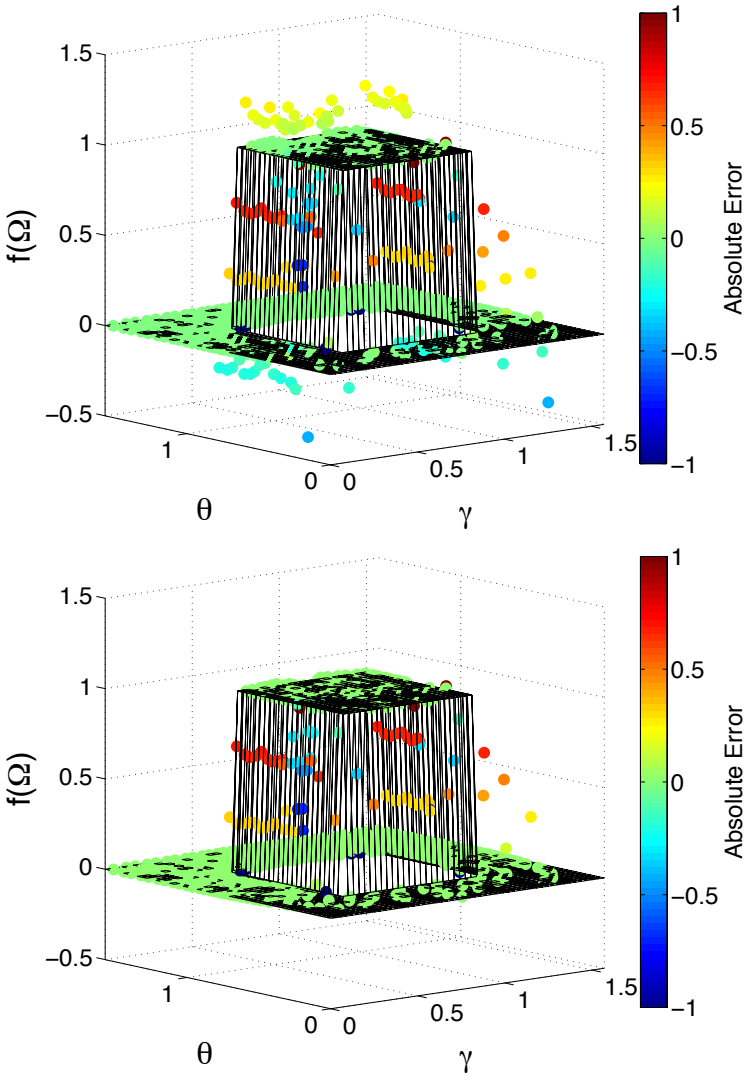

Figure 6.30: LDFE-SQ coarse-to-fine mapping for $f(\vec{\Omega}) = 1,\ \Delta\gamma, \Delta\theta \in (\pi/8, 3\pi/8)$, , 0 elsewhere from a 192-point to a 768-point per octant LDFE-SQ angular quadrature without (top) and with (bottom) fix-up.

vations. The absolute error in the fine-to-coarse mapped solution ranges from -5.3E-1 to +5.7E-1, and requires fix-up. The majority of the error is again attributed to over and under-shoots near the solution discontinuity. The fix-up algorithm produces a mapped solution which satisfies the prescribed limits, and preserves the 0th angular moment to MP, but introduces ≈1.0E-4 relative error into both the 1st and 2nd

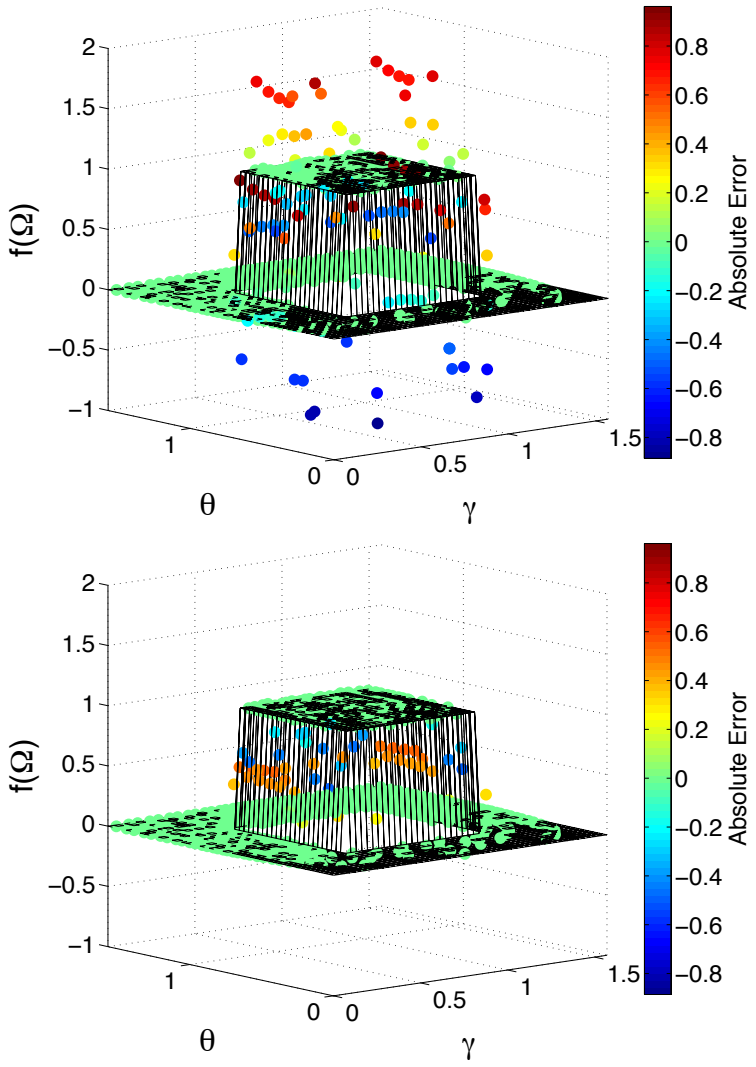

Figure 6.31: LDFE-SQ fine-to-coarse mapping for $f(\vec{\Omega}) = 1,\ \Delta\gamma, \Delta\theta \in (\pi/8, 3\pi/8)$, , 0 elsewhere from a 3072-point to a 768-point per octant LDFE-SQ angular quadrature without (top) and with (bottom) fix-up.

angular moment preservations.

6.2.2 Three-Region Problem

The three-region problem demonstrates the ability of the new mapping and fix-up algorithms to accurately pass the angular flux solution between spatial re-

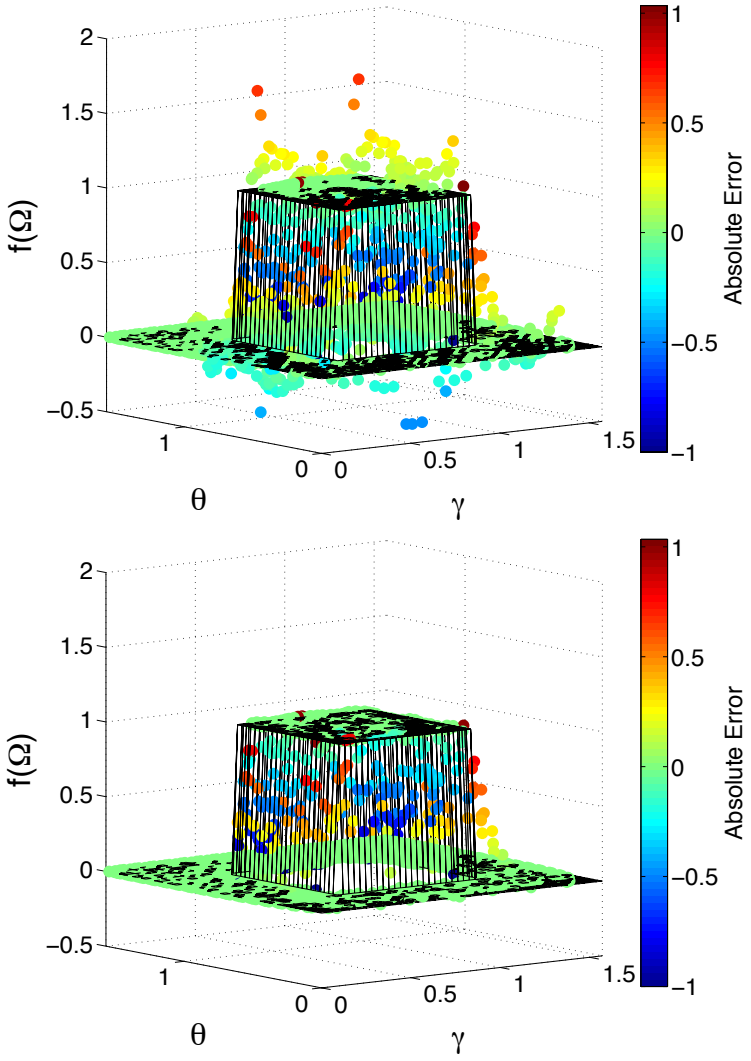

Figure 6.32: QDFE-SQ coarse-to-fine mapping for $f(\vec{\Omega}) = 1,\ \Delta\gamma, \Delta\theta \in (\pi/8, 3\pi/8)$, , 0 elsewhere from a 243-point to a 2187-point per octant QDFE-SQ angular quadrature without (top) and with (bottom) fix-up.

gions with differently-refined DFEM-based angular quadratures (i.e., quadrature regions) for a difficult radiation transport problem. The three-region problem is a 10 cm × 1 cm × 100 cm rectangular box made of pure-absorber material (Σ_a = 0.3 cm^{-1}) surrounded by vacuum. The rectangular box is divided into three quadrature regions along the x-dimension. The left, center and right quadrature regions

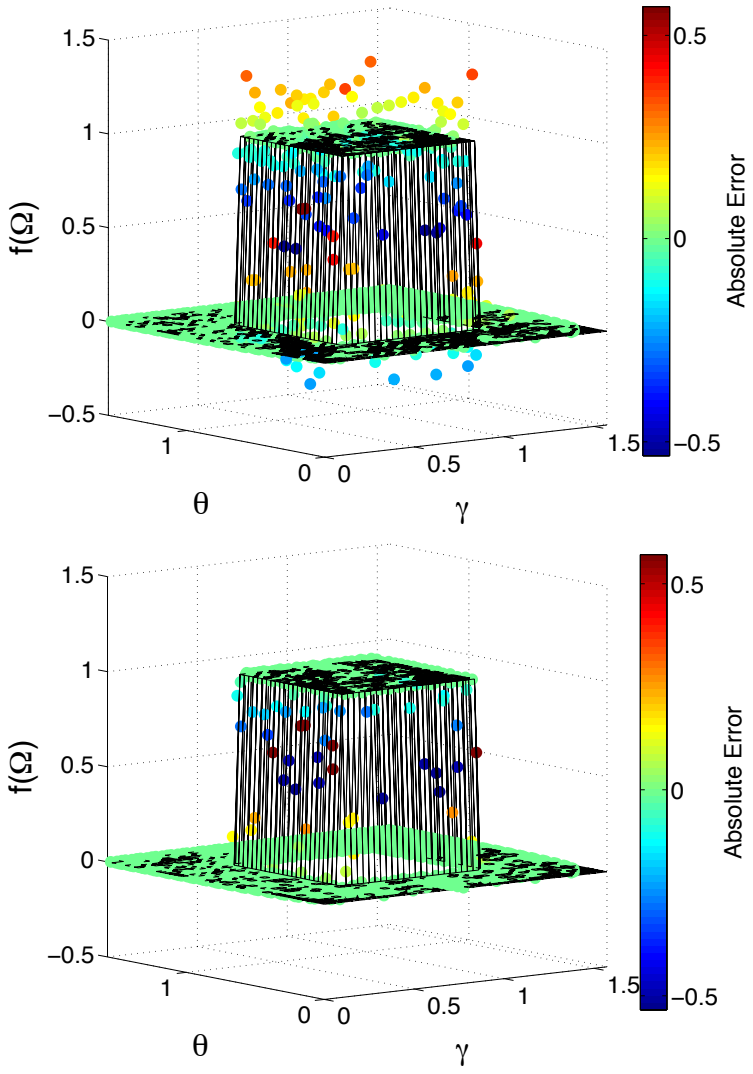

Figure 6.33: QDFE-SQ fine-to-coarse mapping for $f(\vec{\Omega}) = 1,\ \Delta\gamma, \Delta\theta \in (\pi/8, 3\pi/8)$, , 0 elsewhere from a 19,683-point to a 2187-point per octant QDFE-SQ angular quadrature without (top) and with (bottom) fix-up.

span $x \in (0\text{ cm}, 1\text{ cm})$, $x \in (1\text{ cm}, 9\text{ cm})$ and $x \in (9\text{ cm}, 10\text{ cm})$, respectively. A uniformly-distributed isotropic source ($q = 100.0$ neutron/cm^{3}s $\cdot$ ster) is placed into the left quadrature region. The PWLD method is used for spatial discretization. The three-region problem is a difficult mapping problem because the thin profile in the y-dimension and the tall profile in the z-dimension causes the incident angular

flux solution at the right quadrature region interface ($x = 9$ cm) to be very peaked around $\mu = 1$. As shown in Section 6.2.1, the mapping algorithm has difficulty mapping near solution discontinuities (or near discontinuities). The QOIs are the mapped solution errors, and the moment preservation errors across the right quadrature region interface. The reference solution is obtained by setting all three quadrature regions to the same refinement, which eliminates mapping errors. We compare the results using (1) the new mapping algorithm without fix-up, (2) the new mapping algorithm with fix-up, and (3) the previous mapping algorithm suggested by Jarrell and Adams presented in Section 3.2.4. We run the three-region problem using both uniform and locally-refined angular quadratures. The locally-refined angular quadratures are obtained using the adaptive algorithm presented in Section 5.3.

6.2.2.1 Uniform Mapping

For uniform mapping, we increase the LDFE-SQ angular quadrature refinement going from the left to the right quadrature regions. Table 6.7 shows the LDFE-SQ direction count per octant in each quadrature region with refinement. Fig. 6.34 shows the reference angular flux solution at the right quadrature region interface, generated by running with the same highly-refined (98,304 directions per octant) LDFE-SQ angular quadrature in each quadrature region to avoid introducing mapping errors. We show only the angular flux solution for the positive μ directions, since particles travel only from left to right across the right quadrature region interface. We also note that we are showing only the angular flux solution for the spatial node at $(9 \text{ cm}, 0 \text{ cm}, 0 \text{ cm})$ since the other three spatial nodes at the right quadrature region interface are simply reflections of each other.

Fig. 6.35 shows the mapped angular flux solution across the right quadrature region interface using the previous Jarrell and Adams mapping algorithm. The com-

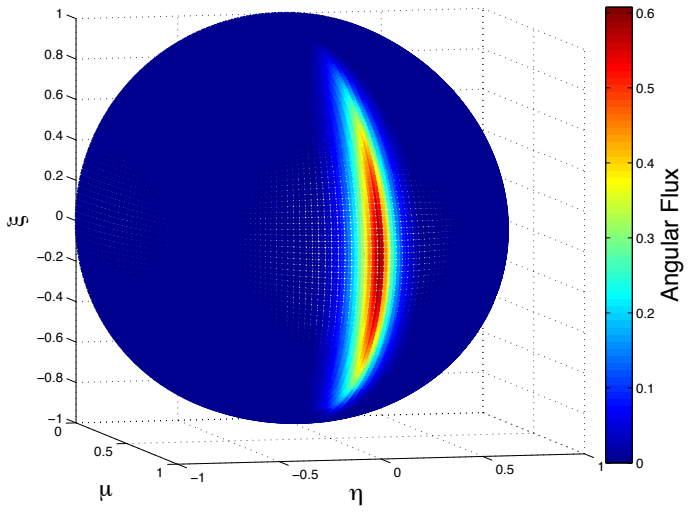

Figure 6.34: Reference angular flux solution at the right quadrature region interface for the three-region problem. The position and color of the points indicate quadrature direction and angular flux solution magnitude, respectively. Results are shown only at (9 cm, 0 cm, 0 cm) since the results in the other three spatial nodes at this interface are simply reflections of each other.

putational results show the shape of the incoming angular flux solution is not well-preserved as evident by comparison with the reference solution in Fig. 6.34. The minimum and maximum angular flux values also exceed the empirical limits established by the reference solution, including negativities. The magnitude by which the empirical limits are exceeded increases with refinement. We also note that, as discussed in Section 3.2.4, the Jarrell and Adams mapping algorithm preserves only the normal partial current (i.e., μ-component of the 1st angular moments for this problem).

Fig. 6.36 shows the mapped angular flux solution using the new mapping algorithm without fix-up. The computational results show the shape of the incoming angular flux solution is well-preserved. Additionally, the 0th and 1st angular moments are preserved to MP. However, minor negativities are present in the mapped angular flux solution near $\mu = 1$, which decrease in magnitude with refinement.

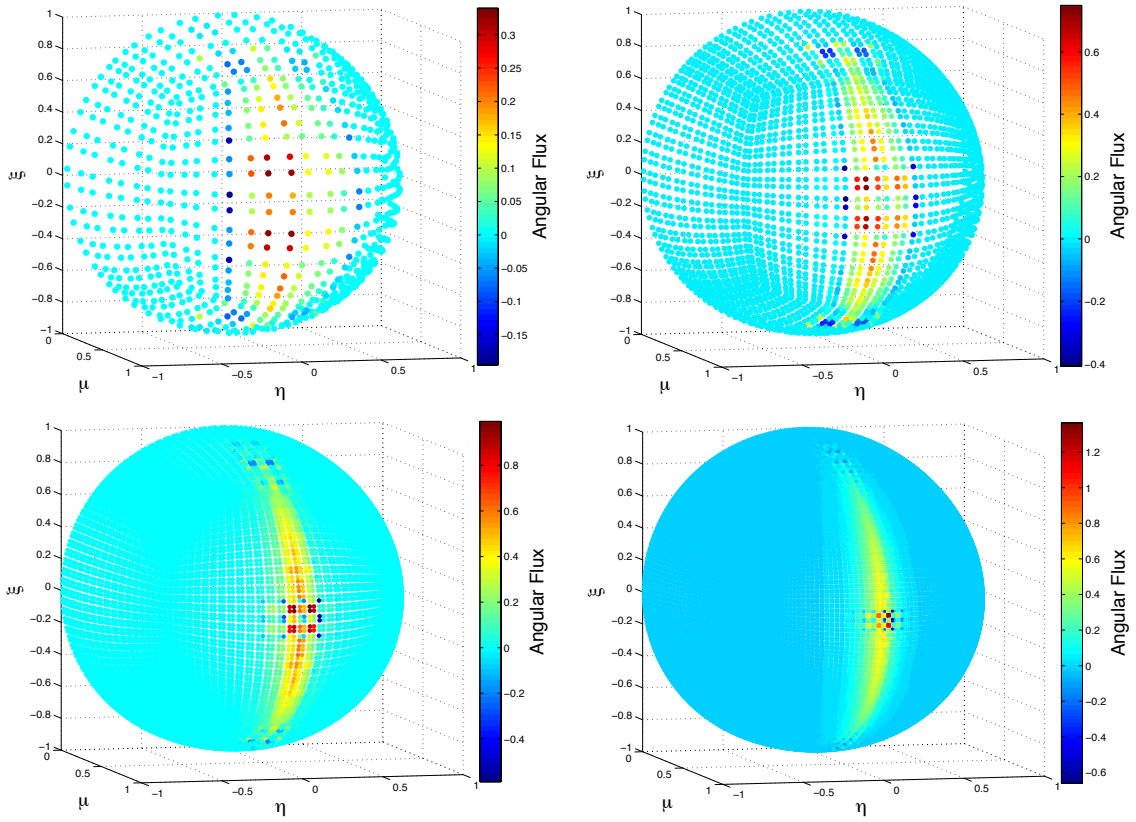

Figure 6.35: Mapped angular flux solution across the right quadrature region interface using the previous Jarrell and Adam's mapping algorithm. Top left, top right, bottom left, and bottom right show the results for runs 1 through 4, respectively, described in Table 6.7. Results are shown only at (9 cm, 0 cm, 0 cm) since the results in the other three spatial nodes at this interface are simply reflections of each other.

Fig. 6.37 shows the mapped angular flux solution using the new mapping algorithm with fix-up. The prescribed limits for this problem were obtained empircally using the reference solution. The results show fix-up preserves the shape of the incoming angular flux solution, satisfies the prescribed limits (which also eliminates negativities), and preserves the 0th angular moment to MP. However, minor errors are introduced into the 1st angular moment preservation, which decreases with refinement.

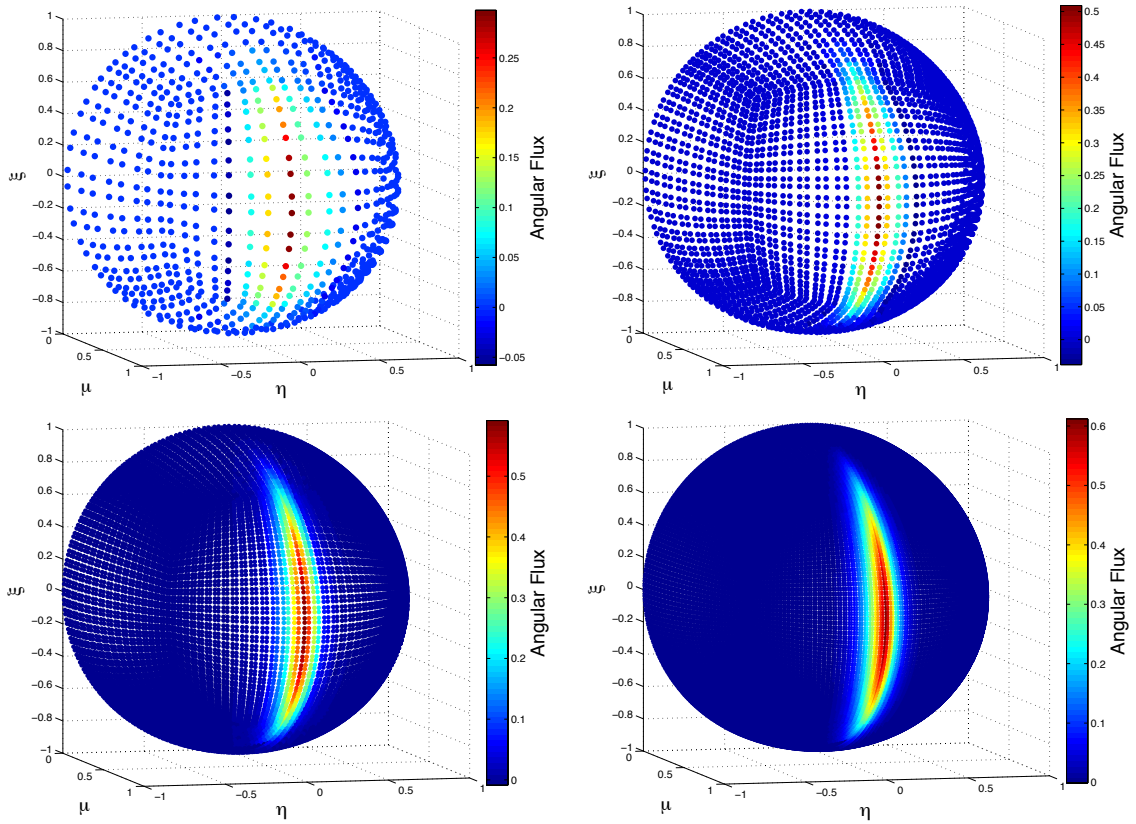

Figure 6.36: Mapped angular flux solution across the right quadrature region interface using the new mapping algorithm without fix-up. Top left, top right, bottom left, and bottom right show the results for runs 1 through 4, respectively, described in Table 6.7. Results are shown only at (9 cm, 0 cm, 0 cm) since the results in the other three spatial nodes at this interface are simply reflections of each other.

Tables 6.8 and 6.9 provides the angular moment preservation errors, and the angular flux extrema using the new mapping algorithm without and with fix-up, respectively. Fig. 6.38 plots the RMS error of the mapped angular flux solution across the right quadrature region interface as a function of the average angular mesh length $h_{\text{cell-ave}}$ defined as

$$h_{\text{cell-ave}} = \frac{1}{\sqrt{\frac{\sum_{i=1}^{N_{\text{cells}}} N_{\text{dirs},i}}{N_{\text{cells}}}}} , \tag{6.10}$$

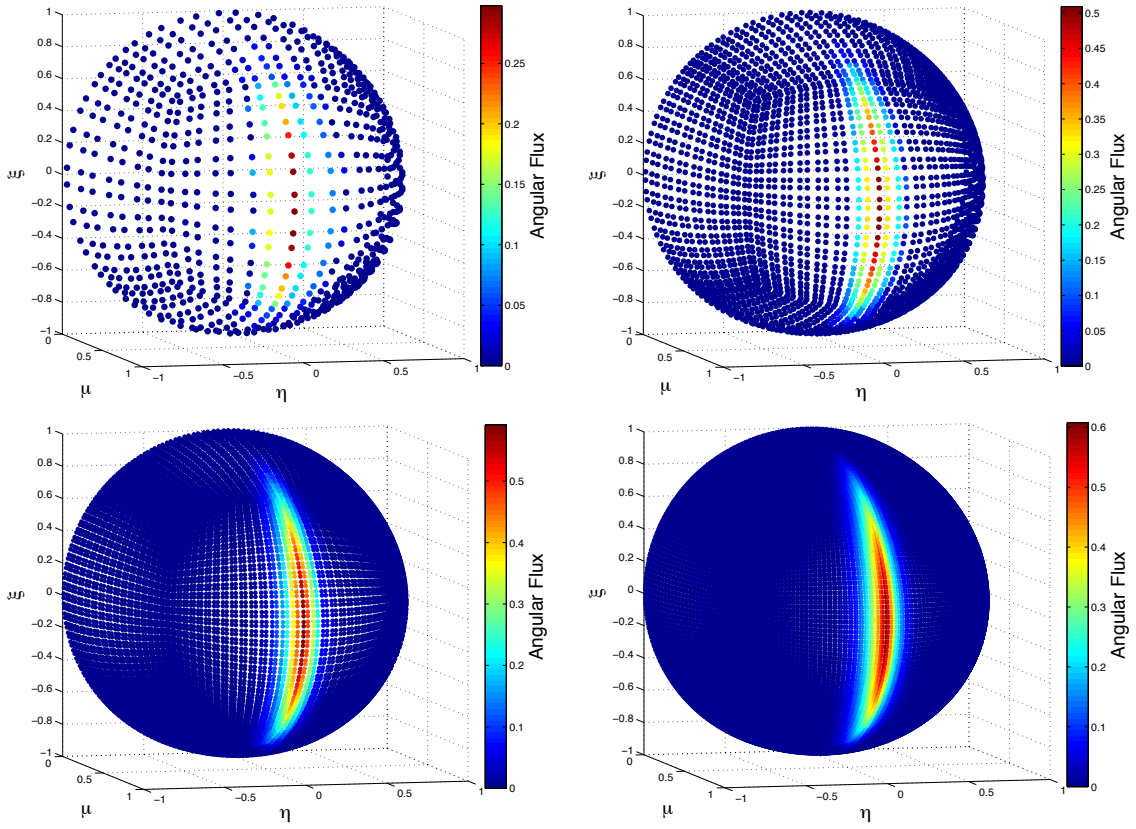

Figure 6.37: Mapped angular flux solution across the right quadrature region interface using the new mapping algorithm with fix-up. Top left, top right, bottom left, and bottom right show the results for runs 1 through 4, respectively, described in Table 6.7. Results are shown only at (9 cm, 0 cm, 0 cm) since the results in the other three spatial nodes at this interface are simply reflections of each other.

where N_{cells} is the total number of spatial cells, and $N_{\text{dirs},i}$ is the total number of directions in spatial cell i. Fig. 6.38 shows the new mapping algorithm (with or without fix-up) reduces the RMS error by 2nd-order, whereas the previous Jarrell and Adams mapping algorithm shows less than 1st-order reduction. Fig. 6.39 plots the maximum absolute error in the mapped angular flux solution across the right quadrature region interface as a function of $h_{\text{cell-ave}}$, which shows the new mapping algorithm (with or without fix-up) reduces the maximum absolute error by 2nd-order,

whereas the previous Jarrell and Adams mapping algorithm shows an increase with refinement.

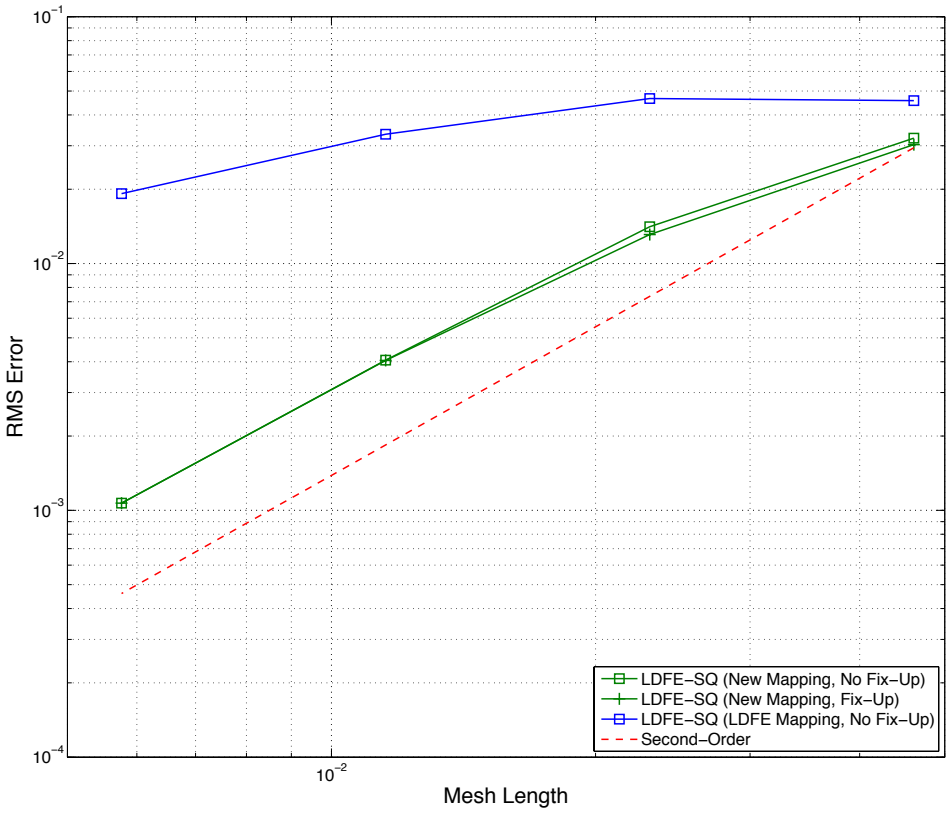

Figure 6.38: RMS error of the mapped angular flux solution across the right quadrature region interface using the new mapping with and without fix-up, and the previous Jarrell and Adam's mapping.

6.2.2.2 Locally-Refined Mapping

For locally-refined mapping, we start with the coarsest (12 directions per octant) LDFE-SQ angular quadrature in each quadrature region. The adaptive algorithm presented in Section 4.4 is then applied to generate the locally-refined angular quadrature for each quadrature region. For this problem, we set $\epsilon_{pw} = 0$, and vary

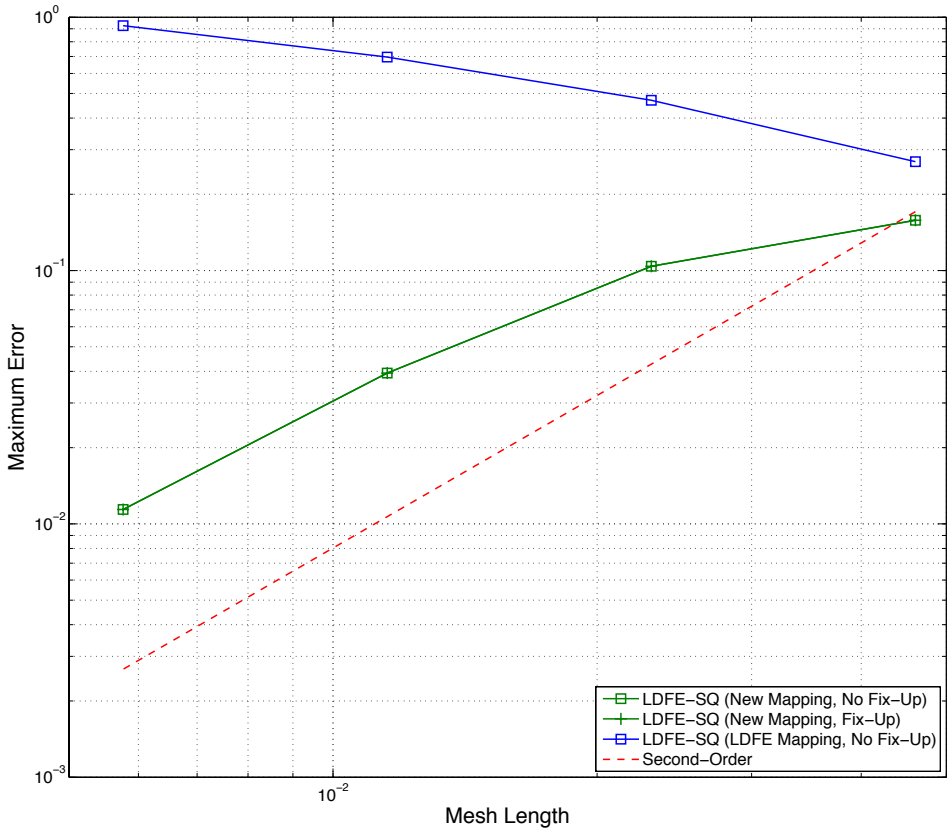

Figure 6.39: Maximum error of the mapped angular flux solution across the right quadrature region interface using the new mapping with and without fix-up, and the previous Jarrell and Adam's mapping.

ϵ_{oc} between 0.01 and 0.3 to avoid over-refining SQs with angular flux solutions near zero. Figs. 6.40 to 6.42 plot the reference angular flux solution at the left and right quadrature region interfaces ($x = 1$ cm and $x = 9$ cm), and at the right boundary of the problem domain ($x = 10$ cm). The reference solutions were generated by using the same highly-refined LDFE-SQ angular quadrature (98,304 directions per octant) in each quadrature region to eliminate mapping errors. We note that we are showing only the angular flux solution for the spatial nodes at $(1\text{ cm}, 0\text{ cm}, 0\text{ cm})$, $(9\text{ cm}, 0\text{ cm}, 0\text{ cm})$ and $(10\text{ cm}, 0\text{ cm}, 0\text{ cm})$ since the angular flux solution for the other three spatial nodes at each interface are simply reflections of each other. We

also show only the angular flux solution for the positive μ directions, since particles travel only from left to right across each of the interfaces.

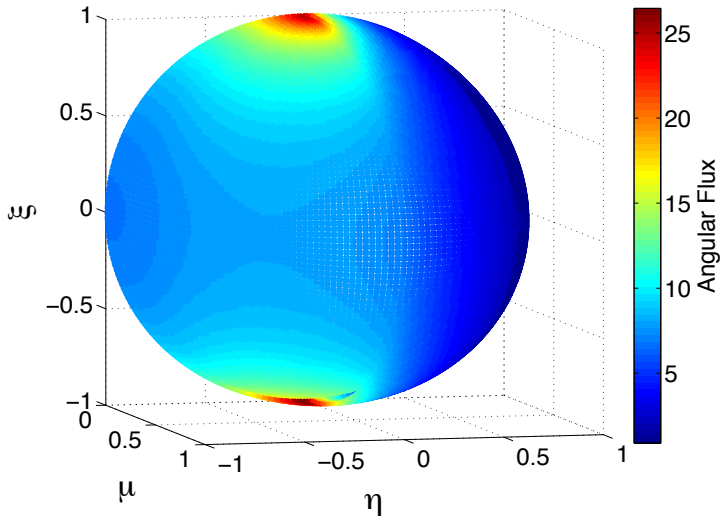

Figure 6.40: Reference angular flux solution at the left quadrature region interface for the three-region problem. The position and color of the points indicate quadrature direction and angular flux solution magnitude, respectively. Results are shown only at (1 cm, 0 cm, 0 cm) since the results in the other three spatial nodes at this interface are simply reflections of each other.

Figs. 6.43 to 6.45 plot the quadrature direction distribution for the positive μ octants for each quadrature region as we vary ϵ_{oc}, and Table 6.10 summarizes the direction counts. Figs. 6.40 shows the reference angular flux solution at the left quadrature region interface is relatively smooth. Therefore, the adaptive algorithm does not require the angular quadrature in the left quadrature region to undergo significant local refinement (except for $\epsilon_{oc} = 0.01$ where the tolerance is sufficiently low) as shown in Fig. 6.43. Figs. 6.41 and 6.42 show both the reference angular flux solution at the right quadrature region interface and the right boundary of the problem domain are nearly discontinuous near $\mu = 1$. Therefore, the adaptive

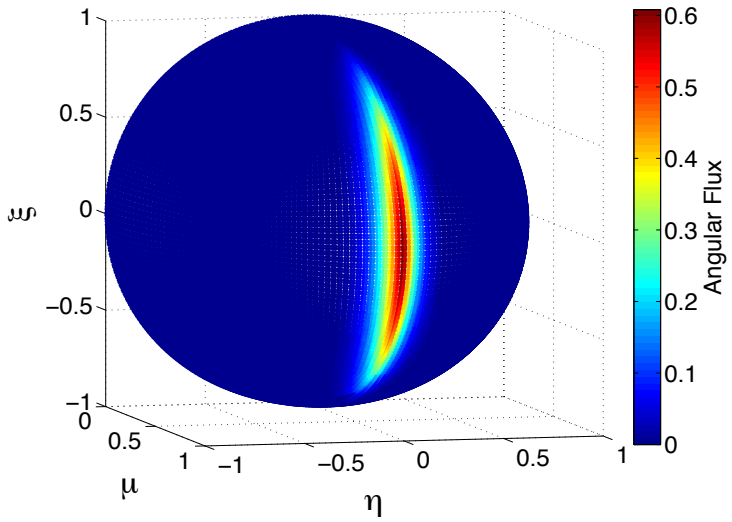

Figure 6.41: Reference angular flux solution at the right quadrature region interface for the three-region problem. The position and color of the points indicate quadrature direction and angular flux solution magnitude, respectively. Results are shown only at (9 cm, 0 cm, 0 cm) since the results in the other three spatial nodes at this interface are simply reflections of each other.

algorithm requires the SQs near $\mu = 1$ for both the angular quadratures in the center and right quadrature regions to undergo significant local refinement as shown in Figs. 6.44 and 6.45.

Figs. 6.46 to 6.49 show the incoming and mapped angular flux solutions across the left and right quadrature region interfaces, respectively, as we vary ϵ_{oc}. The mapped angular flux solutions are generated by using the new mapping algorithm without fix-up. We note that the mapped angular flux solution across each quadrature region interface preserves the 0th and 1st angular moments to machine precision. However, over- and under-shoots (including negativites) appear in the mapped solution across the left quadrature region interface near $\mu = 0$ as shown in Figs. 6.46 and 6.47 .

Fig. 6.50 plots the cell-average scalar flux as a function of angular mesh length for the spatial cell immediately after mapping across the right quadrature region inter-

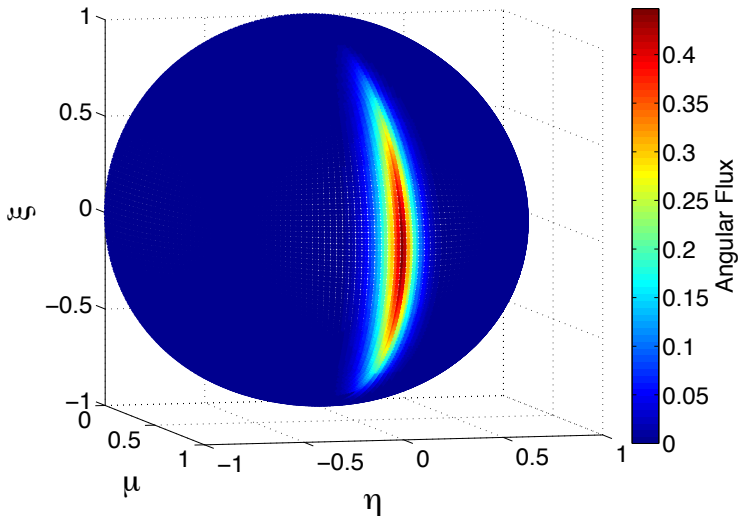

Figure 6.42: Reference angular flux solution at the right problem boundary for the three-region problem. The position and color of the points indicate quadrature direction and angular flux solution magnitude, respectively. Results are shown only at (10 cm, 0 cm, 0 cm) since the results in the other three spatial nodes at this interface are simply reflections of each other.

face. We note that the uniform angular quadrature results use the typical definition of h (Eqn. 6.1), whereas the locally-refined results use $h_{\text{cell-ave}}$ (Eqn. 6.10). Fig. 6.50 does not show improvement in scalar flux error convergence using the adaptive algorithm provided in Section 4.4. This can be understood by the following argument. Table 6.10 shows the number of directions in the left quadrature region is over a magnitude lower than that of the center quadrature region. Therefore, mapping across the left quadrature region interface requires recursively applying the mapping algorithm in order to map across multiple refinement levels for SQs near $\mu = 1$ as shown in Figs. 6.46 and 6.47. This introduces mapping errors that are propagated to the right quadrature region interface. Even though the mapping errors are minor at the left quadrature region interface, they become more important at the right quadrature region interface where the majority of the angular flux occurs near $\mu = 1$. This

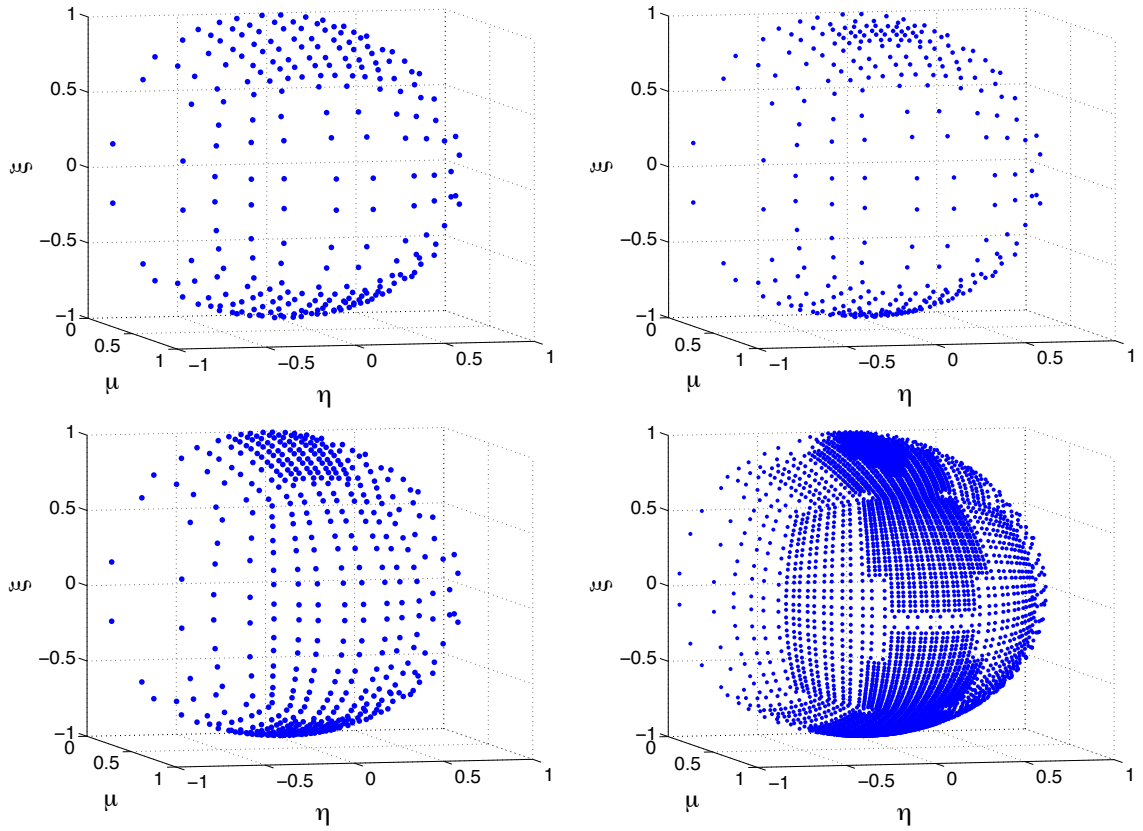

Figure 6.43: Quadrature direction distribution for the positive μ octants in the left quadrature region for $\epsilon_{oc} = 0.3$ (top left), $\epsilon_{oc} = 0.2$ (top right), $\epsilon_{oc} = 0.1$ (bottom left) and $\epsilon_{oc} = 0.01$ (bottom right).

results in an angular flux distribution which produces an incorrect scalar flux at the right quadrature region interface. We note that as the adaptive algorithm stands, there is no way for the left quadrature region to know that the right quadrature region requires the angular flux solution at $\mu = 1$ to be calculated with such precision. One possible way to circumvent this problem is to use "goal-oriented" testing that uses adjoint calculations to estimate where errors may arise in the solution, and thus where local angular refinement should occur. [28]

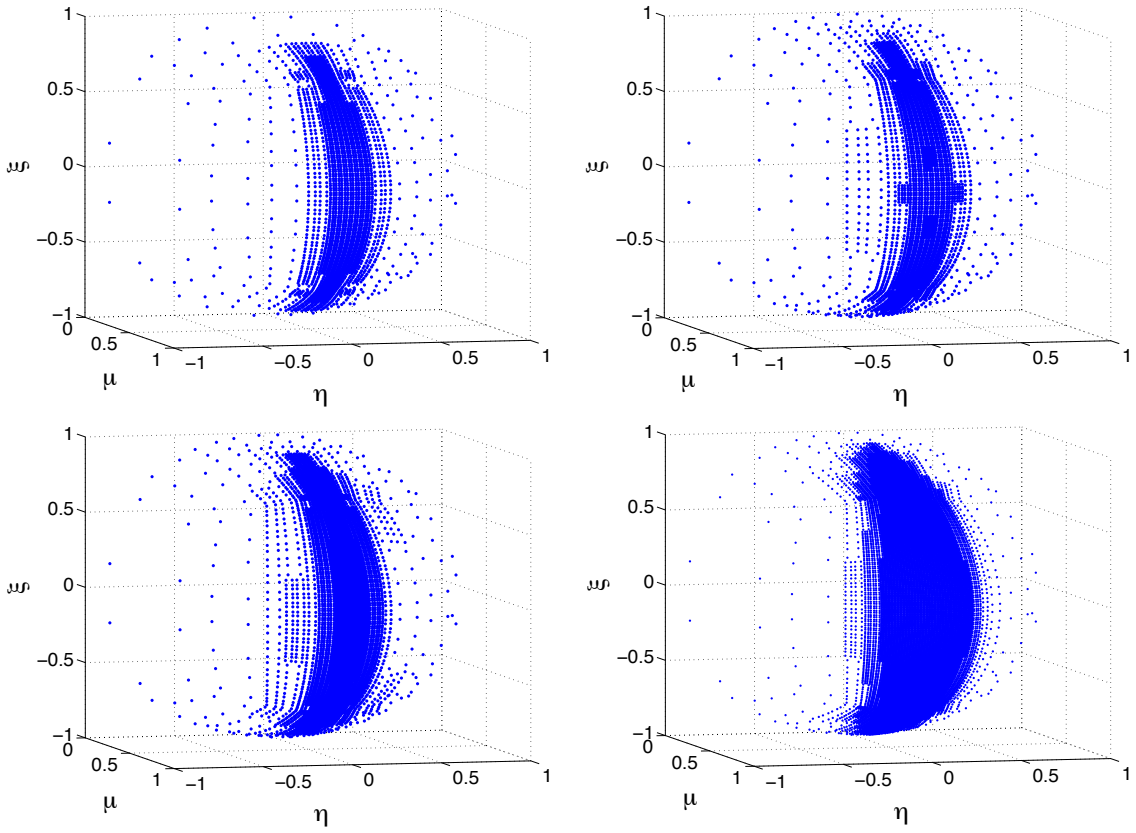

Figure 6.44: Quadrature direction distribution for the positive μ octants in the center quadrature region for $\epsilon_{oc} = 0.3$ (top left), $\epsilon_{oc} = 0.2$ (top right), $\epsilon_{oc} = 0.1$ (bottom left) and $\epsilon_{oc} = 0.01$ (bottom right).

Table 6.4: LDFE-SQ spherical harmonic function mapping results

Function	Mapping	Fix-up	ϵ_0	ϵ_μ	ϵ_η	ϵ_ξ	Error Range
Linear	Coarse-to-fine	No[a]	MP[b]	MP	MP	MP	(-4.2E-3, 4.6E-3)
Linear	Fine-to-coarse	No	MP	MP	MP	MP	(-9.2E-2, 9.3E-2)
Linear	Fine-to-coarse	Yes	MP	3.9E-9	3.9E-9	3.9E-9	(-5.6E-2, 5.7E-2)
5th-degree	Coarse-to-fine	No	MP	MP	MP	MP	(-1.2E-2, 9.8E-3)
5th-degree	Coarse-to-fine	Yes	MP	2.6E-6	2.6E-6	2.6E-6	(-1.2E-2, 9.8E-3)
5th-degree	Fine-to-coarse	No	MP	MP	MP	MP	(-2.9E-1, 2.9E-1)
5th-degree	Fine-to-coarse	Yes	MP	1.2E-7	1.2E-7	1.2E-7	(-4.4E-2, 4.3E-2)
Discontinuous	Coarse-to-fine	No	MP	MP	MP	MP	(-1.0E0, 1.0E0)
Discontinuous	Coarse-to-fine	Yes	MP	3.2E-3	3.1E-3	6.4E-4	(-1.0E0, 1.0E0)
Discontinuous	Fine-to-coarse	No	MP	MP	MP	MP	(-8.9E-1, 9.6E-1)
Discontinuous	Fine-to-coarse	Yes	MP	4.0E-4	4.0E-4	1.5E-4	(-5.0E-1, 5.5E-1)

[a] Fix-up not required
[b] Machine precision $\leq$ 1.0E-12

Table 6.5: QDFE-SQ spherical harmonic function mapping results

Function	Mapping	Fix-up	ϵ_0	ϵ_μ	ϵ_η	ϵ_ξ
Linear	Coarse-to-fine	No	MP[c]	MP	MP	MP
Linear	Coarse-to-fine	Yes	MP	2.5E-8	3.0E-8	3.0E-8
Linear	Fine-to-coarse	No	MP	MP	MP	MP
Linear	Fine-to-coarse	Yes	MP	1.6E-9	1.6E-9	6.4E-9
5th-degree	Coarse-to-fine	No	MP	MP	MP	MP
5th-degree	Coarse-to-fine	Yes	MP	3.9E-7	4.7E-7	3.2E-7
5th-degree	Fine-to-coarse	No	MP	MP	MP	MP
5th-degree	Fine-to-coarse	Yes	MP	4.2E-9	9.5E-9	4.2E-9
Discontinuous	Coarse-to-fine	No	MP	MP	MP	MP
Discontinuous	Coarse-to-fine	Yes	MP	1.3E-3	1.3E-3	7.4E-4
Discontinuous	Fine-to-coarse	No	MP	MP	MP	MP
Discontinuous	Fine-to-coarse	Yes	MP	2.1E-6	2.7E-4	5.1E-5

[a] Machine precision $\leq$ 1.0E-12

Table 6.6: QDFE-SQ spherical harmonic function mapping results (cont.)

Function	Mapping	Fix-up	$\epsilon_{\mu\eta}$	$\epsilon_{\mu\xi}$	$\epsilon_{\eta\xi}$	ϵ_{ξ^2}	$\epsilon_{\mu^2-\eta^2}$	Error Range
Linear	Coarse-to-fine	No	MP[a]	MP	MP	MP	MP	(-8.2E-3, 1.4E-2)
Linear	Coarse-to-fine	Yes	1.1E-7	1.0E-7	1.2E-7	MP	MP	(-8.2E-3, 1.4E-2)
Linear	Fine-to-coarse	No	MP	MP	MP	MP	MP	(-2.6E-3, 3.5E-3)
Linear	Fine-to-coarse	Yes	9.7E-9	2.4E-8	2.4E-8	6.2E-9	MP	(-2.6E-3, 3.5E-2)
5th-degree	Coarse-to-fine	No	MP	MP	MP	MP	MP	(-3.2E-2, 1.8E-2)
5th-degree	Coarse-to-fine	Yes	1.2E-6	8.8E-7	1.1E-6	1.3E-8	MP	(-3.2E-2, 1.8E-2)
5th-degree	Fine-to-coarse	No	MP	MP	MP	MP	MP	(-5.7E-3, 6.7E-3)
5th-degree	Fine-to-coarse	Yes	2.0E-8	4.5E-8	2.0E-8	2.5E-8	MP	(-5.7E-3, 6.7E-3)
Discontinuous	Coarse-to-fine	No	MP	MP	MP	MP	MP	(-1.0E0, 1.0E0)
Discontinuous	Coarse-to-fine	Yes	4.3E-3	2.9E-3	2.9E-3	3.6E-4	MP	(-1.0E0, 1.0E0)
Discontinuous	Fine-to-coarse	No	MP	MP	MP	MP	MP	(-5.3E-1, 5.7E-1)
Discontinuous	Fine-to-coarse	Yes	2.6E-5	1.1E-4	1.2E-4	4.1E-5	MP	(-5.7E-1, 6.9E-1)

[a] Machine precision $\leq$ 1.0E-12

Table 6.7: Number of directions per octant in each quadrature region for the uniform three-cell problem.

Run	Left	Center	Right
1	96	384	1536
2	384	1536	6144
3	1536	6144	24576
4	6144	24576	98304

Table 6.8: Moment preservation error and mapped angular flux solution range for the uniform three-cell problem using the new mapping algorithm without fix-up.

Run	ϵ_0	ϵ_μ	ϵ_η	ϵ_ξ	$\Psi_{\min}$	$\Psi_{\max}$
1	MP	MP	MP	MP	-5.77E-2[a]	2.98E-1
2	MP	MP	MP	MP	-3.81E-2[a]	5.09E-1
3	MP	MP	MP	MP	-8.65E-3[a]	5.92E-1
4	MP	MP	MP	MP	-8.18E-4[a]	6.12E-1[a]

[a] Does not satisfy the prescribed limits

Table 6.9: Moment preservation error and mapped angular flux solution range for the uniform three-cell problem using the new mapping algorithm with fix-up.

Run	ϵ_0	ϵ_μ	ϵ_η	ϵ_ξ	$\Psi_{\min}$	$\Psi_{\max}$
1	MP	3.97E-3	9.70E-3	1.66E-3	0.00E0	2.98E-1
2	MP	3.40E-4	4.61E-3	2.84E-4	0.00E0	5.09E-1
3	MP	5.43E-6	1.64E-4	1.01E-6	0.00E0	5.92E-1
4	MP	1.27E-7	2.02E-5	7.18E-8	0.00E0	6.08E-1

Table 6.10: Total number of directions in the positive μ octants in each quadrature region for the locally-refined three-cell problem.

Run	ϵ_{pw}	ϵ_{oc}	Left	Center	Right
1	0.00	0.30	240	3048	2952
2	0.00	0.20	288	4020	3864
3	0.00	0.10	480	8508	8052
4	0.00	0.01	4848	25320	22824

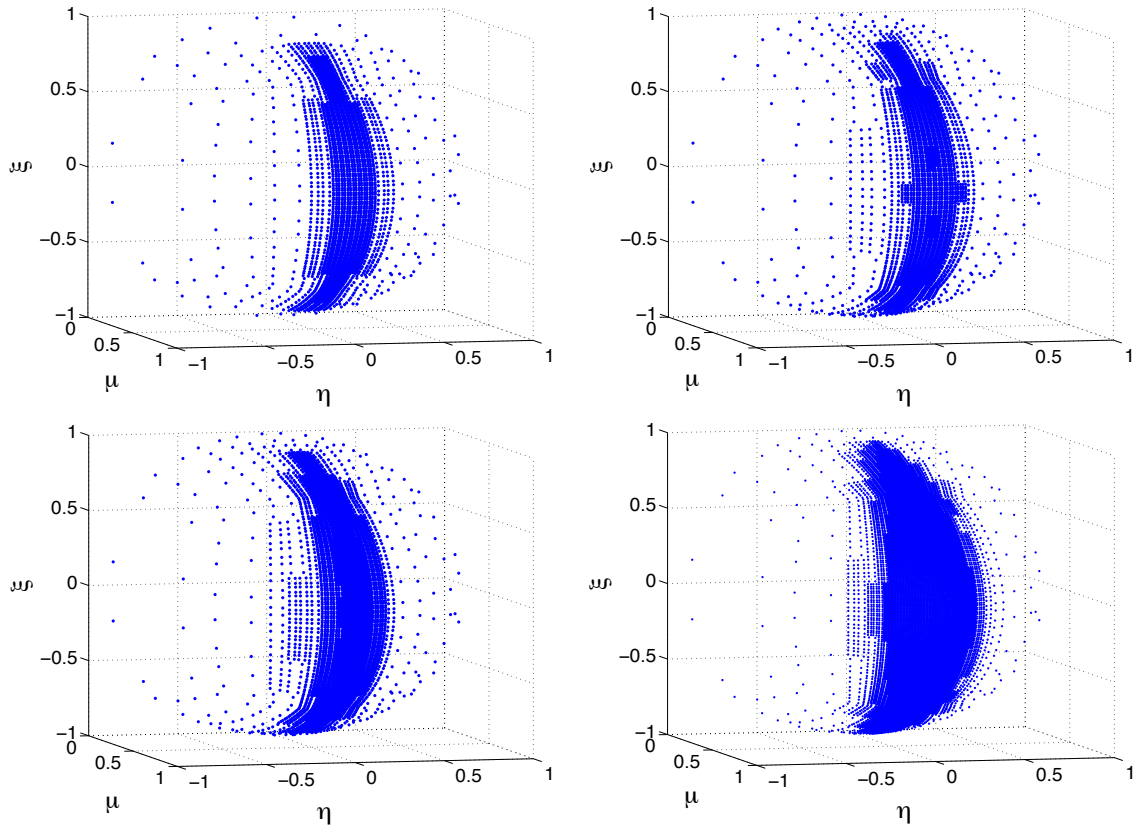

Figure 6.45: Quadrature direction distribution for the positive μ octants in the right quadrature region for $\epsilon_{oc} = 0.3$ (top left), $\epsilon_{oc} = 0.2$ (top right), $\epsilon_{oc} = 0.1$ (bottom left) and $\epsilon_{oc} = 0.01$ (bottom right).

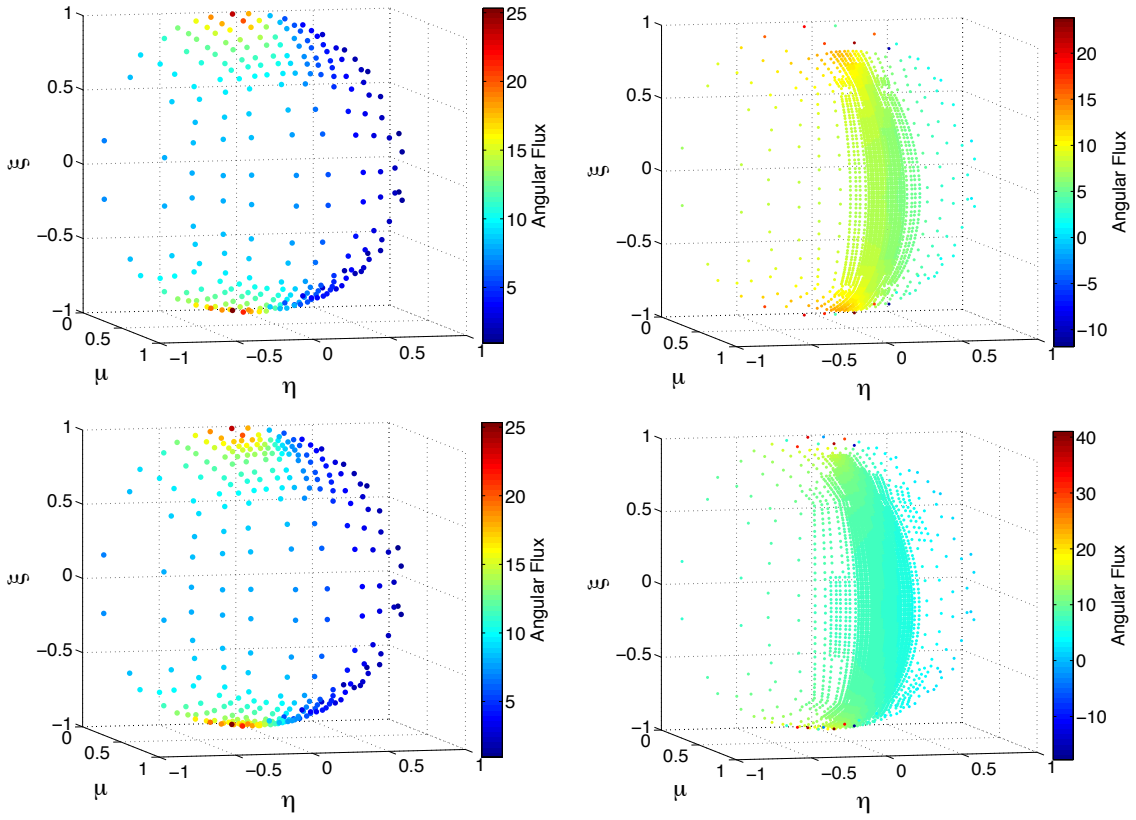

Figure 6.46: Incoming (left column) and mapped (right column) angular flux solutions across the left quadrature region interface for $\epsilon_{oc} = 0.3$ (top row) and $\epsilon_{oc} = 0.2$ (bottom row). Results are shown only at (1 cm, 0 cm, 0 cm) since the results in the other three spatial nodes at this interface are simply reflections of each other.

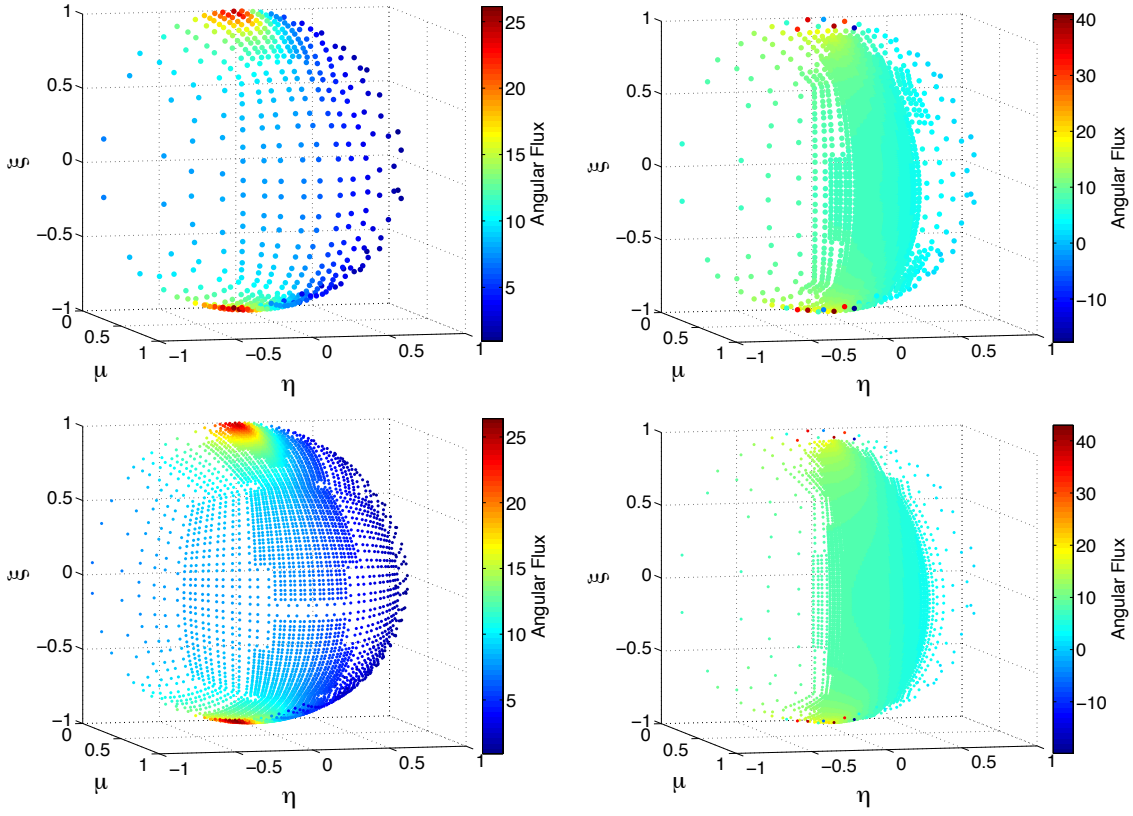

Figure 6.47: Incoming (left column) and mapped (right column) angular flux solutions across the left quadrature region interface for $\epsilon_{oc} = 0.1$ (top row) and $\epsilon_{oc} = 0.01$ (bottom row). Results are shown only at (1 cm, 0 cm, 0 cm) since the results in the other three spatial nodes at this interface are simply reflections of each other.

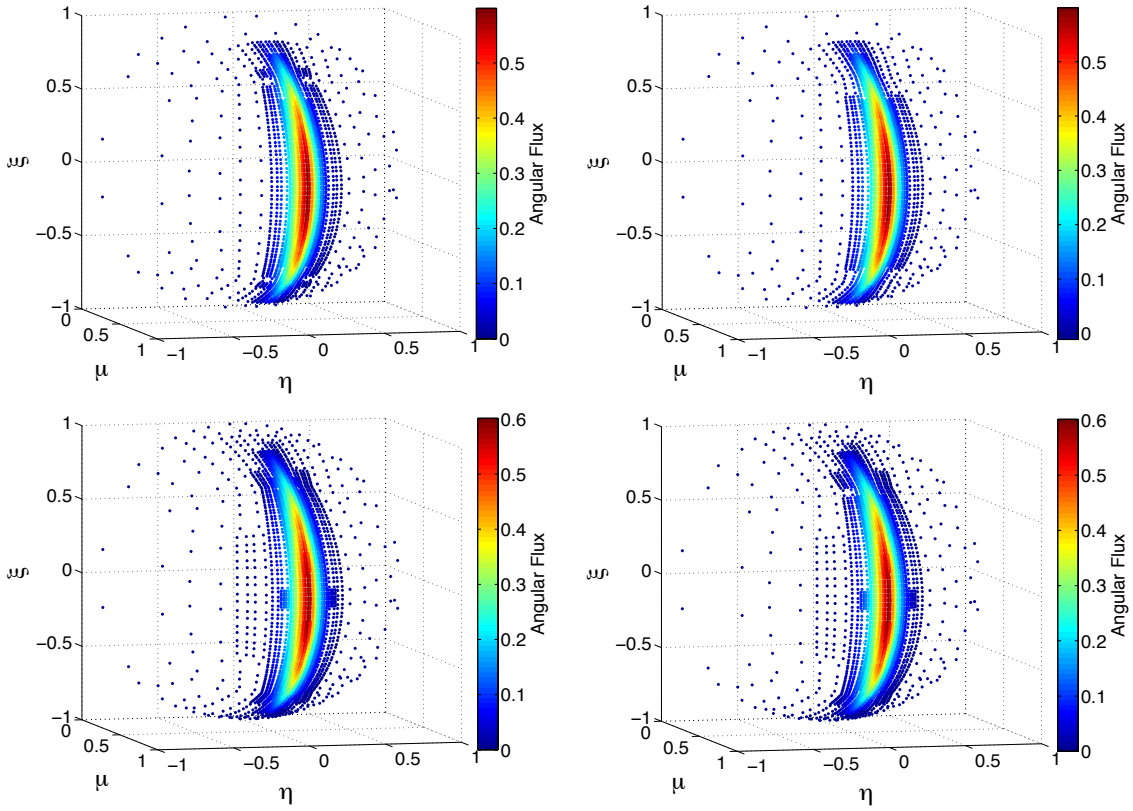

Figure 6.48: Incoming (left column) and mapped (right column) angular flux solutions across the right quadrature region interface for $\epsilon_{oc} = 0.3$ (top row) and $\epsilon_{oc} = 0.2$ (bottom row). Results are shown only at (9 cm, 0 cm, 0 cm) since the results in the other three spatial nodes at this interface are simply reflections of each other.

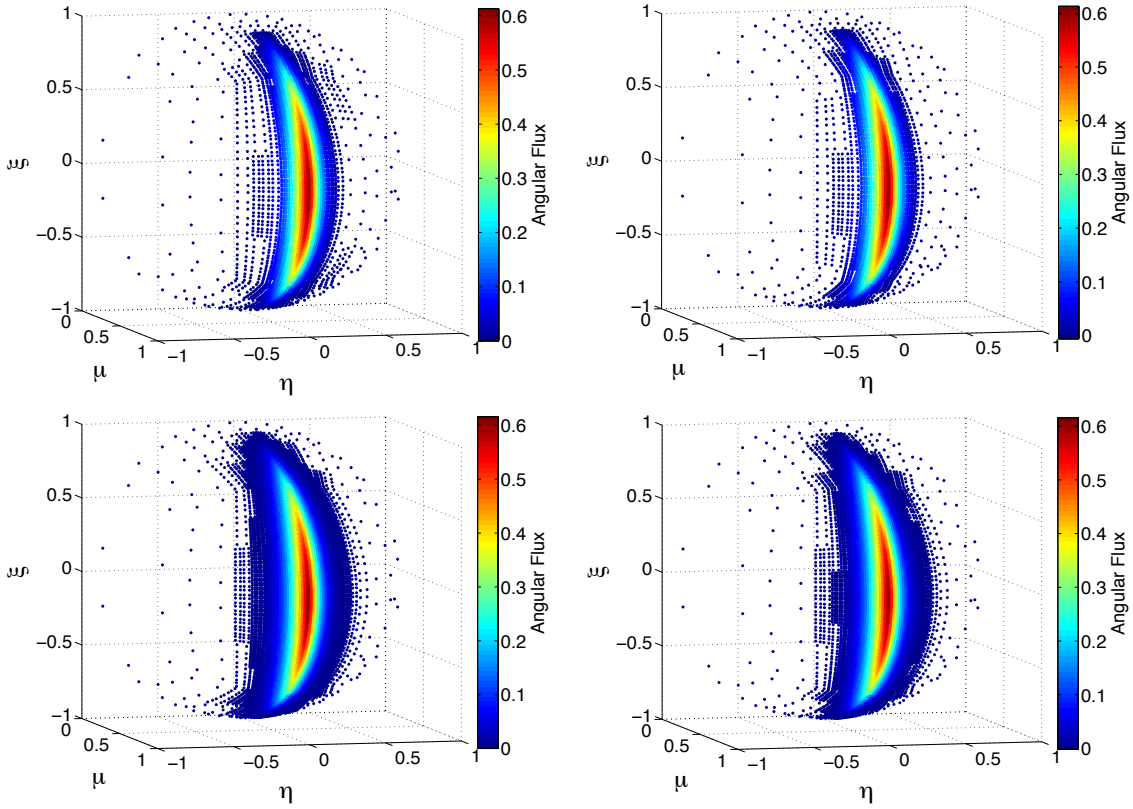

Figure 6.49: Incoming (left column) and mapped (right column) angular flux solutions across the right quadrature region interface for $\epsilon_{oc} = 0.1$ (top row) and $\epsilon_{oc} = 0.01$ (bottom row). Results are shown only at (9 cm, 0 cm, 0 cm) since the results in the other three spatial nodes at this interface are simply reflections of each other.

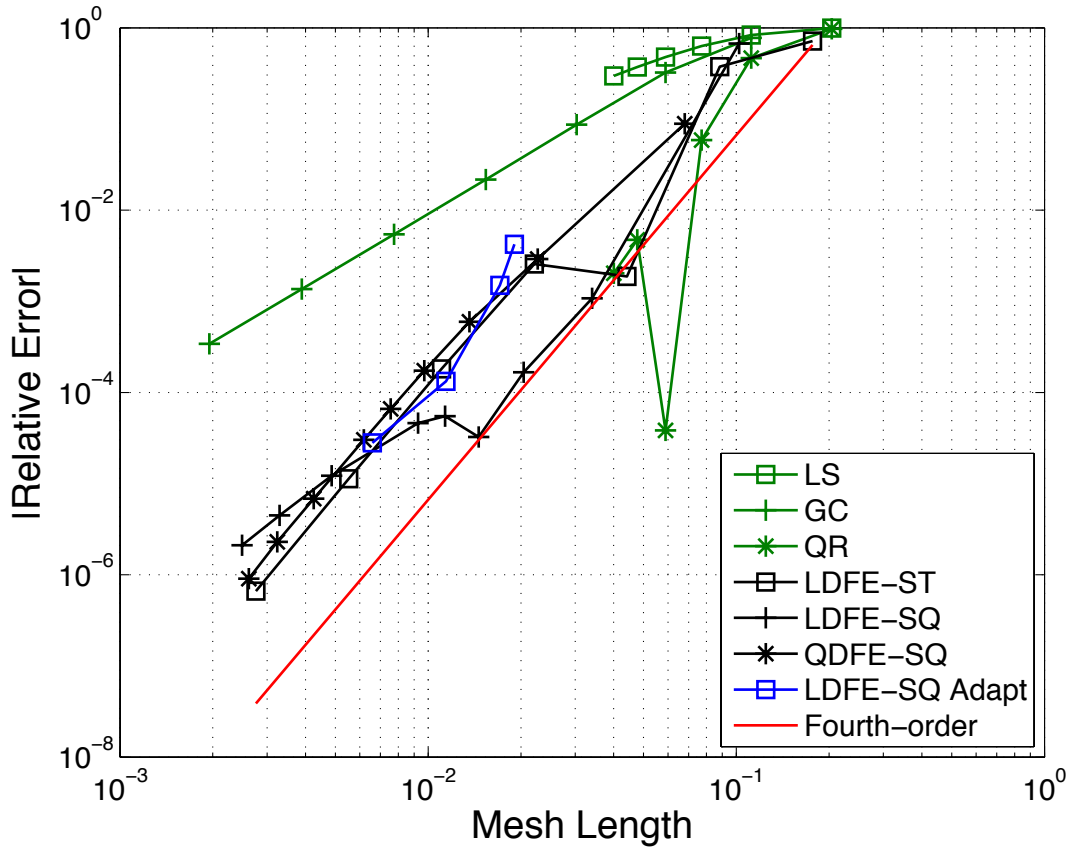

Figure 6.50: Scalar flux error in the first spatial cell after mapping across the right quadrature region interface as a function of angular mesh length for the locally-refined three-cell problem.

7. CONCLUSIONS AND FUTURE WORK

7.1 Conclusions

In this dissertation, we presented a new family of discrete-ordinates (S_n) angular quadratures based on discontinuous finite-elements (DFEM) in angle. The angular domain is divided into cones subtended by spherical quadrilaterals (SQs) on the surface of the unit sphere. Linear and quadratic discontinuous finite element (LDFE and QDFE) basis functions in the direction cosines are defined over each SQ, producing LDFE-SQ and QDFE-SQ angular quadratures, respectively. The directions and weights are chosen to exactly integrate the underlying basis functions. The new angular quadratures are an extension of the LDFE-ST angular quadratures developed by Jarrell and Adams, [2, 3] which define LDFE basis functions in angle over spherical triangles. The use of SQs, combined with our algorithm for defining SQ boundaries and the location of the quadrature directions in each SQ, produces more uniform direction and weight distributions, thereby reducing local integration errors. The QDFE-SQ angular quadrature demonstrates the use of higher-order DFEM basis functions within the DFEM-based angular quadrature methodology. The new angular quadratures are locally refinable, have strictly positive weights that correspond to a geometric tessellation of the unit sphere surface, and can be generated for large numbers of directions (sets with up to ≈800,000 directions over all octants have been generated). These properties make the new angular quadratures well-suited for adaptive S_n algorithms. A potential downside of the new angular quadratures is the inexact integration of spherical harmonics (SH) functions above linear for LDFE-SQ or quadratic for QDFE-SQ, which leads to particle-conservation errors for radiation transport problems with scattering order above 1st-order for LDFE-SQ or 2nd-order

for QDFE-SQ. However, computational results show that the new angular quadratures integrate high-degree SH functions with 4th-order accuracy (i.e., if the average SQ diameter decreases by a factor of 2, then the integration error decrease by a factor of $2^4 = 16$) given uniformly refined quadratures (no local refinement). For this reason, the particle-conservation errors from using the new angular quadratures for a radiation transport problem with anisotropic scattering must rapidly diminish with quadrature refinement, a characteristic observed in our computational results. In the limited testing to date, maximum cellwise conservation errors are orders of magnitude lower than the discretization errors in the quantities of interest (such as absorption rates) in the calculations. This result could be different for different quantities of interest in different problems, and may be different if locally refined quadratures are used. Overall, the computational results indicate that the performance of the new angular quadratures without local refinement is comparable to or better than that of traditional angular quadratures. Their performance can be further improved by using local refinement, which can significantly reduce the number of directions required to achieve a given accuracy, as computational results presented here have demonstrated for some problems.

Previous studies have shown that the effectiveness of DFEM-based angular quadratures in adaptive S_n algorithms was limited by the accuracy of the mapping algorithms required to pass the angular flux solution between spatial regions with different angular quadrature refinement. An "optimal" mapping algorithm should preserve both the shape and the angular moments of interest from the incoming angular flux solution. We have presented a new mapping algorithm which is nearly "optimal" for mapping sufficiently smooth solutions away from octant boundaries (small pointwise errors are introduced into the mapped solution even when the incoming solution lives in the underlying DFEM basis space, due to the perservation of the higher

angular moments). However, the mapped solution may contain over- and under-shoots (including negativities) when mapping near solution discontinuities or octant boundaries. To address these instances, we have developed and presented a fix-up algorithm, which uses multi-objective optimization (MOOP) to ensure the mapped solution satisfies a set of prescribed limits, and preserves the 0th angular moment to machine precision (MP). However, the fix-up algorithm introduces minor errors into the preservation of angular moments above 1st-order for LDFE-SQ or 2nd-order for QDFE-SQ.

The new angular quadratures, along with the new mapping and fix-up algorithms, provide the necessary tools for using DFEM-based angular quadratures in adaptive S_n algorithms. The next section discusses areas of potential future work including: (1) testing of various adaptive S_n strategies, and their efficient implementation on massively-parallel machines; (2) generalizing the new angular quadratures to arbitrary DFEM basis function order, which may lead to hp-adaptivity in angle; (3) theorizing the 4th-order error reduction shown by LDFE-SQ angular quadrature for integrating high-degree SH functions; (4) developing additional angular tessellation schemes by projecting other platonic solids onto the surface of the unit sphere; (5) applying the new angular quadratures to radiation transport problems in cylindrical geometry; (6) determining prescribed limits for the fix-up algorithm based on the discrete maximum principle applied to the linear Boltzmann transport equation; (7) improving the computational speed of the fix-up algorithm for use in larger S_n applications; (8) preserving the normal partial current instead of the 0th angular moment to MP in the fix-up algorithm; and (9) increasing weight distribution uniformity by allowing the SQ mesh lines on the surface of the inscribed cube to be skewed.

7.2 Future Work

7.2.1 Implementation and Testing of Adaptive S_n Algorithms

The goal of this research was to provide the necessary tools for effectively using DFEM-based angular quadratures within an adaptive S_n algorithm: (1) DFEM-based angular quadratures with improved properties; and (2) new mapping and fix-up algorithms for "optimally" passing the angular flux solution between spatial regions with different angular quadrature refinement. Future work should include testing of various adaptive S_n algorithms using the tools developed in this research. Of particular interest is the adaptive S_n algorithm provided by Jarrell and Adams, [2, 3] which suffered mainly from the lack of an accurate mapping algorithm. The research presented herein has demonstrated the use of a simplified version of their adaptive S_n algorithm (ignoring coarsening), which produced desirable results (e.g., locally-refining angular regions containing the largest angular flux variations, and preventing the over-refinement of angular regions with angular flux solution near zero). However, much more extensive testing is an important next step.

The use of adaptive S_n algorithms may lead to certain spatial regions having many more quadrature directions than others. If the problem domain is simply partitioned based on spatial decomposition, then the processors containing spatial regions with more quadrature directions will require additional computational effort. This poses a load-balancing issue, which negatively impacts parallel efficiency since the computational work is not evenly distributed among the processors. Future work should include the development and testing of a partitioning and/or solution algorithm that addresses this load-balancing issue.

7.2.2 hp-Adaptivity in Angle

hp-Adaptivity refers to an adaptive algorithm that can update both the mesh size, h (i.e., h-adaptivity) and the degree of the underlying basis function, p (i.e., p-adaptivity). Previous studies have shown that hp-adaptivity can lead to exponential error convergence, as opposed to converging at a polynomial rate as demonstrated by h-adaptivity with a constant p.[29] The adaptive S_n algorithm provided by Jarrell and Adams may be classified as an h-adaptive method since it changes only the angular partition (i.e., width of some SQs on the surface of the unit sphere). Their adaptive S_n algorithm could be extended to an hp-adaptive method by adjusting both the angular partitioning and the order of the underlying DFEM basis functions. Future work should include: (1) generalization of the new angular quadratures to higher-order (above quadratic) DFEM basis functions, and (2) development of hp-adaptive S_n algorithm rules.

7.2.3 Theoretical Study of 4th-Order Convergence

The computational results in this study showed LDFE-SQ angular quadratures are capable of integrating high-degree (above linear) SH functions with 4th-order accuracy (i.e., reducing the average SQ width by a factor of 2, reduces the integration error by a factor of $2^4 = 16$). Jarrell and Adams observed the same rapid convergence with LDFE-ST angular quadratures. From approximation theory, collocation onto piecewise linear functions would be expected to produce results that are at most 2nd-order accurate. Therefore, the LDFE-SQ angular quadratures may be classified as super-convergent. Future work should attempt a theoretical understanding of this phenomenon.

7.2.4 Alternative Tessellation Schemes

Both the new (LDFE-SQ and QDFE-SQ) and previous (LDFE-ST) DFEM-based angular quadratures project platonic solids (i.e., a cube and an octahedron, respectively) onto the surface of the unit sphere. There are five platonic solids: tetahedron (four faces), cube (six faces), octahedron (eight faces), dodecahedron (12 faces), and icosahedron (20 faces). Platonic solids share the following characteristics: (1) all vertices lie on a sphere, (2) angles formed between any two faces are equal, (3) all faces are polyhedral, (4) all solid angles subtended by each face are equal, and (5) all vertices are surrounded by the same number of faces.[30] The most interesting of the three remaining platonic solids is the icosahedron, which most closely resembles a sphere, thereby possibly producing more uniform direction distributions. In addition, the 20 triangular faces can be divided into 60 quadrilaterals, each with the same subtended solid angle. This suggests the possibility of even more uniform quadrature direction and weight distributions than were achieved in the present work, which could further reduce local integration errors.

7.2.5 Extension to S_n Problems in Cylindrical Geometry

The main difference between cartesian and cylindrical geometry for S_n radiation transport is the derivative term with respect to the azimuthal angle in cylinders. Traditionally, the angular derivative term is discretized using a weighted differencing scheme [1] that assumes quadrature directions lying along constant polar levels (fixed Ω_z), solved in an ordered manner (i.e., from azimuthal angle $\gamma = \pi$ to $\gamma = 0$). The new LDFE-SQ and QDFE-SQ (and the previous LDFE-ST) angular quadratures do not force sets of directions to lie on discrete polar levels, and thus cannot be used in existing cylindrical-geometry S_n codes. Instead, we suggest two potential methods for using DFEM-based angular quadratures for S_n radiation transport in cylindrical ge-

ometry: (1) development of a product angular quadrature using 1D Gauss-Legendre (GL) quadrature for the polar angular domain and 1D DFEM-based angular quadrature for the azimuthal angular domain; and (2) development of a DFEM-consistent discretization method for the angular derivative term, which allows the use of the new LDFE-SQ and QDFE-SQ angular quadratures in cylindrical geometry by sweeping through the angular domain one SQ at a time, from the most inward-directed to the most outward-directed. This would resemble the familiar cell-by-cell "sweep" in the spatial domain that is the basis for many S_n iterative sweeps.

The first method discretizes the polar angular domain using 1D GL quadrature, and the azimuthal angular domain using 1D DFEM-based angular quadrature. For each discrete polar level, we partition the azimuthal angular domain into a set of non-overlapping angular bins $\Delta\gamma_i, i = 1 : I$. We define 1D DFEM basis functions in angle $b_{ij}(\gamma), j = 1 : J$ over each $\Delta\gamma_i$ where J is the number of degrees of freedom. For example, 1D LDFE basis functions have two degrees of freedom, and are linear in the directional cosine:

$$b_{ij}(\gamma) = c_j + c_{\mu,j}\mu \ , \ \ j = 1 : 2, \tag{7.1}$$

where $\mu = cos(\gamma)$. We note that Stone [4] investigated DFEM-based angular quadratures for 2D Cartesian geometry where the basis functions are linear in both $\mu = \cos(\gamma)$ and $\eta = \sin(\gamma)$. Cylindrical geometry does not require basis functions that are linear in both μ and η since by reflective symmetry $\psi(\gamma) = \psi(-\gamma)$ (i.e., ψ is an even function of γ, and thus the sine term is zero). The b_{ij} unknowns (i.e., the c-coefficients in Eqn. 7.1) are determined by requiring b_{ij} to be cardinal functions at J selected quadrature directions. For example, using 1D LDFE basis functions requires solving the following linear system to determine the c-coefficients for each

angular bin:

$$\begin{bmatrix} 1 & \mu_1 \\ 1 & \mu_2 \end{bmatrix} \begin{bmatrix} c_1 & c_2 \\ c_{\mu,1} & c_{\mu,2} \end{bmatrix} = \begin{bmatrix} 1 & 0 \\ 0 & 1 \end{bmatrix} . \tag{7.2}$$

The weight of each quadrature is the integral of its associated basis function over its angular bin:

$$w_{ij} = \int_{\Delta\gamma_i} d\gamma b_{ij}(\gamma) . \tag{7.3}$$

The set of J directions and weights forms the 1D DFEM angular quadrature for $\Delta\gamma_i$.

The traditional weighted differencing scheme for the angular derivative term can be used with the GL-DFEM angular quadrature. Alternatively, a DFEM-consistent discretization scheme for the angular derivative term can be obtained by (1) expanding the angular flux solution in each angular bin using its underlying DFEM basis functions, and (2) taking up to the N-th (where N is the DFEM basis function order) azimuthal moment of the linear Boltzmann transport equation (LBE) in cylindrical geometry over each angular bin. This results in $N+1$ moment equations, and $N+3$ unknowns for each angular bin. The unknowns in each angular bin are the angular flux solutions at $N+1$ quadrature directions, and the angular flux solutions at the angular bin edges. The system is closed by recognizing the angular flux solution at the incoming edge is known from the upstream angular bin (or the starting direction at $\gamma = \pi$), and the solution at the outgoing edge can be approximated by evaluating the underlying DFEM basis functions. Therefore, each angular bin requires an $(N+1) \times (N+1)$ linear solve to obtain the angular flux solutions at the quadrature directions.

The second method extends the DFEM-consistent discretization scheme to the new LDFE-SQ and QDFE-SQ angular quadratures. The new angular quadratures distribute directions uniformly rather than concentrating them by polar level. In-

stead of solving the angular flux solution along constant polar levels, we may sweep through the angular domain one SQ at a time, from the most inward-directed to the most outward-directed by (1) expanding the angular flux in each SQ using the underlying DFEM basis functions in angle, and (2) taking up to the N-th (where N is the DFEM basis function order) moment of the LBE in cylindrical geometry over each SQ. This results in $(N+1)^2$ moment equations, and $(N+1)^2+4$ unknowns for each SQ. The unknowns in each SQ are the angular flux solutions at $(N+1)^2$ quadrature directions, and the angular flux solutions at the SQ edges. The system is closed by recognizing the solution at the incoming edge is known from the upstream SQ, and the solution at the outgoing edges may be found by interpolating the underlying DFEM basis functions. Therefore, each SQ requires an $(N+1)^2 \times (N+1)^2$ linear solve to obtain the angular flux solutions at the quadrature directions.

7.2.6 Fix-Up Limits Based on Discrete Maximum Principle

As discussed in Section 5.2, the fix-up algorithm is applied if the mapped solution does not satisfy a set of prescribed limits. In this dissertation, the prescribed limits were based on either analytic or empirical solutions. Neither of those methods may be possible or feasible for real-world applications. Ideally, the prescribed limits would come from the maximum principle, which states the solution for a given partial differential equation with set boundary and initial conditions must satisfy certain bounds. The bounds on the analytic LBE solution on a given spaital cell with a given source are known and simple. However, spatial discretization schemes violate these bounds, introducing unphysical extrema. Future work could develop a *discrete* version of a maximum principle for spatial discretization schemes of interest in order to obtain prescribed limits for the fix-up algorithm. We note that the fix-up algorithm should not try to cancel out other discretization errors, such as those introduced by

spatial discretization. For example, if the spatial discretization produces a negative solution at the quadrature region interface, then the discrete maximum principle that we envision should be allowed to assign a negative lower bound.

7.2.7 Increase Speed and Accuracy of Fix-Up Algorithm

The fix-up algorithm in this dissertation used the revised Simplex method for solving the required multi-objective optimization problem (MOOP). As discussed in Section 5.2, the revised Simplex method was chosen as a proof-of-concept due to its robustness and simplicity in implementation. As discussed in Appendix B, there are many other types of linear programs including other variants of the Simplex method that are designed to increase the speed and accuracy of the Simplex method, particularly for larger problems. Future work should optimize the speed and accuracy of the fix-up algorithm by testing different linear programs, particularly if higher-order (above quadratic) DFEM basis functions are used.

7.2.8 Preservation of Normal Partial Current in Fix-Up Algorithm

As discussed in Section 5.2, the fix-up algorithm imposed an equality constraint to preserve the 0th angular moment (i.e., scalar flux) of the incoming angular flux solution. However, the scalar flux has no physical significance when mapping across a spatial interface. Instead, future work should investigate the preservation of the normal partial current to MP:

$$\vec{J} = \sum_{m=1}^{N_{\text{map}}} \left(\vec{\Omega}_m \cdot \vec{n} \right) w_m \psi_m \ , \tag{7.4}$$

where $\vec{n}$ is the outward unit normal vector of the spatial interface. The preservation of the normal partial current ensures particle balance when mapping across a spatial interface using the fix-up algorithm.

7.2.9 Exact QDFE-SQ Mapping of Linear Functions

As discussed in Section 6.2.1, simple interpolation of the QDFE basis functions for mapping linear SH functions should produce mapped solutions that have no error relative to the analytic solution, since the linear SH functions live in the basis space for both the coarse and fine QDFE-SQ angular quadratures. The mapped solution should also exactly integrate the 0th and 1st angular moments, which only require the integration of up to 2nd-degree SH functions (shown to be exact in Section 6.1.1). Errors in the mapped solution relative to the analytic solution are introduced by the requirement of the QDFE-SQ mapping to exactly preserve the 2nd angular moments, which requires integration of up to 3rd-degree SH functions. Future work should modify the QDFE-SQ mapping algorithm such that no errors are introduced into the mapping of linear SH functions.

7.2.10 Increase Weight Distribution Uniformity Using Skewed Mesh Lines

As discussed in Section 4.1.5, SQs are projected from divisions on the cube face that are required to be either horizontal or vertical. Fig. 7.1 shows the SQs resulting from evenly placing the divisions on each cube face, which shows the projected SQs are smaller near the center of the octant even though the surface area of the quadrilaterals on the cube face are equal. Fig. 7.2 shows the SQs resulting from using the division placement strategy provided in Section 4.1.5, which ensures the total surface area of all the SQs belonging to the same "ring" (see Section 4.1.5 for details) are equal to what it should be in a perfectly uniform SQ surface area distribution. The results show the SQs have a more uniform surface area distribution than in Fig. 7.1, but are still not perfectly uniform since SQs within the same ring do not necessarily have equal surface areas. One possible way to achieve a even more uniform SQ surface area distribution would be to allow the divisions on the cube

face to skew. This additional degree of freedom would allow quadrilaterals on the cube face closer to the center of the octant to be made larger in order to offset the inherent decrease in surface area of the projected SQ.

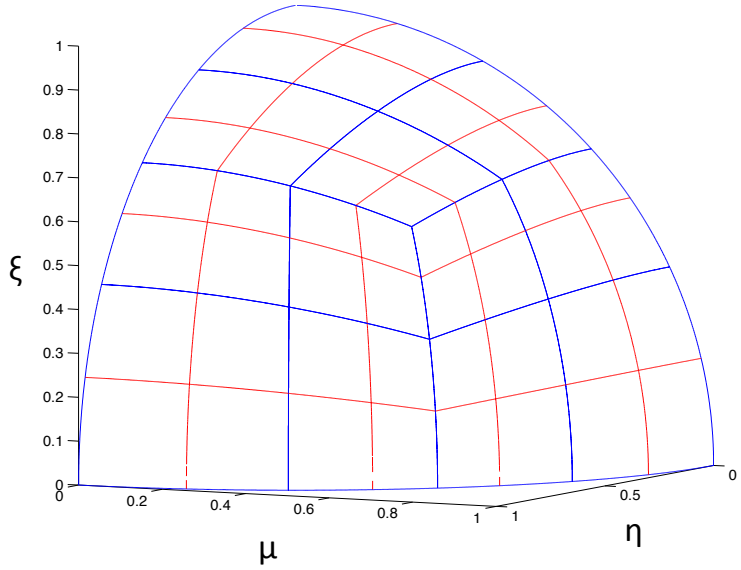

Figure 7.1: Spherical quadrilaterals using even division placement on the cube face. Blue and red lines indicate spherical quadrilaterals projected from sub-square and sub-sub-square divisions, respectively.

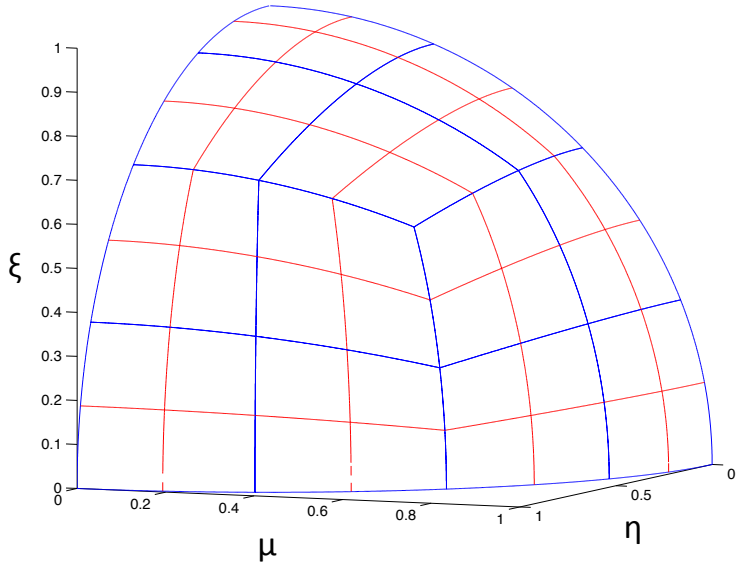

Figure 7.2: Spherical quadrilaterals using the division placement strategy from Section 4.1.5. Blue and red lines indicate spherical quadrilaterals projected from sub-square and sub-sub-square divisions, respectively.

REFERENCES

[1] Lewis, E.E., Miller, W.F., Computational Methods of Neutron Transport, John Wiley and Sons, New York, 1984.

[2] Jarrell, J.J., An Adaptive Angular Discretization Method for Neutral-Particle Transport in Three-Dimensional Geometries, PhD Dissertation, Texas A&M University, College Station, TX, 2010.

[3] Jarrell, J.J., Adams, M.L., Discrete-Ordinates Quadrature Sets Based on Linear Discontinuous Finite Elements, *International Conference on Mathematics and Computational Methods Applied to Nuclear Science and Engineering (M&C 2011)*, Rio de Janeiro, Brazil, May 8-12, 2011.

[4] Stone, J.C., Adaptive Discrete-Ordinates Algorithms and Strategies, PhD Dissertation, Texas A&M University, College Station, TX, 2007.

[5] Adams, M.L., Discontinuous Finite Element Transport Solutions in Thick Diffusive Problems, *Nuclear Science and Engineering*, Vol. 137, pp 298-333, 2001.

[6] Adams, M.L., Larsen, E.W., Fast Iterative Methods for Discrete-Ordinates Particle Transport Calculations, *Progress in Nuclear Energy*, Vol. 40, pp 3-159, 2002.

[7] Abu-Shumays, I.K., Compatible Product Angular Quadrature for Neutron Transport in X-Y Geometry, *Nuclear Science and Engineering*, Vol. 64, pp 299-316, 1977.

[8] Abu-Shumays, I.K., Angular Quadratures for Improved Transport Calculations, *Transport Theory and Statistical Physics*, Vol. 30, No. 2, pp 169-204, 2001.

[9] Stroud, A., Secrest, D., Gaussian Quadrature Formulas, Prentice-Hall, Englewood Cliffs, NJ, 1966.

[10] Spence, P.J., The Generation of Arbitrary Order, Non-Classical, Gauss-Type Quadrature for Transport Applications, *Journal of Computational Physics*, Vol. 296, pp 25-57, 2015.

[11] Ahrens, C., and Beylkin, G., Rotationally Invariant Quadratures for the Sphere, *Proc. R. Soc. A*, Vol. 465, pp 3103-3125, 2009.

[12] Brown, P., Chang, B., and Clouse, C. Locally Refined Quadrature Rules for S_N Transport, Lawrence Livermore Laboratory, Tech. Rep. UCRL-JRNL-220755, Livermore, CA, 2006.

[13] Fromowitz, D.B., and Zeigler, G.B., Development and Evaluation of High-Fidelity Product and Evenly-Spaced Angular Quadratures for Three-Dimensional Discrete Ordinates Calculations with Large Air Regions, *Nuclear Science and Engineering*, Vol. 182, pp 166-180, 2016.

[14] Nair, R.D., Thomas, S.J., Loft, R.D., A Discontinuous Galerkin Transport Scheme on the Cubed Sphere, *Monthly Weather Review*, Vol. 133, pp 814-828, 2005.

[15] Sobolev, S.L., Cubature Formulas on the Sphere Invariant Under Finite Groups of Rotations, *Doklady Akademii Nauk SSSR*, Vol. 146, pp 310-313, 1962.

[16] Diwekar, U.M., Introduction to Applied Optimization, Springer, New York, 2008.

[17] Morgan, S.S., A Comparison of Simplex Method Algorithms, MS Dissertation, University of Florida, Gainesville, FL, 1997.

[18] Darst, R.B., Introduction to Linear Programming: Applications and Extensions, Marcel Dekker Inc, New York, 1991.

[19] Press, W.H., Teukolsky S.A., Vetterling W.T., Flannery B.P., Numerical Recipes: The Art of Scientific Computing, Cambridge University Press, New York, 2007.

[20] Adams, M.P., Adams, M.L., Hawkins, W.D., Smith, T., Rauchwerger, L., Amato, N.M., Bailey, T.S., Falgout, R.D., Provably Optimal Parallel Transport Sweeps on Regular Grids, *International Conference on Mathematics and Computational Methods Applied to Nuclear Science and Engineering (M&C 2013)*, Sun Valley, ID, May 9-15, 2013.

[21] Hawkins, W.D., Smith, T., Adams, M.P., Rauchwerger, L., Amato, N.M., Adams, M.L., Efficient Massively Parallel Transport Sweeps, *Trans. Amer. Nucl. Soc.*, Vol. 107, pp 477-481, 2012.

[22] Buss, A., Harshvardhan, Papdopoulos, I., Pearce, O., Smith, T., Tanase, G., Thomas, N., Xu, X., Bianco, M., Amato, N.M., Rauchweger, L., STAPL: Standard Template Adaptive Parallel Library, *SYSTOR*, Haifa, Israel, June 4-6, 2010.

[23] Tanase, G., Buss, A., Fidel, A., Harshvardhan, Papadopoulos, I., Pearce, O., Smith, T., Thomas, N., Su, X., Mourad, N., Vu, J., Bianco, M., Amato, N.M., Rauchwerger, L., The STAPL Parallel Container Framework, *Proc. ACM SIGPLAN Symp. Prin. Prac. Par. Prog. (PPOPP)*, 2011.

[24] Stone H.G., Adams, M.L., A Piecewise Linear Finite Element Basis with Application to Particle Transport, *Proc. ANS Topical Meeting Nuclear Mathematical and Computational Sciences Meeting*, Gatlinburg, TN, April 6-11, 2003.

[25] Kobayashi K., Sugimura N., Nagaya Y., 3D Radiation Transport Benchmark Problems and Results for Simple Geometries with Void Regions, *Progress in Nuclear Energy*, Vol. 39, No. 2, pp 119-144, 2001.

[26] Chai, J., Lee, H., Patankar, S., Ray Effect and False Scattering in the Discrete Ordinates Method, *Numerical Heat Transfer, Part B: Fundamentals: An International Journal of Computation and Methodology*, Vol. 24, Issue 4, 1993.

[27] Coelho, P., The Role of Ray Effects and False Scattering on the Accuracy of the Standard and Modified Discrete Ordinates Method, *Journal of Quantitative Spectroscopy and Radiative Transfer*, Vol. 73, pp 231-238, 2002.

[28] Wang, Y., Adaptive Mesh Refinement Solution Techniques for the Multigroup SN Transport Equation Using a Higher-Order Discontinuous Finite Element Method, PhD Dissertation, Texas A&M University, 2009.

[29] Guo, X.Z., Babuska, I., The H-P Version of the Finite Element Method. Part 1: The Basic Approximation Results, *Computational Mechanics*, Vol. 1, pp 21-41, 1986.

[30] Weisstein, E.W., Platonic Solid, *MathWorld: A Wolfram Web Resource*. Retrieved May 15, 2016 from http://mathworld.wolfram.com/PlatonicSolid.html.

APPENDIX A

SPHERICAL QUADRILATERAL INTEGRATION MATHEMATICS

A.1 Background

As discussed in Section 3.2, quadrature weights are determined by integrating discontinuous finite element (DFEM) basis functions in the direction cosines over spherical quadrilaterals (SQs) on the surface of the unit sphere, which is difficult since the SQ boundaries are not constant. Therefore, we transform the basis functions from the surface of the unit sphere to the surface of the inscribed cube from which the SQs were projected. The integration of the basis functions over the cube face is simple since the boundaries are constant. In this appendix, we derive the Jacobian required to transform the basis functions from the surface of the unit sphere to the surface of the inscribed cube.

A.2 Relationships Between Unit Sphere and Cube Face

Fig. A.1 shows the $(\tilde{x}, \tilde{y})$ coordinates on the cube face perpendicular to the μ-axis. The vector from the unit sphere origin to any point in the $(\tilde{x}, \tilde{y})$ domain represents a unique direction $\vec{\Omega}$. From simple geometry, we can establish the following relationships between the polar and azimuthal angles (θ, γ), and the $(\tilde{x}, \tilde{y})$ coordinates:

$$\cos\gamma = \frac{a}{\sqrt{a^2 + \tilde{x}^2}} \,, \tag{A.1}$$

$$\sin\gamma = \frac{\tilde{x}}{\sqrt{a^2 + \tilde{x}^2}} \,, \tag{A.2}$$

$$\cos\theta = \frac{\tilde{y}}{\sqrt{a^2 + \tilde{x}^2 + \tilde{y}^2}} \,, \tag{A.3}$$

and

$$\sin\theta = \frac{\sqrt{a^2 + \tilde{x}^2}}{\sqrt{a^2 + \tilde{x}^2 + \tilde{y}^2}} \ , \tag{A.4}$$

where $a = 1/\sqrt{3}$ is the length of the inscribed cube in the first octant. Inserting Eqns. A.1 through A.4 into the following directional cosine identities:

$$\mu = \cos\gamma \sin\theta \ , \tag{A.5}$$

$$\eta = \sin\gamma \sin\theta \ , \tag{A.6}$$

and

$$\xi = \cos\theta \ , \tag{A.7}$$

results in

$$\mu = \frac{a}{r} \ , \tag{A.8}$$

$$\eta = \frac{\tilde{x}}{r} \ , \tag{A.9}$$

and

$$\xi = \frac{\tilde{y}}{r} \ , \tag{A.10}$$

where $r = \sqrt{a^2 + \tilde{x}^2 + \tilde{y}^2}$. Eqns. A.8 to A.10 are the relationships between the surface of the unit sphere and the surface of the inscribed cube.

A.3 Jacobian Derivation

The Jacobian required to transform the basis functions from the surface of the unit sphere to the $(\tilde{x}, \tilde{y})$ coordinates on the surface of the inscribed cube is

$$|J| = \begin{vmatrix} \frac{\partial\xi}{\partial\tilde{x}} & \frac{\partial\xi}{\partial\tilde{y}} \\ \frac{\partial\gamma}{\partial\tilde{x}} & \frac{\partial\gamma}{\partial\tilde{y}} \end{vmatrix} \ . \tag{A.11}$$

Eqns. A.1 and A.2 show

$$\frac{\partial \gamma}{\partial \tilde{y}} = 0 \; . \tag{A.12}$$

Therefore, Eqn. A.11 becomes

$$|J| = \left| \frac{\partial \gamma}{\partial \tilde{x}} \frac{\partial \xi}{\partial \tilde{y}} \right| \; . \tag{A.13}$$

We solve for $\partial\gamma/\partial\tilde{x}$ using Eqn. A.1 or A.2:

$$\frac{\partial \gamma}{\partial \tilde{x}} = \frac{a}{a^2 + \tilde{x}^2} \; . \tag{A.14}$$

We solve for $\partial\xi/\partial\tilde{y}$ using Eqn. A.3:

$$\frac{\partial \xi}{\partial \tilde{y}} = \frac{a^2 + \tilde{x}^2}{(a^2 + \tilde{x}^2 + \tilde{y}^2)^{3/2}} \; . \tag{A.15}$$

Inserting Eqns. A.14 and A.15 into A.13 results in

$$|J| = \frac{a}{r^3} \; , \tag{A.16}$$

where $r = \sqrt{a^2 + \tilde{x}^2 + \tilde{y}^2}$.

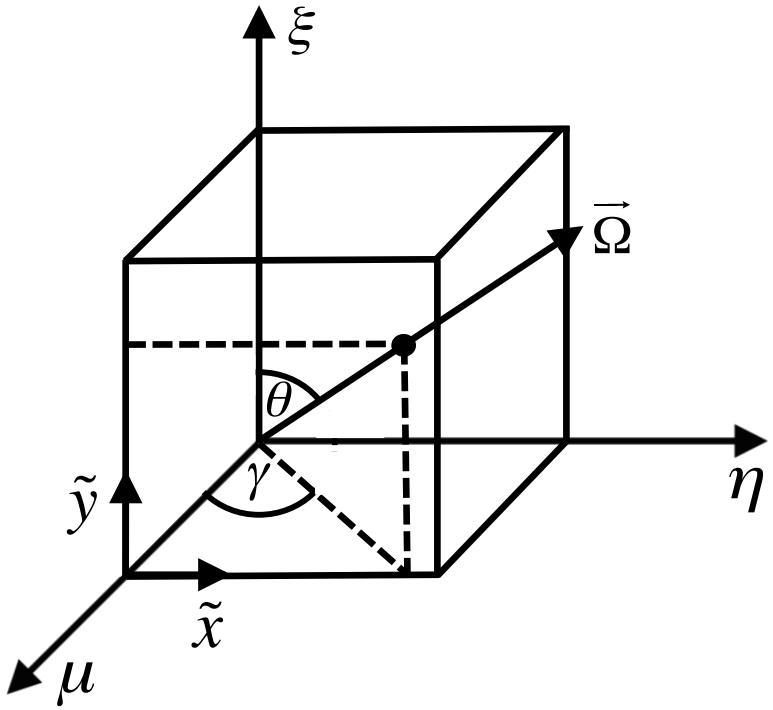

Figure A.1: $(\tilde{x}, \tilde{y})$ coordinates on surface of the inscribed cube perpendicular to the μ-axis. The vector from the unit sphere origin to any point in the $(\tilde{x}, \tilde{y})$ domain represents a unique direction $\vec{\Omega}$.

APPENDIX B

MULTI-OBJECTIVE OPTIMIZATION FIX-UP

B.1 Background

As discussed in Section 4.3, an "optimal" mapping algorithm should preserve both the shape and the angular moments of interest from the incoming solution. The new mapping algorithm is nearly "optimal" for mapping sufficiently smooth solutions away from octant boundaries. However, over- and under-shoots (including negativities) may occur in the mapped solution if mapping near solution discontinuities or octant boundaries. To address these instances, we apply a fix-up algorithm which uses multi-objective optimization problem (MOOP) to ensure the mapped solution satisfies a set of prescribed limits, and preserves the 0th angular moment to machine precision (MP) defined as $\leq 10^{-12}$ relative error. However, MOOP introduces minor error into the preservation of higher angular moments.

MOOP minimizes the total difference between a set of objective functions and their associated goals, while ensuring the solution satisfies a set of constraints. For LDFE-SQ mapping, the objective functions (Eqns. 5.9 to 5.11) and goals (Eqns. 5.12 to 5.14) preserve the 1st angular moments as well as possible. For QDFE-SQ mapping, the objective functions (Eqns. 5.9 to 5.11; 5.15 to 5.19) and goals (Eqns. 5.12 to 5.14; 5.20 to 5.24) preserve the 1st and 2nd angular moments as well as possible. An equality constraint (Eqn. 5.25) is imposed to preserve the 0th angular moment to MP, and multiple inequality constraints (Eqn. 5.8) are imposed to ensure the prescribed limits are satisfied.

B.2 Goal Programming Method

The goal programming (GP) method reduces the MOOP into a single-objective optimization problem (SOOP), which can be solved using any standard linear program (LP) e.g., Simplex or Interior Point methods.[16, 17, 18, 19] The GP method minimizes the total difference Z_{total} between a set of objective functions $Z_i, i = 1 : N_{\text{goals}}$ and their associated goals $G_i, i = 1 : N_{\text{goals}}$:

$$\text{Minimize } Z_{\text{total}} = \sum_{i=1}^{N_{\text{goals}}} \delta_i^+ + \delta_i^- \ , \tag{B.1}$$

where:

$$Z_i - G_i = \delta_i^+ - \delta_i^- \ \ , \ \ i = 1 : N_{\text{goals}} \ . \tag{B.2}$$

Eqns. B.1 and B.2 along with the inequality (Eqns. 5.8) and equality (Eqns. 5.25) constraints constitute the SOOP. We note δ_i^+ and δ_i^- are strictly positive values.

B.3 Standard Form

LPs require the SOOP to be written in standard form. We begin by adding artificial variables a to the equality constraints. Eqn. B.2 becomes

$$Z_i - \delta_i^+ + \delta_i^- + a_i = G_i \ \ , \ \ i = 1 : N_{\text{goals}} \ . \tag{B.3}$$

The 0th angular moment preservation constraint (Eqn. 5.25) becomes

$$\sum_{j=1}^{N_{\text{map}}} \Psi_j w_j + a = \sum_{k=1}^{N_{\text{orig}}} \Psi_k w_k \ . \tag{B.4}$$

For $\geq$ inequality constraints, we add surplus s' and artificial a variables. The lower limit of Eqn. 5.8 becomes

$$\Psi_j - s'_j + a_j = \Psi_{\min} \ , \ \ j = 1 : N_{\text{map}} \ . \tag{B.5}$$

For $\leq$ inequality constraints, we add slack s variables. The upper limit of Eqn. 5.8 becomes

$$\Psi_j + s_j = \Psi_{\max} \ , \ \ j = 1 : N_{\text{map}} \ . \tag{B.6}$$

We must minimize the sum of the artificial variables to return to the original system. Therefore, we add the artificial variables to Eqn. B.1 resulting in

$$\text{Minimize } Z_g = \sum_{i=1}^{N_{\text{goals}}} \delta_i^+ + \delta_i^- + M \sum_{\ell=1}^{N_{\text{art}}} a_\ell \ , \tag{B.7}$$

where M is an arbitrarily large constant. The use of M to increase the importance of minimizing the artificial variables is referred to as the Big-M method in literature.[16] Eqns. B.3 to B.7 is the standard form of the SOOP.

B.3.1 Fine-to-Coarse Fix-up

LPs require the standard form of the SOOP to be written in matrix notation. Eqns. B.8 to B.10 show: (1) matrix-A containing the left-hand coefficients of the constraints (Eqns. B.3 to B.6), (2) vector-b containing the right-hand values of the constraints, and (3) vector-c containing the coefficients of the minimization problem (Eqn. B.7) for LDFE-SQ fine-to-coarse fix-up. The matrix form of the SOOP for QDFE-SQ fine-to-coarse fix-up is analogous.

$$A = \left[\begin{array}{cccccccccccccccccccccc}
w_1\mu_1 & \cdots & w_4\mu_4 & -1 & & & 1 & & & & & & 1 & & & & & & & & & \\
w_1\eta_1 & \cdots & w_4\eta_4 & & -1 & & & 1 & & & & & & 1 & & & & & & & & \\
w_1\xi_1 & \cdots & w_4\xi_4 & & & -1 & & & 1 & & & & & & 1 & & & & & & & \\
w_1 & \cdots & w_4 & & & & & & & & & & & & & 1 & & & & & & \\
1 & & & & & & & & & -1 & & & & & & & 1 & & & & & \\
& \ddots & & & & & & & & & \ddots & & & & & & & \ddots & & & & \\
& & 1 & & & & & & & & & -1 & & & & & & & 1 & & & \\
1 & & & & & & & & & & & & & & & & & & & 1 & & \\
& \ddots & & & & & & & & & & & & & & & & & & & \ddots & \\
& & 1 & & & & & & & & & & & & & & & & & & & 1
\end{array}\right] \tag{B.8}$$

$$b = \begin{bmatrix} \sum_{k=1}^{N_{\text{orig}}} \Psi_k w_k \mu_k \\ \sum_{k=1}^{N_{\text{orig}}} \Psi_k w_k \eta_k \\ \sum_{k=1}^{N_{\text{orig}}} \Psi_k w_k \xi_k \\ \sum_{k=1}^{N_{\text{orig}}} \Psi_k w_k \\ \psi_{min} \\ \vdots \\ \psi_{min} \\ \psi_{max} \\ \vdots \\ \psi_{max} \end{bmatrix} \qquad \text{(B.9)} \qquad c = \begin{bmatrix} 0 \\ \vdots \\ 0 \\ 1 \\ \vdots \\ 1 \\ 0 \\ \vdots \\ 0 \\ M \\ \vdots \\ M \\ 0 \\ \vdots \\ 0 \end{bmatrix} \qquad \text{(B.10)}$$

B.3.2 Coarse-to-Fine Fix-up

Testing showed using the same prescribed limits for every mapped direction causes the mapped solution to significantly alter the shape of the incoming solution. Therefore, we set unique limits for each mapped direction based on the mapped solution without fix-up. We define bad ordinates as directions with mapped solution outside the prescribed limits, and good ordinates elsewhere. We begin by setting the mapped solution for all bad ordinates $\psi_m^{'}, m = 1 : N_{\text{bad}}$ to the nearest prescribed limit:

$$\psi_m^{'} = \begin{cases} \psi_{\text{min}} \text{ if } \psi_m < \psi_{\text{min}} \\ \psi_{\text{max}} \text{ if } \psi_m > \psi_{\text{max}} \end{cases} \quad , \quad m = 1 : N_{\text{bad}} \ , \qquad \text{(B.11)}$$

where ψ_m is the mapped solution for the bad ordinates without fix-up. Next, we calculate the net change in the 0th angular moment caused by applying Eqn. B.11:

$$\Delta\phi_{\text{net}} = \sum_{m=1}^{N_{\text{bad}}} w_m \left(\psi'_m - \psi_m\right) \ . \tag{B.12}$$

If $\Delta\phi_{\text{net}} > 0$, then we have removed 0th angular moment from the system. Therefore, we must add the same amount of 0th angular moment to the good ordinates to maintain 0th angular moment preservation. We set the lower limits of the good ordinates $\psi_n, n = 1 : N_{\text{good}}$ as the mapped solution without fix-up:

$$\psi_{\text{min},n} = \psi_n \ \ , \ \ n = 1 : N_{\text{good}} \ . \tag{B.13}$$

The upper limit of each good ordinate is the minimum of either the solution required to preserve the 0th angular moment ϕ_{inc} assuming each other good ordinate is set to their lower limit, or the prescribed upper limit:

$$\psi_{\text{max},n} = \min\left(\psi_{\text{max}}, \frac{\phi_{\text{inc}} - \sum_{n'=1,n'\neq n}^{N_{\text{good}}} w_{n'}\psi_{\text{min},n'} - \sum_{m=1}^{N_{\text{bad}}} w_m\psi'_m}{w_n}\right) \ . \tag{B.14}$$

If $\Delta\phi_{\text{net}} < 0$, then we have added 0th angular moment to the system. Therefore, we must remove the same amount of 0th angular moment from the good ordinates to maintain 0th angular moment preservation. We set the upper limits of the good ordinates $\psi_n, n = 1 : N_{\text{good}}$ to the mapped solution without fix-up:

$$\psi_{\text{max},n} = \psi_n \ \ , \ \ n = 1 : N_{\text{good}} \ . \tag{B.15}$$

The lower limit of each good ordinate is the maximum of either the solution required to preserve the 0th angular moment assuming each other good ordinate is set to their upper

limit, or the prescribed lower limit:

$$\psi_{\min,n} = \max\left(\psi_{\min}, \frac{\phi_{\text{inc}} - \sum_{n'=1,n'\neq n}^{N_{\text{good}}} w_{n'}\psi_{\max,n'} - \sum_{m=1}^{N_{\text{bad}}} w_m\psi_m^{'}}{w_n}\right) . \tag{B.16}$$

The above changes require modifications to the SOOP posed by Eqns. B.3 to B.7. The LDFE-SQ objective functions become

$$Z_1 = \sum_{n=1}^{N_{\text{good}}} \Psi_{\text{good},n}\mu_{\text{good},n}w_{\text{good},n} , \tag{B.17}$$

$$Z_2 = \sum_{n=1}^{N_{\text{good}}} \Psi_{\text{good},n}\eta_{\text{good},n}w_{\text{good},n} , \tag{B.18}$$

and

$$Z_3 = \sum_{n=1}^{N_{\text{good}}} \Psi_{\text{good},n}\xi_{\text{good},n}w_{\text{good},n} . \tag{B.19}$$

The associated goals become

$$G_1 = \sum_{k=1}^{N_{\text{inc}}} \Psi_{\text{inc},k}\mu_{\text{inc},k}w_{\text{inc},k} - \sum_{m=1}^{N_{\text{bad}}} \Psi_{\text{bad},m}\mu_{\text{bad},m}w_{\text{bad},m} , \tag{B.20}$$

$$G_2 = \sum_{k=1}^{N_{\text{inc}}} \Psi_{\text{inc},k}\eta_{\text{inc},k}w_{\text{inc},k} - \sum_{m=1}^{N_{\text{bad}}} \Psi_{\text{bad},m}\eta_{\text{bad},m}w_{\text{bad},m} , \tag{B.21}$$

and

$$G_3 = \sum_{k=1}^{N_{\text{inc}}} \Psi_{\text{inc},k}\xi_{\text{inc},k}w_{\text{inc},k} - \sum_{m=1}^{N_{\text{bad}}} \Psi_{\text{bad},m}\xi_{\text{bad},m}w_{\text{bad},m} . \tag{B.22}$$

The changes in QDFE-SQ objective functions and goals are analogous. The equality constraint for 0th angular moment preservation becomes

$$\sum_{n=1}^{N_{\text{good}}} \Psi_{\text{good},n}w_{\text{good},n} + a = \sum_{k=1}^{N_{\text{inc}}} \Psi_{\text{inc},k}w_{\text{inc},k} - \sum_{m=1}^{N_{\text{bad}}} \Psi_{\text{bad},m}w_{\text{bad},m} . \tag{B.23}$$

The inequality constraints for the prescribed limits are now set to the new limits presented in Eqns. B.14 and B.16:

$$\Psi_n - s'_n + a_n = \Psi_{\min,n} \ , \ \ n = 1 : N_{\text{good}} \ , \tag{B.24}$$

and

$$\Psi_n + s_n = \Psi_{\max,n} \ , \ \ n = 1 : N_{\text{good}} \ . \tag{B.25}$$

Eqns. B.26 to B.27 show matrix-A containing the left-hand coefficients of the constraints (Eqns. B.3; B.23 to B.25), and vector-b containing the right-hand values of the constraints. Vector-c containing the coefficients of the minimization problem (Eqn. B.7) for LDFE-SQ coarse-to-fine fix-up remains the same as Eqn. B.10. The matrix form of the SOOP for QDFE-SQ coarse-to-fine fix-up is analogous.

$$
A = \begin{bmatrix}
w_1\mu_1 & \cdots & w_{N_{\text{good}}}\mu_{N_{\text{good}}} & -1 & & 1 & & & & & & & & & & & & & & & \\
w_1\eta_1 & \cdots & w_{N_{\text{good}}}\eta_{N_{\text{good}}} & & -1 & & 1 & & & & & & & & & & & & & & \\
w_1\xi_1 & \cdots & w_{N_{\text{good}}}\xi_{N_{\text{good}}} & & & -1 & & 1 & & & & & & & & & & & & & \\
w_1 & \cdots & w_{N_{\text{good}}} & & & & & & -1 & & & & & & & & & & & & \\
1 & & & & & & & & & \ddots & & & & & & & & & & & \\
& \ddots & & & & & & & & & -1 & & & & & & & & & & \\
& & 1 & & & & & & & & & 1 & & & & & & & & & \\
1 & & & & & & & & & & & & 1 & & & & & & & & \\
& \ddots & & & & & & & & & & & & 1 & & & & & & & \\
& & 1 & & & & & & & & & & & & 1 & & & & & & \\
& & & & & & & & & & & & & & & \ddots & & & & & \\
& & & & & & & & & & & & & & & & 1 & & & & \\
& & & & & & & & & & & & & & & & & 1 & & & \\
& & & & & & & & & & & & & & & & & & \ddots & & \\
& & & & & & & & & & & & & & & & & & & 1 &
\end{bmatrix}
\tag{B.26}
$$

$$b = \begin{bmatrix} \sum_{k=1}^{N_{\text{inc}}} \Psi_{\text{inc},k}\mu_{\text{inc},k}w_{\text{inc},k} - \sum_{m=1}^{N_{\text{bad}}} \Psi_{\text{bad},m}\mu_{\text{bad},m}w_{\text{bad},m} \\ \sum_{k=1}^{N_{\text{inc}}} \Psi_{\text{inc},k}\eta_{\text{inc},k}w_{\text{inc},k} - \sum_{m=1}^{N_{\text{bad}}} \Psi_{\text{bad},m}\eta_{\text{bad},m}w_{\text{bad},m} \\ \sum_{k=1}^{N_{\text{inc}}} \Psi_{\text{inc},k}\xi_{\text{inc},k}w_{\text{inc},k} - \sum_{m=1}^{N_{\text{bad}}} \Psi_{\text{bad},m}\xi_{\text{bad},m}w_{\text{bad},m} \\ \sum_{k=1}^{N_{\text{inc}}} \Psi_{\text{inc},k}w_{\text{inc},k} - \sum_{m=1}^{N_{\text{bad}}} \Psi_{\text{bad},m}w_{\text{bad},m} \\ \psi_{\text{min},1} \\ \vdots \\ \psi_{\text{min},N_{\text{good}}} \\ \psi_{\text{max},1} \\ \vdots \\ \psi_{\text{max},N_{\text{good}}} \end{bmatrix} \tag{B.27}$$

B.4 Simplex Method

We chose to use the Simplex method [16, 17, 18, 19] for solving the SOOP required for fix-up, due to its robustness and simplicity in implementation. The Simplex method begins with an initial feasible solution, which sets the non-basic variables (Ψ, δ^+, δ^- and s') to zero resulting in non-zero basic variables (a and s) to satisfy the SOOP constraints (Eqn. B.3 to B.6). Each iteration of the Simplex method exchanges a basic variable with a non-basic variable such that Z_{tot} (Eqn. B.7) decreases, while the solution remains feasible.[16] The Simplex method moves from vertex to vertex of the feasible solution region, and is applied until an optimal feasible solution is found in which Z_{tot} can no longer decrease. We test the most simple variant of the Simplex method, known as the Revised Simplex method, [17, 18] which represents the Simplex method as linear algebra computations. We note other methods (e.g., Bartels-Golub, Forrest-Tomlim, Reid, etc) have been developed to improve the speed and accuracy of the Simplex method, particularly for SOOPs requiring large sparse systems, or producing ill-conditioned matrices.[17] However, the SOOPs for LDFE-SQ and QDFE-SQ fix-up does not require solving particularly large systems, nor produce ill-conditioned matrices during our testing. The Revised Simplex method pseudocode is

provided in Algorithm 1. The input parameters are the matrices for the SOOP presented in Sections B.3.1 and B.3.2. The output variables are vector-d_f containing the mapped solution with fix-up, and vector-C_B containing the indices in d_f corresponding to each mapped direction.

Input : $\mathbf{A}, b, c$ (Inputs defined in Section B.3.1)
Output: d_f, c_B

Set $\Psi, \delta^+, \delta^-, s'$ to 0 (Variables not in the basis)
Set a, s to satisfy constraints (Variables currently in the basis)
Form $\mathbf{B}$ (Columns of $\mathbf{A}$ for variables in the basis)
Checkpoint 1
Compute $\mathbf{B}^{-1}$
Compute $d = \mathbf{B}^{-1}b$
Determine c_V (Entries of c for variables not in the basis)
Determine c_B (Entries of c for variables in the basis)
Determine $\mathbf{V}$ (Columns of $\mathbf{A}$ for variables not in the basis)
Compute $\tilde{c}_V = c_V - c_B\mathbf{B}^{-1}\mathbf{V}$
Find most negative $\tilde{c}_V$ entry, store index in j
if $min(\tilde{c}_V) \geq 0$ **then**
    Return $d_f \equiv d$ (Final solution)
    Return c_B (Variable indices for d)
    End Program
end
Compute w=$\mathbf{B}^{-1}a_j$ (a_j is the j^{th} column of $\mathbf{A}$)
Find smallest, positive ratio d_i/w_i
Swap column i in $\mathbf{B}$ with a_j
Swap column j in $\mathbf{A}$ with b_i (b_i is the i^{th} column of $\mathbf{B}$)
return *Checkpoint 1*

Algorithm 1: Revised Simplex Method